A massively parallel matrix free finite element based multigrid method for simulations of heterogeneous materials using tomographic images

Xiaodong Liu

To cite this version:

Xiaodong Liu. A massively parallel matrix free finite element based multigrid method for simulations of heterogeneous materials using tomographic images. Mechanics of materials [physics.class-ph]. École centrale de Nantes, 2019. English. NNT : 2019ECDN0057 . tel-02493207

THESE DE DOCTORAT DE

L'ÉCOLE CENTRALE DE NANTES
COMUE UNIVERSITE BRETAGNE LOIRE

ECOLE DOCTORALE N° 602
Sciences pour l'Ingénieur
Spécialité : « *Mécanique des Solides, des Matériaux, des structures et des surfaces* »

Par
« Xiaodong LIU »

« A massively parallel matrix free finite element based multigrid method for simulations of heterogeneous materials using tomographic images »

Thèse présentée et soutenue à Nantes, le 10/12/2019
Unité de recherche : UMR 6183, Institut de Recherche en Génie Civil et Mécanique (GeM)

Rapporteurs avant soutenance :

Jean-Charles PASSIEUX	Professeur des Universités	INSA Toulouse
Cornelis H. VENNER	Professeur	University of Twent

Composition du Jury :

Présidente :	Katia MOCELLIN	Professeur	MINES ParisTech
Examinateurs :	Luisa SILVA	Chargée de Recherche, HDR	Centrale Nantes
	Antonius A. LUBRECHT	Professeur des Universités	INSA Lyon
Dir. de thèse :	Julien RETHORE	Directeur de Recherche CNRS	Centrale Nantes

Invité

Alain COMBESCURE	Professeur des Universités

Acknowledgements

Tout d'abord, je voudrais remercier M. Jean-Charles Passieux et M. Cornelis H. Venner, qui ont accepté la lourde tâche d'être rapporteurs de ma thèse. Les marques qu'ils ont menés et les questions qu'ils ont posés sont très intéressantes. Ça me permettra d'améliorer et de donner une valeur de plus de mon travail tout en ayant une réflexion pertinente sur les perspectives de mes travaux. Je tiens également mon merci à Mme. Katia Mocellin, qui m'a fait honorer d'être présidente de ma soutenance. J'aimerais remercier également Mme. Luisa Silva qui a examiné mon travail de ces trois ans. Je tiens également à remercier M. Alain Combescure qui a accepté d'être venu malgré que'il est à la retraite.

J'adresse nes infinis remerciement à mes directeurs de thèse M. Julien Rétoré et M. Ton Lubrecht, pour le temps qu'ils m'ont consacré, pour les milles émails qu'ils m'envoyés jours et nuits, pour la liberté qu'ils m'ont accordée, pour la confiance qu'ils m'ont faite, pour les ressources qu'ils m'ont ramenées, pour les soutiens qu'ils m'ont tenus, pour les trajets qu'ils ont faits, pour les remarques qu'ils m'ont données et etc. Sans eux, je n'aurais jamais eu assez de courages pour avancer. Encore un grand merci à tous les deux.

J'aimerais remercier chaleureusement mes collègues qui m'ont aidés et soutenus. Merci à Nicolas Chevaugeon qui m'a fait une première ouverture sur l'aspect parallélisme. Merci à Hugues Digonnet qui m'a aidé à construire mes algorithmes parallélisés et à développer ma plateforme de visualisation. Merci à Alexis Salzman qui m'a fait une première formation sur l'utilisation de serveur de l'école. Merci à Gregory Legrain qui m'a donné des conseils sur C et C++. Merci à Abdullah Waseem avec qui j'ai fait le vélo à Loire et avec qui j'ai discuté de la science, surtout, l'homogénéisation. Merci à Nicolas Moës et Jean Yves Buffière qui ont accepté d'être mes membres du CSI et de me donner des remarques pendant les deux réunions. Merci aux personnels de l'équipe MS pour leur soutient : Cynthia Nozay, Éric Manceau. Merci aux collègues avec qui j'ai passés ces trois ans dans le même bureau. Merci à Charlotte Bazin de la RH et à Mme Manuèle Bouchet en tant que médicine de travail qui m'ont beaucoup aidé sur l'aménagement de ma poste de travail. Merci à toutes les personnes de l'équipe MS, du GeM et de Centrale Nantes.

Je tiens également à remercier mes amis (amies) avec qui j'ai partagé des moments joyeux durant ces trois ans.

Finalement, je voudrais remercier à ma famille : mon père Guangbao, ma mère Jiaqin. Sans eux, je ne n'aurais jamais pu arriver à faire tout ce que j'ai fait et tout ce que j'ai envies de faire. Merci à ma sœur Xiaoyu qui me soutient tout le temps à distance. Merci à ma copine Jiayu qui j'ai rencontré à la fin de ma première année de thèse, mais surtout avec qui je voudrais vivre pendant toute ma vie.

Contents

Chapter 1

State of the art

Contents

1.1 Background and motivations

The development of material processing leads to innovations in material science. Many man-made materials, with improved corrosion resistance, high strength, light weight, *etc.*, are widely used in the industrial domain and in the biological domain. However, during the life cycle of these innovative materials, many problems, *e.g.* damage, crack, *etc.* can send the products into discarding step. The work of scientists is to find the defects on these materials and to give some advice to engineers to improve the material performance. Many techniques are investigated to find the defects on and in material. Thousands of years ago, chips of crystal or obsidian were used by Egyptians to better view small objects. Nowadays, the microscope has been developed, but it can only help scientists to see the surface of materials. The homogenization method was then investigated to predict the effective material properties from its microstructure. Since the structure of man-made materials are ”theoretically known”, researchers proposed to predict the effective material properties from the ”theoretical” microstructure of materials, *e.g.* laminated structure materials.

Heterogeneity leads to homogenization. The mathematical theory of homogenization methods was proposed to obtain the effective properties, *e.g.* conductivity, elastic modulus, of heterogeneous materials, *e.g.* composite materials. The principle of the homogenization method is to obtain the global material property from its microstructure as presented in Figure 1.1 from a to b. In the 1950s, researchers started studying the strain and stress in heterogeneous materials. The well-known Eshelby's problem ([ESH 57, ESH 59]) dates to these years. After that, the elastic behavior of more complex materials, *e.g.* composite materials and polycrystals was studied by [HAS 62b, HAS 62a, HAS 64]. But the homogenization method was really proposed in the 1970s ([PAP 78, SÁN 80, OLE 84]) for periodic structures. It was developed for the application of the multiscale method. For more information, *e.g.* history, theory, about homogenization, see in [PAP 78, CIO 99, TAR 09, BAK 12].

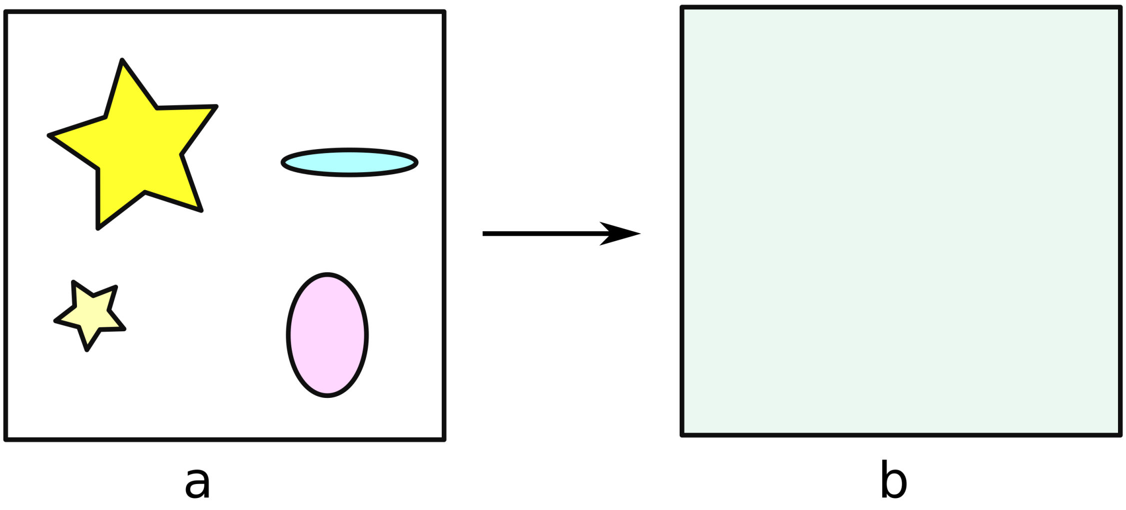

Figure 1.1: The principle of the homogenization method

Nowadays, two typical homogenization methods are used: the numerical homogenization and the analytical homogenization. The well-known analytical homogenization methods are: Hashin-Shtrikman by [HAS 62b, HAS 62a], Mori-Tanaka by [MOR 73, BEN 87], self-consistent by [HER 54, BUD 65, HIL 65], *etc.*. The principle of the analytical homogenization is to use a formulation to compute the effective material properties from its microstructure with the material properties, volume fractions, geometries, *etc.* of each component. The advantage of this kind of homogenization method is that the numerical process is simple. However, these methods are suitable only for materials with simple geometry and it does a poor job for materials with large property variations. For random heterogeneous materials, the analytical homogenization method is not sufficient. The computational or numerical homogenization method is developed and often used in the last three decades. The principle of the numerical homogenization is to carry out numerical simulations with specific boundary conditions on its microstructure. The effective material properties at the macroscopic scale can then be computed from its solutions at the microscopic scale.

However, as stated the origin of the homogenization method: to predict the effective material properties from its microstructure. The two major drawbacks of the homogenization method are obvious.

- It looses microscopic details. *e.g.* The free edge effect in laminated structures can never be predicted by the classical laminate theory. However, this kind of effects can lead to material damage.
- The ”theoretical” material microstructure is just theoretical, the ”real” microstructures are always different from its theoretical structures due to the manufacturing process limitations.

To obtain the real material microstructure without destroying the material, the well-known Computed Tomography (CT) was invented.

The mathematical theory of the Radon transform in 1917 is the first proposal of X-ray computed tomography according to [RAD 05]. In 1979, Allan M. Cormack and Godfrey N. Hounsfield received the Nobel Prize in Physiology or Medicine for ”the development of computer assisted tomography”. After that, the CT techniques are widely used in the last three decades. Especially, it is widely used in the medical domain for screening for diseases and preventive medicine, *e.g.* full-motion heart scans, screening for rheumatic diseases as illustrated in Figure 1.2.

Beside the medical use, CT techniques are also used in material sciences. [HIR 95] observed the internal damage in a metal matrix composite under static tensile loading by *in situ* X-ray computed tomography. [HEE 97] introduced the potential of the CT to quantify plant roots *in situ*. [RAN 10] studied the fatigue crack by using the CT image of cast iron, as presented in 1.3. [LEC 15] observed the free edge effect in laminated composites by using X-ray CT. [RUB 13] studied the mechanical fatigue properties of natural rubber by the *in situ* X-ray tomography. The squeeze flow is studied in heterogeneous unidirectional discontinuous viscous prepreg laminates by using CT techniques in [SOR 17].

The application of CT images, is not only useful in the experimental domain, but also in the numerical simulation domain. The objective of using CT images to perform numerical simulations is to account for the ample information of the inner structure of materials, especially for complex microstructures, *e.g.* composite materials. The main

Figure 1.2: A rheumatic diseases image. iStock.com

process of using the CT image for numerical simulations is to use the CT image as input and to account for the material microstructure. The work of [LEN 98] and [BES 07] presented the real simulation of bone tomography. They studied mechanical problems *e.g.* hip fractures of the human femur, using Finite Element Methods (FEM). [FER 99], [MIC 10] and [PRO 16] applied the FEM simulations to tomographic images of industrial materials to analyze their properties. [LEG 11] developed an image-based modeling using the X-FEM and the level set numerical solver. The investigation, *i.e.* high order X-FEM and the level sets for complex microstructures, proposed in [LEG 12], can also applied for CT simulations. [LIA 13] studied a voxel-based approach compared with the X-FEM/levelset based on images.

Both the numerical and the experimental development on CT images have been made by researchers. However, for certain cases, the experimental applications can not be performed, *e.g.* a living part of human, or the available equipment can not insure an experiment, or the experiments are so expensive. In these cases, numerical simulations have been widely developed and used by researchers and scientists. Meanwhile, CT images contain ample information. Using them as an input for the numerical simulation permits one to understand material behavior at the microscopic scale. As stated above, many investigations have been made by researchers to perform CT simulations. However, the numerical simulations using CT images are still a challenge for researchers because of its complexity and its dimension. To employ such simulations, the computational cost is expensive both because of the time consumption and the memory space requirement, *e.g.* large CT images can have more than 8 billion voxels.

This work is motivated by the following points.

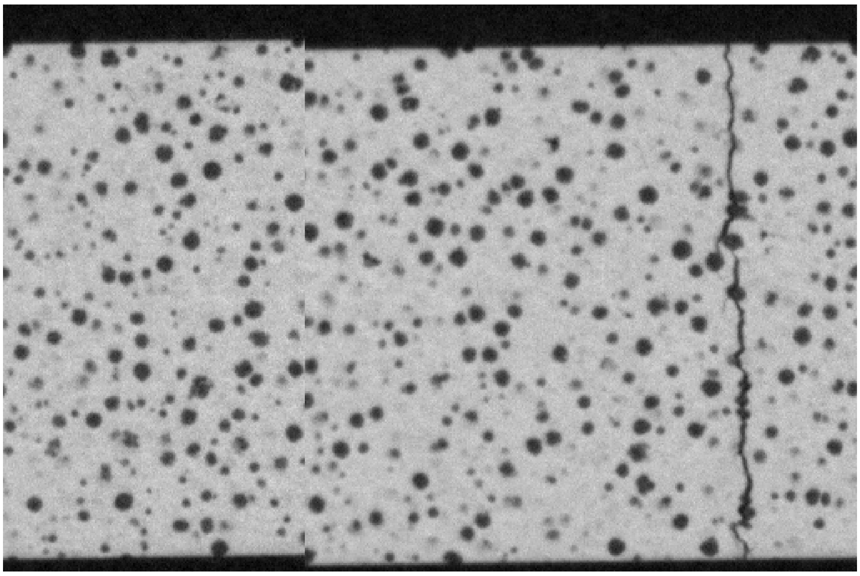

Figure 1.3: Crack in cast iron

- To understand the material behavior of heterogeneous materials.
- To automatically perform numerical simulations using large scale 3D CT images.

1.2 Literature review of different methods

To develop a solver for numerical simulations, the first step is to choose a numerical technique, *e.g.* the Finite Element Method (FEM), the Finite Difference Method (FDM), the Fast Fourier Transform (FFT), *etc.*.

1.2.1 The finite element method

Among all the techniques for the numerical simulations of mechanical and thermal problems, the first to come to mind is the FEM. The FEM was firstly proposed in the 1950s. It was used for the aerospace industry at the beginning. According to [FIS 07], its principle is to discretize the target domain into small parts, which refers to finite elements. Equations are firstly developed on each element. These small domains are then assembled to have a large system of equations. This large system of equations models the entire problem. The final step is to solve this large system of equations by direct or iterative solvers. For more information about the FEM and its applications to mechanical problems, see in [ZIE 00, LAR 13].

Many works of numerical simulations are based on the FEM. [FOU 99, CHE 02] investigated the contact problem of forming processes by the FEM. [LEN 98, BES 07, FER 99, MIC 10, PRO 16] applied the FEM on CT simulations. [KAN 03, ANN 07,

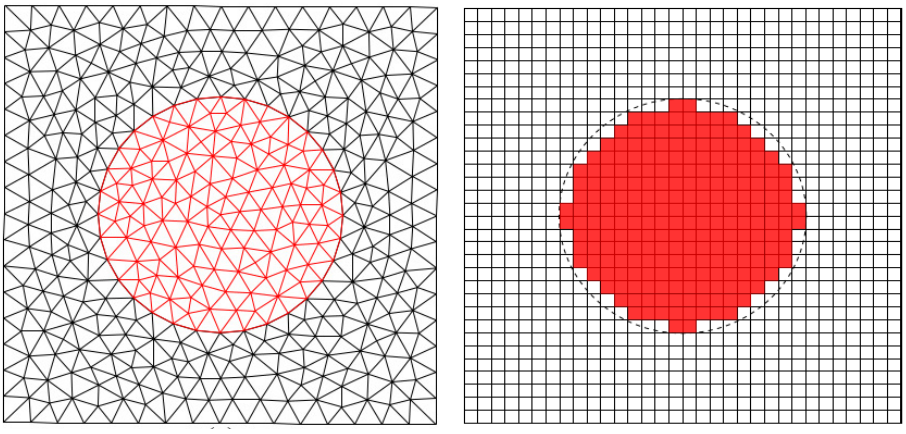

(a) FEM mesh

(b) FDM mesh

Figure 1.4: Mesh generated by FEM and FDM for a circular inclusion in a rectangular domain [GU 16]

KAR 07] presented the applications of the FEM on composite materials. The advantages of the FEM are the following:

- Abundant element types can deal with complicated geometries to obtain a good approximation. As presented in 1.4(a), a circle can be almost perfectly approximated.
- The implementation of boundary conditions is straightforward.
- Many investigations have been made by researchers.

Despite these advantages, the two weak points of FEM are the complicity of mesh generation and the computational cost. Its abundant element types can insure the correct geometry, but it requires a lot of work, especially for CT images. To generate a perfect mesh corresponding to CT images, it requires plenty of human intervention. This can take more than half of the total work time. Meantime, the assembled large system of equations of the entire problem is very large for a problem with billions of Degree of Freedom (DoF). It requires much memory space, *e.g.* the size of the sparse stiffness matrix for a problem with 16 billion of DoF is about 3.14 TB. Furthermore, traditional FEM can slow down quickly for large scale problems. The traditional FEM can be a big challenge if used in this work. Thus, specific treatment is needed to apply the FEM for this work.

1.2.2 The fast Fourier transform based method

FFT-based methods are very attractive for problems with highly heterogeneous materials. FFT based methods for periodic elasticity have been successfully used for composite materials during the last three decade. This method does not need the full mesh of the microstructure. The FFT based method is carried out on a regular grid. It can overcome the drawback of FEM. It was the periodic problems that led to the FFT-based method [NEM 82, SUQ 90]. This method is then developed by [MOU 98, EYR 99, VIN 08, IDI 09, BIL 07]. It becomes almost routinely applied to visco-plastic and rigid-plastic materials. However, as implied its origin, it can correctly deal with problems with periodic boundary conditions, which is not possible to simulate using the experimental boundary conditions, *e.g.* traction, fracture problems.

1.2.3 The finite difference method

The finite difference method is a method used for solving partial differential equations (PDEs). It was firstly applied in the 1950s. The principle is to use the Taylor expansion and differential quotients to approximate the derivatives in PDEs. The approximated solutions are then solved by the direct or the iterative solver, *e.g.* Jacobi solver, Gauss-Seidel solver. The FDM is a conventional method applied for fluid mechanical problems, *e.g.* Navier-Stokes equations, Poisson equations. The way to discretize the domain of the FDM is not like the FEM. As illustrated in Figure 1.4(b), for the same problem, the FDM discretization can not have the same geometry approximation as the FEM. For more information about the FDM, see in [SMI 85].

For the same problem, the FDM is normally faster than the FEM for a uniform structured grid. The memory space required by the FDM is less than the FDM. However, the implementation of the boundary conditions for the FDM is complicated. Nevertheless, some work [DOW 90] has been done to relieve this problem. Meanwhile, the convergence of the FDM can be slowed down quickly after few iterations. This is because the Jacobi solver and Gauss-Seidel solver can quickly eliminate high frequency errors. But for the low frequency errors, they do a poor job. Due to these drawbacks, the FDM is not often used for the solid mechanics. Nevertheless, several works can be found like [DOW 90, GU 16].

1.2.4 The matrix free finite element method

As stated above, the application of the FEM on the X-ray tomography image simulation is a big challenge due to the memory space requirement and the time consumption. To overcome the drawback of the FEM, a reformulated FEM is investigated by researchers ([HUG 87, RIE 96, AUG 06]) during the last three decades. It is the matrix free finite element method (MF-FEM). The MF-FEM was proposed to diminish memory requirements and to apply parallel computing. The MF-FEM is particularly favorable for problems with regular and few element types. The MF-FEM does a good job for problems arising from voxel conversions. With the voxel conversion, the mesh generation can be automatic. All the generated elements have exactly the same geometry and orientation. [ARB 08] presents a human bone structures simulation using CT images by the MF-FEM.

The often used MF-FEM technique for heterogeneous materials is element-by-element (EBE). The principle is to compute the residual element by element without the entire stiffness matrix. The main drawback of this technique is that it is difficult to find an efficient preconditioner. The often used preconditioner is the EBE preconditioning ([HUG 87]) or the Jacobi preconditioning (diagonal scaling). However, it is not efficient for complex problems like CT simulations. An often used accelerator is the well-known MultiGrid algorithm, as presented in [ARB 08] the MF-FEM coupled with the aggregation-based MultiGrid method.

1.2.5 The MultiGrid method

The MultGrid (MG) method is an acceleration method based on the FDM or the FEM by solving the problem on different grids. As presented in Figure 1.5, the problem is discretized using two different mesh sizes. By solving the problem on these two grids, the high frequency part of the error can be eliminated on the fine grid and the low frequency part can be eliminated on the coarse grid. This strategy can thus overcome the drawback of the Jacobi relaxation. The MG method used in this work refers to the geometric MG. Another kind of MG is algebraic MG (AMG [RUG 87]), which is not presented in this work.

The MG method was proposed in the 1960s by [FED 62, FED 64]. Its initial objective was to solve the Poisson equation. The efficiency of the MG was presented about ten years after the paper of Fedorenko by Brandt ([BRA 77, BRA 77]). Meanwhile, the principle of the MG was pointed out by Brandt. After that, other researchers investigated to improve the convergence performance of the MG method on problems with large variations of material properties, such as the work of [ALC 81] for 2D, [HOE 98] for 3D, [ENG 96] and [ENG 97]. For more information about the MG method, see in [BRA 11, TRO 00, VEN 00].

All the early work using the MG method was on fluid mechanics. The application of the MG method to solid mechanics dates to the 1980s for 2D problems by [BRA 88, BRA 85]. Its applications on 3D solid mechanics are illustrated by [PAR 90a, PAR 90b]. They pointed out that the MG convergence performance does not depend on the problem size by using a homogeneous structure, but it is sensitive to the problem feature. [ADA 99] applied the parallel computing on the MG method to achieve efficiency. For the work of the recent years, [PAS 11] applied the MG method with the extended FEM to estimate the generalized stress intensity factors. [BOF 15, ZHA 19, BOF 12b] studied the contact problem in heterogeneous materials.

1.2.6 Parallel computing

The numerical technique has a huge influence on the efficiency. The computer which performs the numerical simulations plays also an important role. Nowadays, with the development of supercomputers, one can apply parallel computing to diminish the computing time.

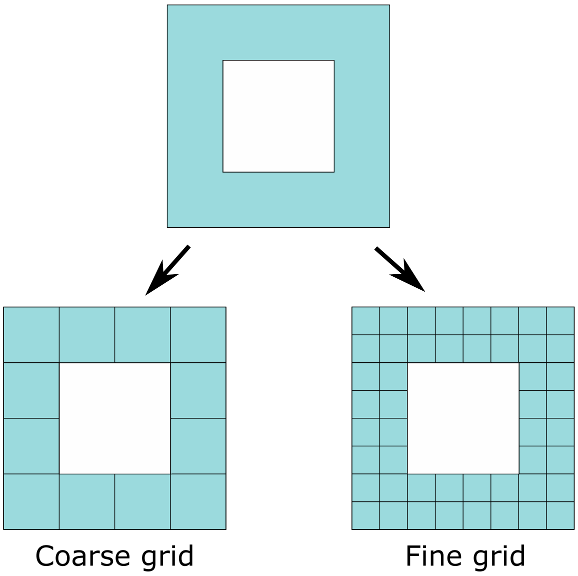

Figure 1.5: The coarse grid and the fine grid for a plate with a rectangular cavity

The first electronic programmable computer ENIAC built in the U.S, brought the dawn to computational science. Nevertheless, researchers and inventors were not satisfied with such huge and slow computer. The development of the modern computer received its significant considerations. Supercomputers were therefore built to support the wide ambitions of researchers. Sperry Rand built the first supercomputer LARC in 1960, a true massively parallel computer was firstly realized in the 1970s. Moreover, during the last decade, the supercomputers have been rapidly developed. Until today, the fastest supercomputer of the world can achieve 148 600.0 TFlop/s with more than 2 million cores. They are no longer reserved only for national institutes *e.g.* weather research, nuclear research. Nowadays, some large companies have supercomputers to carry out their research on industrial applications.

According to [KUM 02], the use of the supercomputer is primary on structural mechanics ([ADE 91]), computational biology ([SCH 96]) and commercial applications. This book ([KUM 02]) gives an overall reference to know and to learn parallel computing. For more information about parallel computing, please refer to this book. Nevertheless the investigations of researchers, there are still many challenges to apply parallel computing on traditional numerical techniques. Many researchers try to improve the performance of parallel computing. [MES 08, DIG 19] proposed a parallel anisotropic mesh adaption for the application of fluid mechanics on supercomputers. Applications of the parallel computing on the MG method can be found in [BRA 81, MCB 91, DUR 96, YAN 02].

1.3 Objectives

The proposal of this work is based on the difficulties of performing numerical simulations directly on X-ray tomography images. As stated before, the major questions are:

- How to deal with the complicated microstructure of CT images (mesh generation problem)?
- How to handle the material property jumps?
- How to reduce the memory space requirement?
- How to obtain the result efficiently?

With these proposed questions, the aim of this work is to develop an automatic and efficient solver to perform numerical simulations on heterogeneous materials using X-ray tomographic images. This objective can be detailed as followings.

- **Automatic**: the numerical simulation shall performance itself without too much human intervention.
- **Efficient**: the solver shall have a good efficiency.
- **Heterogeneous materials**: the solver shall be robust to deal with material property discontinuities or jumps as well as with geometries discontinuities.

To achieve these objectives, this work is based on the following proposals:

- Propose a strategy to take one image voxel as an elementary node for the mesh generation to avoid human intervention.
- Apply the MF-FEM to reduce memory space requirement and improve parallel performance.
- Investigate an efficient and new homogenization technique to compute the coarse grid operator of the MG method to improve its convergence performance for the heterogeneous materials.
- Develop a massively parallel MF-FEM based MG program both for thermal problems and mechanical problems, and analyze its performance and efficiency.
- Apply the developed strategy by using images of a laminate structure and a random heterogeneous structure, *i.e.* glass reinforced plastic laminated structure and cast iron. The effective conductivity of this two materials is also computed by apply the numerical homogenization.
- Analyze the free edge effect in the composite materials and compare to the experimental result.
- Study the effects of soft inclusions in materials with a crack opening problem.

1.4 Outline of the thesis

The outline of the rest chapters of this thesis is presented as followings.

Chapter 2 reviews the fundamentals of thermal conduction and its numerical solutions. The proposed strategy is presented in this chapter, its efficiency is also demonstrated. Section 2.2 presents the equations of the thermal conduction and its numerical solutions by the MF-FEM. Section 2.3 introduces the basic of the MG method. Its defects are also presented. Several special techniques, *e.g.* homogenized material property, are proposed to enhance the stability and the efficiency of MG methods. In section 2.4, we present the high performance computing to tackle time and memory consumption. The hybrid MPI+OpenMP programming and its communication strategy are illustrated. The parallel performance is analyzed at last.

Chapter 3, we present some applications of the thermal conduction in heterogeneous materials by using CT images. The validation of the proposed method is illustrated in this chapter. The application of the numerical homogenization method with the proposed strategy is demonstrated by using images of nodular graphite cast iron and composite materials. Simulations with more than 8 billion DoF are presented at the end of this chapter.

Chapter 4 demonstrates the principle to apply the proposed strategy for the mechanical problem. The process to develop an efficient strategy on mechanical problems is illustrated. The detailed application is presented for linear elastic problems. The validation of the built program is employed on a spherical inclusions problem. The free edge effect in a laminated structure is analyzed by a CT simulation with more than 18 billion DoF. The numerical result is compared with an experimental result. The last application deals with the linear elasticity of random heterogeneous material, *e.g.* cast iron, by using its CT image with a prescribed crack.

Finally, some conclusions and perspectives are drawn.

Chapter 2

Thermal problems

Contents

A part of this chapter is adapted from our published paper [LIU 19].

2.1 Introduction

In this chapter, the efficient strategy by using the MF-FEM based MG method is proposed. The strategy is built based on thermal conductions in heterogeneous materials. Section 2.2 reviews the thermal conduction and its numerical solutions by the MF-FEM. Section 2.3 introduces the basics of the MG algorithm and its sensibility on problems with large material property variations. Several specific techniques, *e.g.* homogenized material property, are proposed in this section to enhance the stability and the efficiency of the MG method. The efficiency of the proposed algorithm is analyzed at the end of this section. In section 2.4, we present the high performance computing to tackle the time and the memory consumption when working with large tomographic images. The hybrid MPI+OpenMP programming and its communication strategy are illustrated. Its parallel performance is analyzed.

2.2 Thermal conduction and its numerical solutions

2.2.1 Thermal conduction theory

Thermal conduction can be treated by a heat equation according to the first law of thermodynamics (*i.e.* conservation of energy):

$$\rho c_p \frac{\partial T}{\partial t} - \nabla \cdot (\alpha \nabla T) = \dot{q}_v \tag{2.1}$$

where:

ρ is the mass density of material

c_p is the specific heat capacity

T is the temperature

t is the time

∇ denotes the gradient operator

α is the thermal conduction coefficient which is a second order tensor

$\dot{q}_v$ is the volumetric heat source.

Since the focus of this work is thermal conductivity, it is assumed that there is no extra source and the thermal field does not depend on time. The heat equation (2.1) becomes a typical Poisson equation:

$$\nabla \cdot (\alpha \nabla T) = div(\alpha \nabla T) = 0 \tag{2.2}$$

The tomographic image used in this study is a cubic domain $\Omega \in \boldsymbol{R}^3$. Two kinds of boundary conditions are used on $\partial\Omega$ as illustrated in Figure 2.1:

- Dirichlet boundary condition, *i.e.* prescribed temperature, *e.g.* on Γ_1 and Γ_2
- Neumann boundary condition, *i.e.* prescribed heat flux, *e.g.* zero heat flux on the other four surfaces.

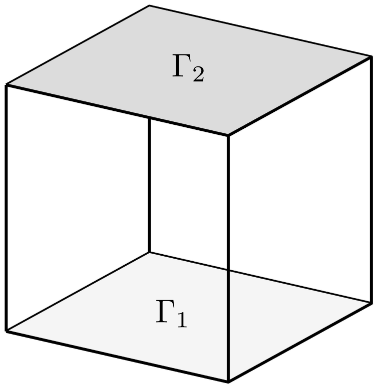

Figure 2.1: Two types of boundary conditions applied on $\partial\Omega$

which can be written as equation (2.3):

$$\begin{cases} T = T_0 & \text{on } \Gamma_1 \\ T = T_1 & \text{on } \Gamma_2 \\ \alpha \nabla T \cdot \vec{n} = \mathbf{0} & \text{on the other surfaces} \end{cases} \tag{2.3}$$

where $\vec{n}$ denotes the outward normal direction. To solve equation (2.2) and 2.3, many investigations have been proposed by researchers, *e.g.* FEM, FDM, the FFT based method. As reviewed in the previous chapter, the MF-FEM is the best choice for this work. One uses a finite element (FE) discretization to discretize the domain Ω.

2.2.2 The finite element discretization

FEM is one of the most common methods to discretize Ω and solve the governing equations. However, the images representing the inner structure of the material have a very complex shape. The use of standard meshes conforming to the phase geometry, requires much human work, as mentioned before and stated in the work of many researchers, *e.g.* [LEN 98], [BES 07], [FER 99], [MIC 10], [PRO 16] and [NGU 17]. The strategy to use one node per voxel in images has been chosen to avoid this difficulty. That means to assign the material property in each voxel on each elementary node. 8-node cubic elements are chosen to discretize Ω.

Multiplying equation (2.2) with a test function and integrating over Ω, one obtains:

$$\int_\Omega div(-\alpha \nabla T) \varphi \, d\Omega = 0 \tag{2.4}$$

where φ is the test function.

Applying integration by parts, the formula reads:

$$-\int_{\partial\Omega} \alpha \nabla T \cdot \vec{n} \varphi \, dS + \int_\Omega \alpha \nabla T \cdot \nabla \varphi \, d\Omega = 0 \tag{2.5}$$

where $-\boldsymbol{\alpha}\nabla T \cdot \vec{n}$ is the heat flux in the outward normal direction $\vec{n}$ on the boundary. Equation (2.5) can be summarized as:

$$\int_{\Omega} \boldsymbol{\alpha}\nabla T \cdot \nabla\varphi d\Omega = \int_{\partial\Omega} \boldsymbol{\alpha}\nabla T \cdot \vec{n}\varphi dS \tag{2.6}$$

which is also referred to:

$$\vec{q}_{in} = \vec{q}_{ex} \tag{2.7}$$

with

$$\begin{cases} \vec{q}_{in} = & \int_{\Omega} \boldsymbol{\alpha}\nabla T \cdot \nabla\varphi d\Omega \\ \vec{q}_{ex} = & \int_{\partial\Omega} \boldsymbol{\alpha}\nabla T \cdot \vec{n}\varphi dS \end{cases}$$

where $\vec{q}_{in}$ is the internal heat flux. $\vec{q}_{ex}$ denotes the external heat flux.

Employing finite element discretization, one obtains:

$$\vec{T} \approx \vec{T_h} = \sum_{i=1}^{N} T_i\varphi_i \tag{2.8}$$

where $\vec{T_h} = \{T_1, T_2, \ldots, T_n\}$ is an approximate solution of T, N denotes the node number and φ_i is the shape functions of 8-node cubic elements, which is the same as the test function.

In this work, the material is locally isotropic. Instead of using $\boldsymbol{\alpha}$, we use α for the sake of simplicity. Finally, the internal heat flux for node j can be described as:

$$q_{in} = \sum_{e}\sum_{i}\sum_{m}\sum_{g=1}^{8} w_g \nabla_m \varphi_i \alpha^g T_i \nabla_m \varphi_j \tag{2.9}$$

where g is the Gauss integration point number. $m = 1, 2, 3$ represents three directions. w_g is the weight of each Gauss integration point. α^g is the conductivity at Gauss integration point. $\sum_e$ demotes the sum in elements. α is the conductivity at each Gauss integration point, which can be is obtained by the integration with shape functions from the conductivity at each elementary node:

$$\alpha^g = \sum_{i=1}^{8} \alpha_i \varphi_i$$

2.2.3 The matrix free finite element iterative solver

The aim is to solve equation (2.7). The solution of this equation can be obtained by the well-known direct solvers and iterative solvers. For direct solves, we have to assemble the stiffness matrix, For a simulation of a 2048^3-element problem, the size of global sparse stiffness matrix is $2049 \times 2049 \times 2049 \times 27 \times 8$bytes ≈ 1.69 TB, it is impossible to solve this problem with a normal computer.

Instead of using a direct solver, one proposes to use an iterative solver. The assembly of the stiffness matrix is not suggested due to the size of the entire stiffness matrix. Moreover, for a mechanical problem, the size of the stiffness matrix is much larger than the thermal problem. One of the best-known techniques not assembling the stiffness matrix is to use a matrix free FEM (MF-FEM). The regular structure model, *grid-based*, permits one to use the MF-FEM. The work of HUGHES *et. al* [HUG 83] used MF-FEM for the first time. It was therewith developed by CAREY *et. al* [CAR 86]. For instance, this method is developed and widely used, especially, for parallel computing (see *e.g.* [TEZ 93]). KRONBICHLER *et. al* [KRO 18] presented the performance of a MF-FEM based MG method for a Poison problem. In spite of the development of this technique, nowadays, MF-FEM is not yet included in commercial software.

The strategy proposed in this work is to compute the unknowns node-by-node. It can be described as:

$$T^{iter+1} = T^{iter} + \omega \frac{q_{ex} - q_{in}}{stiff} \tag{2.10}$$

where T^{iter+1} and T^{iter} are the temperature of one node in the current and the previous iteration. ω is the relaxation coefficient. For $0 < \omega < 1.0$, it is often referred to the damped Jacobi, $\omega = 1.0$ reads the normal Jacobi and $\omega > 1.0$ presents the over-relaxation. Different relaxation coefficients can lead to different convergence speeds. $stiff$ is the diagonal value of the stiffness matrix at each DoF. It reads:

$$stiff = \sum_{e}\sum_{m}\sum_{g=1}^{8} w_g \nabla_m \varphi_i \alpha^g \nabla_m \varphi_i$$

With such a strategy, we firstly compute the residual and $stiff$ element-by-element, and then the unknown node-by-node. Hence, we dot not need to assemble the entire stiffness matrix, which solves the problem of memory consumption.

2.3 MultiGrid

The MFE-FE type iterative single level Jacobi solver proposed previously can quickly decrease the high frequency components of the error, but for low frequency errors, it does a poor job [VEN 00]. The convergence speed diminishes rapidly as presented in Figure 2.9(a) for a typical spherical inclusion problem with a material property contrast of 10.

2.3.1 The standard MultiGrid

It is well known that the MG method is one of the most efficient ways to increase the convergence rate. The idea of the MG method is to construct several levels or grids. Then, iterative relaxations are carried out at each level, high-frequency errors can be eliminated on fine grids and low-frequency errors can be eliminated on coarse grids [BRA 77, BRA 11]. With this method, one can solve the slow convergence problem of the single level Jacobi solver due to the presence of low-frequency errors. The work of [BIB 13] shows the efficiency of using a MG method on the FEM. However, they assembled the stiffness matrix, which is very expensive for large scale problems. In this work, we propose to use the MG method with the MF-FEM to decrease the memory consumption. The MG method can alleviate the time consumption.

The process of the standard MG method is reviewed in the following scheme with a 2D two levels.

Figure 2.2 shows a typical two level V-Cycle MG scheme. We construct two levels in the same domain. The gird size on level 1, *i.e.* H, is two times larger than the size of grid on level 2, *i.e.* h. The aim is to obtain the solution on the finest grid, *i.e.* level 2. Instead of doing single level Jacobi relaxations only on level 2, one proposes to carry out relaxations on both levels. The problem is how to pass the information from one level to another level. One needs specific operators to transform residuals and corrections. This 2-level V-Cycle MG algorithms can be described as:

- Step 1: Perform pre-smoothing (relaxations) with equation (2.10) on the level 2 with the MF-FEM based iterative solver to obtain an approximated solution $\tilde{T}^h$.
- Step 2: Compute the residual r^h of each node j on level 2 by:

  $$r^h = q^h_{ex} - \sum_e \sum_m \sum_i \sum_{g=1}^{8} w_g \nabla_m \varphi_i^h \alpha^h \tilde{T}_i^h \nabla_m \varphi_j^h$$

- Step 3: Inject solutions on level 2 to level 1 on the coinciding points:

  $$\hat{T}^H = \tilde{T}^h$$

- Step 4: Restrict the residual of level 2 to level 1 by the restriction operator $\boldsymbol{R}$:

  $$q^H_{ex} = \sum_e \sum_i \sum_m \sum_{g=1}^{8} w_g \nabla_m \varphi_i^H \alpha^H \hat{T}_i^H \nabla_m \varphi_j^H + \boldsymbol{R} r_h$$

- Step 5: Carry out equation (2.10) on level 1 to obtain an approximated solution T^H on level 1.
- Step 6: Prolong the correction from level 1 to level 2 by using the prolongation operator $\boldsymbol{P}$:

  $$T^h = \tilde{T}^h + \boldsymbol{P}(T^H - \hat{T}^H)$$

- Step 7: Employ post-smoothing by equation (2.10) on level 2 with the corrected solution T^h.

From the above steps, three important operators are presented in the MG algorithms: the restriction operator $\boldsymbol{R}$, the prolongation operator $\boldsymbol{P}$ and the implicit coarse grid operator $\boldsymbol{L}$. The coarse grid operator $\boldsymbol{L}^H$ reads:

$$\boldsymbol{L}^H = \int_\Omega \nabla\phi_i^H \boldsymbol{\alpha}^H \nabla\phi_j^H \, d\Omega \tag{2.11}$$

which is a part of the formulation to compute the internal heat flux. For the FEM based MG method, the relation between R and P is:

$$R = P^T$$

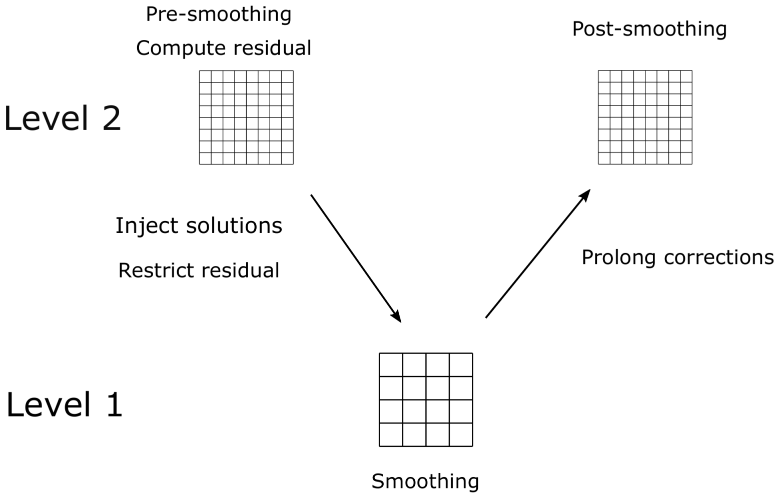

Figure 2.2: Two levels MG scheme with 2D grids ($H = 2h$)

To understand the standard restriction operator, an example of a 3D restriction operator combining 27 points is described in Figure 2.3. The goal is to take the residual from 27 points to the center point. Equation (2.12) presented the strategy of this processing.

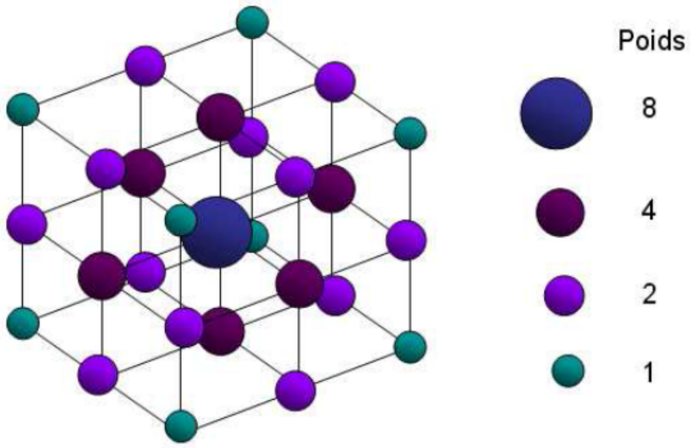

Figure 2.3: Restriction operator R and its weight [BOF 12a]

$$
\begin{aligned}
r^H_{i,j,k} = \frac{1}{64}[1 \times (&r^h_{2i-1,2j-1,2k-1} + r^h_{2i-1,2j-1,2k+1}+\\
&r^h_{2i-1,2j+1,2k-1} + r^h_{2i-1,2j+1,2k+1}+\\
&r^h_{2i+1,2j-1,2k-1} + r^h_{2i+1,2j-1,2k+1}+\\
&r^h_{2i+1,2j+1,2k-1} + r^h_{2i+1,2j+1,2k-1})+\\
2 \times (&r^h_{2i-1,2j-1,2k} + r^h_{2i-1,2j+1,2k}+\\
&r^h_{2i+1,2j-1,2k} + r^h_{2i+1,2j+1,2k}+\\
&r^h_{2i-1,2j,2k-1} + r^h_{2i-1,2j,2k+1}+\\
&r^h_{2i+1,2j,2k-1} + r^h_{2i+1,2j,2k+1}+\\
&r^h_{2i,2j-1,2k-1} + r^h_{2i,2j-1,2k+1}+\\
&r^h_{2i,2j+1,2k-1} + r^h_{2i,2j+1,2k+1})+\\
4 \times (&r^h_{2i-1,2j,2k} + r^h_{2i+1,2j,2k}+\\
&r^h_{2i,2j-1,2k} + r^h_{2i,2j+1,2k}+\\
&r^h_{2i,2j,2k-1} + r^h_{2i,2j,2k+1})+\\
8 \times &r^h_{2i,2j,2k}]
\end{aligned}
\tag{2.12}
$$

where i, j, k is the node number. r^H and r^h are residuals on the coarse grid and the fine grid, respectively. The prolongation operator is the transpose of the restriction operator. With these three operators, one can construct the full MG V-Cycle scheme. It can be described as:

1. Carry out relaxations with the MF-FEM Jacobi solver on level l.
2. Inject the solution and restrict the residual to level $l-1$ and perform relaxations on this level.
3. Repeat steps 1,2,3 from the finest grid to the coarsest grid $l=1$.
4. Prolong the correction to level $l+1$ and relax on this level.
5. Repeat step 4 until the finest level.
6. Loop step 1,2,3,4,5 until obtaining the required residual.
7. Output results

Besides the V-Cycle MG schema, W-cycle is also an often used MG scheme (see in Figure 2.5). The Full MultiGrid (FMG) cycle is another efficient MG scheme. The principle of the FMG is to start computing on the coarsest level instead of starting on the finest level, *e.g.* Figure 2.6 shows FMG cycle for a 3 level problem. For most of the applications in this work, one starts on a $4\times4\times4$ grid on level 1. The grid size on level $l+1$ is two times smaller than that of level l, *e.g.* for a problem of 2048^3 elements, one has 10 levels. ν_0 is the number of relaxations performed on level 1, ν_1 is the number of relaxations performed on each level going up. ν_2 is the number of relaxations performed on each level going down. For the FMG cycle, one uses n_{cy} V-Cycles on each level. For the initial solution of each fine level $l+1$, one does a linear interpolation of the solution of level l. Compared to the V-Cycle and the W-cycle, the FMG cycle requires more relaxations on the coarse grids. The cost of all relaxations on FMG cycles and V–Cycle is described as following.

$$W_{FMG} \leq \frac{n_{cy}}{1-(H/h)^{-d}} W_{V-Cycle} = \frac{n_{cy}(\nu_1+\nu_2)}{(1-(H/h)^{-d})^2} W_U \tag{2.13}$$

where W_U is the cost of one relaxation on the finest grid. W_{FMG} and $W_{V-Cycle}$ are the cost of FMG cycles and V–Cycle. $H/h=2$ in this work which presents the ratio between the grid size of coarse $l-1$ and fine grid l. d is the problem dimension with $d=3$ in this work. There is also the cost of transform between grids, but the problem that will be solved in this work is too large, the relaxation time is much more expensive than others routines. One accounts only the cost of relaxations on coarse grid and fine grid.

Figure 2.4 illustrates the convergence for both FMG cycles and V–Cycle on a spherical thermal conduction case with a material property contrast of 10. The MG parameter setting is: $n_{cy}=5$, $\nu_1+\nu_2=3$, $H=2h$ and $d=3$. Figure 2.4 shows that FMG cycles start by a better initial solution which is about 100 times smaller than the V–Cycle. The cost of these two types MG cycle is

$$W_{FMG} \approx 5.7\, W_{V-Cycle} < 8\, W_{Cycle}$$

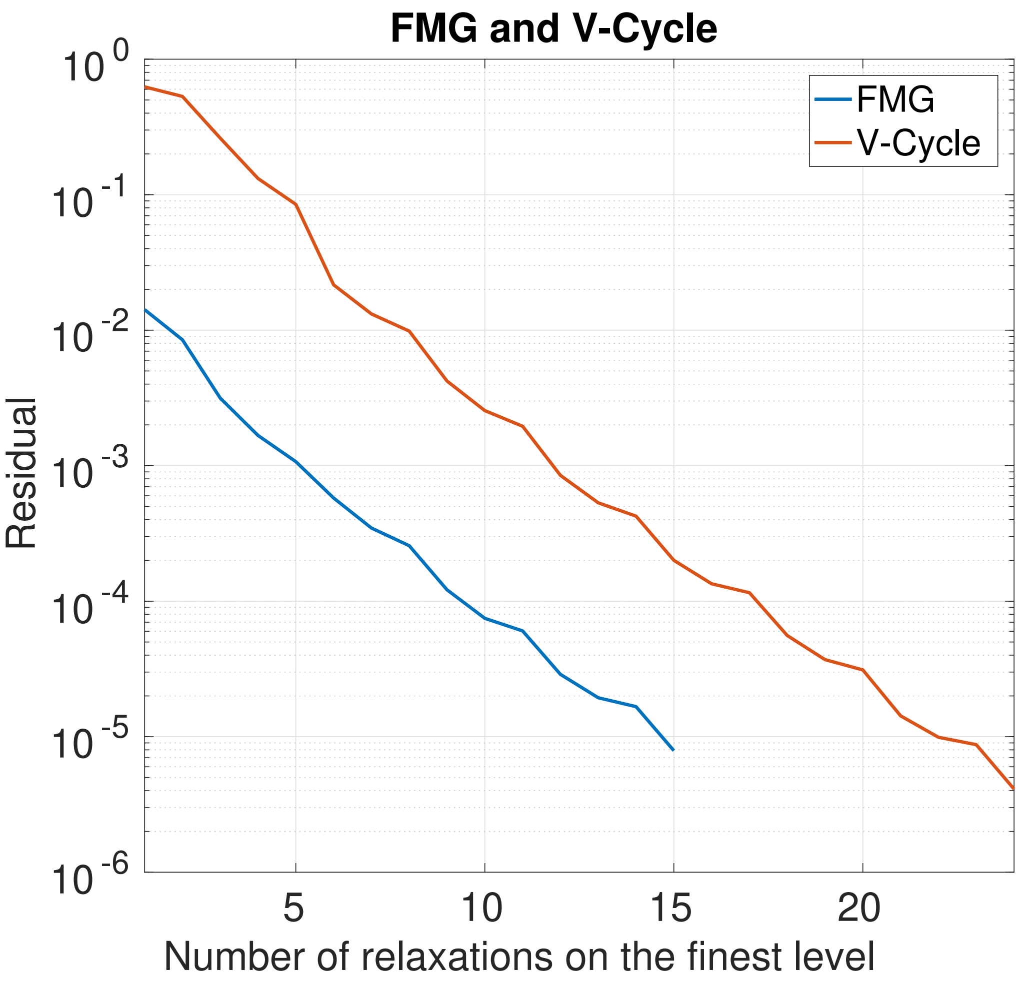

Figure 2.4: FMG cycles and V–Cycle on a spherical thermal conduction problem with a material contrast of 10

It means that to achieve the same residual, FMG cycles are more efficient than V–Cycle. We propose to use FMG cycles. For the detail of the different performances of these types of MG cycles, please see [VEN 00].

2.3.2 The MG method with large variations

Nevertheless, a standard MG method is not adapted for problems with high contrast (see [BOF 12b, BOF 14, ENG 97, GU 16]). It has a very poor convergence performance, when large variations of the material properties exist, or rather, high temperature gradients on coarse grids are involved. These variations make the linear prolongation and restriction operator almost ineffective. The material property on a coarse grid is unknown and should be chosen to avoid the poor performance of classical coarse grid and inter-grid operators.

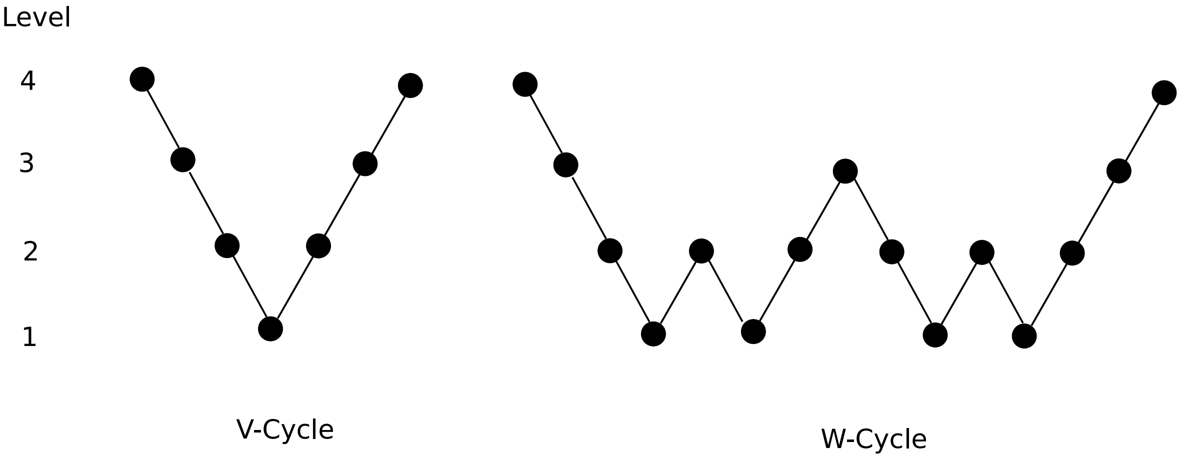

Figure 2.5: Different MG cycles (4 levels)

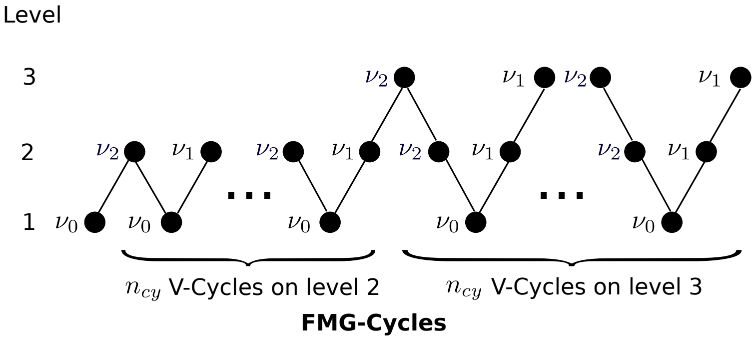

Figure 2.6: FMG Cycle (3 levels)

2.3.2.1 The coarse grid operator

To solve these problems, one needs a new coarse grid operator, prolongation operator and restriction operator. Several researchers have investigated this problem, such as the work of [ALC 81] for 2D, [HOE 98] for 3D, [ENG 96] and [ENG 97]. These researchers proposed several methods to alleviate the poor convergence of the standard MG method. But the problem is that the implementation of these ideas is not simple. The computational time and memory cost are the two other limitations. Based on the work of [ALC 81] and [SVI 15], some new operators for the MG method are proposed in this work.

[SVI 15] proposed to use a Cardwell and Parsons (CP) bounds type homogenization to obtain the analytical coarse grid operator. The idea is to compute the upper and lower CP bounds of the material property on each coarse grid from the finest grid. After that, the average of the arithmetic and geometric averages of the CP bounds, is supposed to be the effective property on each coarse grid. With this strategy, one can obtain the diagonal components of the material property tensor, which is sufficient for isotropic materials. For anisotropic materials, they proposed a method to calculate the off-diagonal components of the property tensor, please see [SVI 15] for details. With the effective material property tensor, the coarse grid operator on each level can be easily obtained by equation (2.11).

The weak point of [SVI 15] is that, the CP bounds on each coarse gird has to be computed from the finest grid. It requires too much computational time when using many grids. Therefore, one proposes to use a different homogenization technique which can be computed recursively.

Among different homogenization methods, the Voigt approximation is one of the best-known methods. In addition, it can be computed recursively. It is also referred to as the arithmetic mean:

$$\alpha_{xx}^{HV} = \frac{\sum_{k=1}^{k=N^h} \alpha_{xx}^{h}}{N^h} \tag{2.14}$$

where α_{xx}^{HV} is the diagonal component of $\boldsymbol{\alpha}^{HV}$ which is the average obtained by Voigt homogenization on the coarse grid $l-1$, α_{xx}^{h} is the diagonal component of $\boldsymbol{\alpha}^{h}$ which is the material property on the fine grid l, $x = 1,2,3$, N^h is the number of nodes on level l, which has the same volume as one element on level $l-1$.

Another approximation often used is the Reuss approximation. Equally, it can be obtained recursively, It is also known as the harmonic mean:

$$\alpha_{xx}^{HR} = \frac{N^h}{\sum_{k=1}^{k=N^h} \alpha_{xx}^{h}{}^{-1}} \tag{2.15}$$

where α_{xx}^{HR} is the diagonal component of $\boldsymbol{\alpha}^{HR}$ which is the average obtained by Reuss homogenization at the grid $l-1$.

Instead of the CP bounds, the Voigt-Reuss (VR) bounds are used in this work. Thus the effective material property tensor can be obtained recursively. The assumption is that the effective value lies within the arithmetic and geometric averages of the VR bounds.

Definition: The effective material property tensor $\bar{\boldsymbol{\alpha}}^{\boldsymbol{H}}$ is the average of the arithmetic and the geometric average of the VR bounds. It is presented as:

$$\alpha_{xx}^{H} = \frac{1}{2}\left(\alpha_{xx}^{a} + \alpha_{xx}^{g}\right) \tag{2.16}$$

where, α_{xx}^{H} is the diagonal component of $\bar{\boldsymbol{\alpha}}^{\boldsymbol{H}}$, α_{xx}^{a} is the diagonal value of the arithmetic average of the VR bounds, which is defined as:

$$\alpha_{xx}^{a} = \frac{1}{2}\left(\alpha_{xx}^{HR} + \alpha_{xx}^{HV}\right)$$

α_{xx}^{g} is the diagonal value of the geometric average of the VR bounds, which is defined as:

$$\alpha_{xx}^{g} = \sqrt{\alpha_{xx}^{HR} \cdot \alpha_{xx}^{HV}}$$

The material used in this work is supposed to be isotropic, off–diagonal values of $\bar{\alpha}^H$ are zero. The strategy to obtain the off-diagonal components is therefore not presented in this work.

An analysis of different homogenization methods (*e.g.* Voigt, Reuss, Hashin-Shtrikman, Self-Consistent) is performed. For the formulation of each method, refer to Appendix 4.5. The idea is to compute the effective thermal conductivity for a cubic structure, in which there is a spherical inclusion.

- The conductivity of the sphere is 100 W·m^{-1}·K^{-1}, 1 W·m^{-1}·K^{-1} for the other part of the cube
- The edge length of the cube is 1 m
- The radius of the sphere is between 0 m and 0.4 m

Figure 2.7 illustrates the effective conductivity obtained by different homogenization methods, when the sphere radius varies. The effective property obtained by the VR bounds lies between the Hashin-Shtrikman bounds. It confirms that the method used in this work is robust, and it can be computed level by level, so it is also efficient.

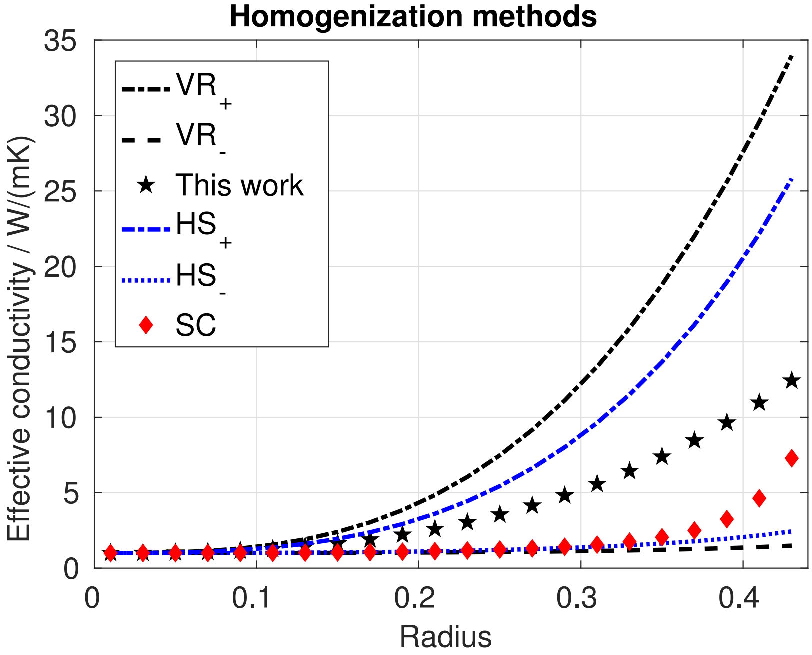

Figure 2.7: Different homogenization methods. VR_+: VR upper bound, VR_-: VR lower bound, HS_+: Hashin-Shtrikman upper bound, HS_-: Hashin-Shtrikman lower bound, SC: Self-Consistent

2.3.2.2 Prolongation and restriction operators

Besides the coarse grid operator, the prolongation and the restriction operator also need specific treatment. As mentioned above, the relation between the restriction operator (*i.e.* $\boldsymbol{R}$) and the prolongation operator (*i.e.* $\boldsymbol{P}$) is:

$$\boldsymbol{P} = \boldsymbol{R}^T \tag{2.17}$$

So here, we present only the prolongation operator $\boldsymbol{P}$, the restriction operator $\boldsymbol{R}$ can then be obtained automatically.

The work of [BOF 14] presents the principle to derive P and R. The point is to consider the material discontinuities. The prolongation process will be briefly presented in this work.

As illustrated in Figure 2.8, the big box with solid edges represents one element on the coarse grid $l-1$, and the eight small boxes with dotted edges are the eight elements on the fine grid l. The temperature correction e, at each "black" node (*e.g.* $A1$, $A2$) of the coarse grid is known. The goal is to obtain the temperature correction at all the 27 nodes of the fine grid. For the temperature correction at the eight "black" nodes of the fine grid coinciding with the ones on the coarse grid, one performs an injection, which means:

$$e^l_{A1} = e^{l-1}_{A1} \tag{2.18}$$

For the other nodes, instead of the linear prolongation of the standard MG method, the nodal material property is taken into account. It reads as follows.

For the "red" nodes (Figure 2.8) located at the center of the edge between two coarse grid nodes (*e.g.* node $B1$):

$$e^l_{B1} = \frac{\alpha_{A1}e^{l-1}_{A1} + \alpha_{A2}e^{l-1}_{A2}}{\alpha_{A1} + \alpha_{A2}} \tag{2.19}$$

For the "blue" nodes, which are located at the center of each face of the big box (*e.g.* node $C1$):

$$e^l_{C1} = \frac{\alpha_{B1}e^l_{B1} + \alpha_{B2}e^l_{B2} + \alpha_{B3}e^l_{B3} + \alpha_{B4}e^l_{B4}}{\alpha_{B1} + \alpha_{B2} + \alpha_{B3} + \alpha_{B4}} \tag{2.20}$$

For the "yellow" center node of the big box (*e.g.* node O):

$$e^l_{O} = \frac{\alpha_{C1}e^l_{C1} + \alpha_{C2}e^l_{C2} + \alpha_{C3}e^l_{C3} + \alpha_{C4}e^l_{C4} + \alpha_{C5}e^l_{C5} + \alpha_{C6}e^l_{C6}}{\alpha_{C1} + \alpha_{C2} + \alpha_{C3} + \alpha_{C4} + \alpha_{C5} + \alpha_{C6}} \tag{2.21}$$

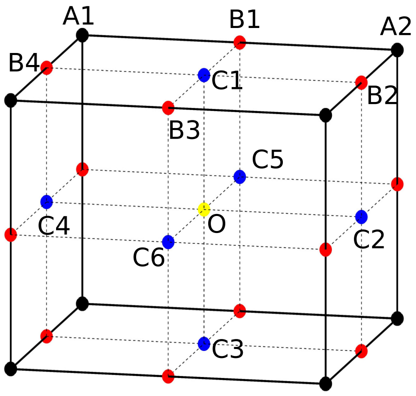

Figure 2.8: Prolongation scheme

2.3.2.3 FMG cycle with homogenization technique and its performance

The FMG cycle with the proposed homogenization technique for a 3-level problem can be therefore described as:

1. Compute the Voigt and the Reuss approximations on each level, respectively; obtain the effective material properties $\boldsymbol{\alpha}^{\boldsymbol{H}}$ for all levels besides the finest level, which exhibits the real material properties.
2. Carry out relaxations with the Jacobi solver on the coarsest level 1.
3. Employ linear interpolation of the level 1 solution to level 2.
4. Perform V-Cycles with these two levels until the required residual on level 2.
5. Employ linear interpolation of the level 2 solution to level 3.
6. Perform V-Cycles with these three levels until the required residual on level 3.
7. Output results

For a problem with more than 3 levels, one repeats the interpolation step and V-Cycles until the required level.

2.3.3 Efficiency of the proposed MG strategy

The performance of the MG method compared to the single level Jacobi solver is studied below. One carries out a simulation on a spherical thermal inclusion problem with a conductivity of 10 W$\cdot$m$^{-1}\cdot$ K^{-1} for the sphere and 1 W$\cdot$m$^{-1}\cdot$ K^{-1} for the other part of the cube. The sphere radius is a quarter of the size of cube. The domain Ω is discretized with 128^3 (more than two million) elements. The boundary conditions are set according to equation (2.3). The simulation is run on an office computer equipped with one processor ”Intel(R) Core(TM)2 Quad CPU Q9650 @ 3.00GHz”. For the single level iterative relaxation, the Jacobi relaxation is applied directly on this 128^3 grid problem. For the MG scheme, one has 6 levels for this 128^3 grid problem with a coarse level of 4^3 elements. ν_0, ν_1, ν_2, n_{cy} are set to be 10, 1, 2 and 5, respectively. Three different values for the relaxation coefficient ω, *i.e.* 0.5, 1.0 and 1.5, are used for both simulations.

	Single level	MG scheme
Residual achieved	1.55×10^{-2}	7.89×10^{-6}
Cost / W_U	4139	19.6

Tableau 2.1: Comparison between single level relaxation and a MG scheme

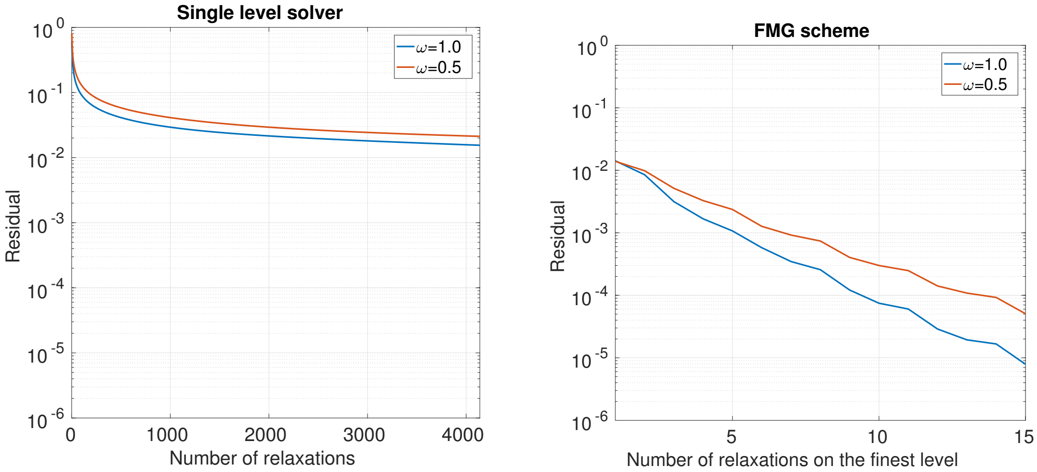

(a) Single level

(b) FMG scheme

Figure 2.9: Convergence of the Jacobi solver (a) and FMG scheme (b) on a 129^3 nodes problem

Table 2.1 and figure 2.9 illustrate the performance of the MG scheme and the single level Jacobi solver. The convergence rate of the single level Jacobi solver decreases rapidly both for damped Jacobi with ω=0.5 and normal Jacobi with ω=1.0. On the other hand, the convergence rate of the MG scheme remains constant with ω=0.5 and ω=1.0. For the case of over relaxation *i.e.* ω=1.5, it diverges with both methods for this problem. With a ω=1.0, one has the best convergence performance for the MG scheme. After 4139 relaxations, the single level Jacobi relaxation does not yet reach the initial solution of FMG cycle on the finest level. It confirms that one has a good initial solution for the finest level with FMG cycles. The MG scheme costs about 211 times lower, with a residual 10 000 times smaller than the single level Jacobi solver.

To demonstrate the efficiency of the proposed MG method in front of the standard MG method, several numerical simulations are employed.

The idea is to compare the convergence performance between the classical MG and the proposed MG method. Compared to the classical Geometric MultiGrid (GMG), the proposed method has two differences:

- Instead of the linear prolongation and restriction operators, one proposes to consider the material properties for the prolongation and restriction operators.
- A homogenization technique is used in the proposed method to obtain material properties on the coarse grid. However, in the classical GMG, a simple average, *i.e.* Voigt approximation, is used to obtain material properties on the coarse grid.

According to the difference between a classical GMG and the proposed MG, one carries out three simulations for the spherical case with a material property contrast of 1 000 (detailed in section 3.3.2) and for the composite case (detailed in section 3.3.4).

- **GMG-A**: Linear restriction and prolongation operators, Voigt approximation of the material properties on the coarse grids
- **GMG-H**: Linear restriction and prolongation operators, homogenized material property on the coarse grids
- **Proposed method**: Considering material property for restriction and prolongation operators, homogenized material properties on coarse grids

As illustrated in Figure 2.10(a) and 2.10(b), these three methods converge for both the spherical and the composite case. For the spherical case, both the proposed method and GMG-H have the best performance. For the composite case, the proposed method has the best performance. For both cases, it shows that the coarse grid material property has a large influence on the convergence speed, a representative material property for coarse grid is highly important to ensure good convergence. The idea to includes the material property for the prolongation and the restriction operator does not always have a large improvement, for some symmetrical case, *e.g.* spherical inclusion, it does not have a large improvement compared to GMG-H. But for the most complex case *e.g.* for a composite material, it has a good performance. Since the aim of the proposed algorithm is to deal with complex materials with large material property variations, the proposed algorithms are more efficient.

2.4 High performance computing

The proposed strategy permits one to have a good and efficient convergence. However, for an image with 2049^3 voxels, even carrying out one relaxation on the finest level requires a

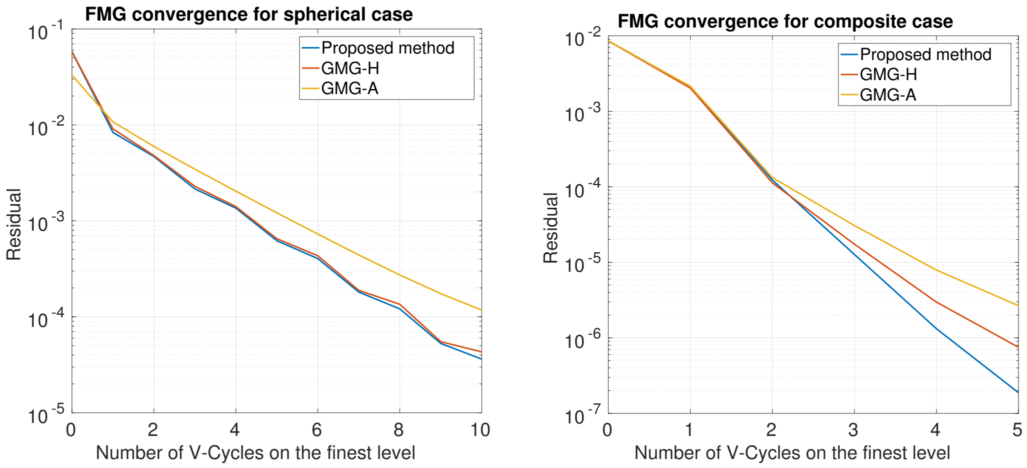

(a) Spherical case (b) Composite case

Figure 2.10: Convergence of the MG method with different intergrid operators

lot of time and memory. Fortunately, high performance computing (HPC) can be of help.

To apply numerical simulations on supercomputers, special programming methods are needed according to the supercomputers architecture. Three well-known parallel programming methods are Message Passing Interface (MPI), Open Multi-Processing (OpenMP), Compute Unified Device Architecture (CUDA). MPI and OpenMP are specially used on CPUs. CUDA is reserved for GPUs. MPI is designed to provide both the point-to point and collective communications among distributed memory machines. It was invented for massively parallel computing. OpenMP is proposed for shared memory multi-platform. For more details about the MPI, OpenMP, please refer to [AUB 11] and [KAR 03]. All of these three programming have a good performance for different machine architectures. To choose the final programming method, one shall first take acknowledge of the available supercomputer.

The architecture of the available machine is the supercomputer ”Liger” at Centrale Nantes. As presented in Figure 2.11, Liger has a hierarchical hardware design, which composes of many nodes. Each node consists of 2 processors (*i.e.* sockets) with a total RAM of 128 GB and each processor is constituted by 12 cores. It is therefore a Multi-Core/Multi-Socket supercomputer. Liger is also equipped with graphic cards to support CUDA, but it is too limited compared to its CPU ability. Since the aim of this work is to solve a 2048^3-element problem, large memory is essential. Pure OpenMP can only ensure 128 GB of RAM, which is not sufficient. Moreover, OpenMP only can not ensure a sufficient speedup. MPI programming allows one to have a massively parallel programming with large memory and sufficient speedup. For the available machine, the maximum number of cores can be used is fixed at 1000 by the owner, which allows us to have a sufficient speedup and memory space for this work.

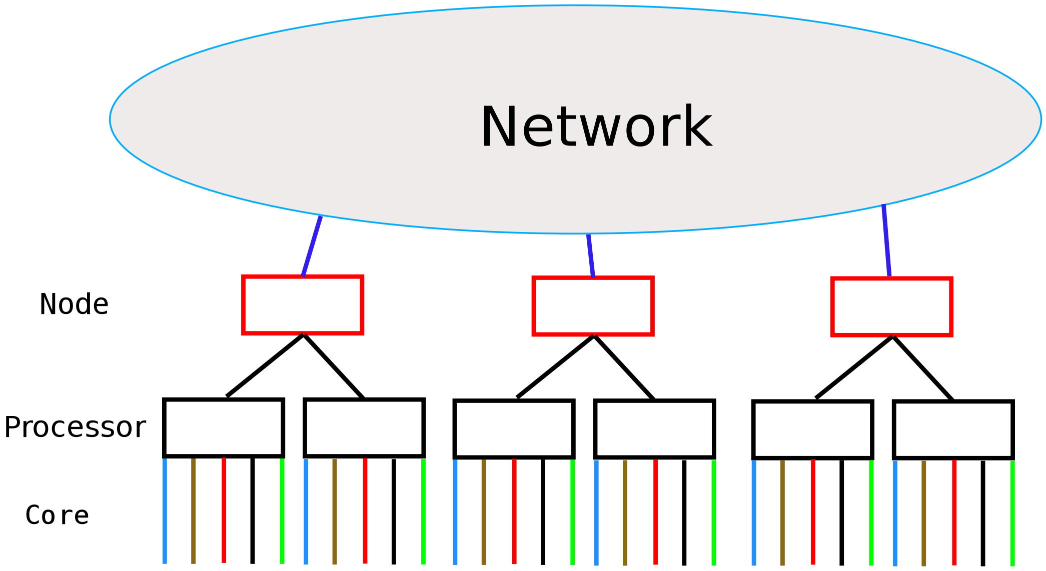

Figure 2.11: Supercomputer architecture

2.4.1 Hybrid MPI+OpenMP

MPI seems to be a good choice for this work. it has a good performance. However, with a MG method, one can have a large limitation for the parallel computing. The coarsest MG gird often starts by a 4^3 grid, which means that on the coarsest level, it does not permit one to use as many MPI as we want. Researchers developed several strategies to avoid such problems. Some researchers propose to compute the entire coarse grid solution in each MPI task and only partition the fine grid simulations into different MPI tasks, since it is the fine grid which is time consuming. Another solution is to change the number of MPI tasks during the computation. For the coarse gird, one uses only one MPI core and lets other cores ”sleep”. For the fine grid, one uses all the MPI cores. Both these two options are not simple to implement. Beside these two options, another often used strategy is the Hybrid MPI+OpenMP, see [GAH 12], [NAK 12] and [BER 06].

Hybrid MPI+OpenMP programming is designed by researchers to achieve a better performance. Rabenseifner *et.al.* [RAB 09] found that compared to pure MPI and pure OpenMP, a hybrid programming model is the superior solution because of memory consumption and reduced communication requirements. Since the available machine is a hierarchical machine, it allows us to use Hybrid MPI+OpenMP programming. MPI is applied for the inter-zone parallelization and OpenMP is applied for the intra-zone parallelization. The hybrid programming can also reduce the number of output files, which can minimize the visualization problem. *e.g.* To use 640 cores, instead of using 640 MPI tasks which creates 640 small output files, one uses 64 MPI with 10 OpenMP per MPI task, the number of output files reduces to 64.

The Hybrid MPI+OpenMP implementation is chosen for this work. As mentioned previously, for a problem with 4^3 elements on the coarse grid, the maximal number of MPI can be used is 64. For large problems, in order to have a good speedup, the idea is to use one MPI on one socket and 12 OpenMP on each socket. In this way, one cam have 768 cores working simultaneously. The option of using one MPI per node and 24 OpenMP per MPI permits to use more cores. But it is does not give a good performance, since OpenMP has a poor performance when accessing data between two sockets.

2.4.2 Domain decomposition and communication

For both MPI pure programming and Hybrid MPI+OpenMP programming, the part of MPI is fundamental. To apply MPI, the first step is to decompose the domain. The way to decompose the computational domain has a significant influence on the speedup. The optimum option is to let all the MPI tasks have an identical workload, *i.e.* the number of unknowns to be computed is identical in each MPI task.

The domain Ω in this work is cubic. One proposes to use a 3D domain decomposition (see Figure 2.12). A 2D example is presented to explain it. As illustrated in Figure 2.13, a 2D 6×6 grid problem is separated into 9 MPI tasks. All the tasks are named as (0, 0), (0, 1), ... , (2, 2). Each MPI task calculates a 2×2 grid problem. To obtain the unknown on an elementary node, it needs the residual of all the four elements which are connected with this node. For the center node, *e.g.* node O, it has all his neighbors to accomplish its computation in task (1, 1). For nodes on boundaries, *e.g.* node A, their neighbors are not in processor (1,1). To obtain the value of the unknown on node A, elements e_1, e_2, e_3 and e_4 are required. However, since it is a distributed memory supercomputer, one does not have directly data access to another computer node. The strategy is to create "ghost" elements in task (1, 1). As shown in Figure 2.13, elements $e_2^{'}$, $e_3^{'}$ and $e_4^{'}$ are virtually the same as elements e_2, e_3 and e_4 in task (0, 1), (0, 2) and (1, 2), respectively. To computer all the unknowns, other "ghost" elements are also needed. Figure 2.13 shows all the "real" elements and "ghost" elements for this 2D example.

After the first relaxation in each MPI task, values on all nodes of elements e_2, e_3 and e_4 are updated. But their "ghost" elements still have "old" values, which can not be updated. To ensure the value of $e_2^{'}$, $e_3^{'}$ and $e_4^{'}$ be updated before the second relaxation, one needs the MPI to do communication job. The idea is to send the updated value to each ghost points. For the previous 2D example, each processor has to communicate with all the surrounding processors. If one does it point by point, the implementation and communication process will be too complicated. To simplify the communication strategy, many researchers investigated in this subject. One proposes to use the MPI topology (see in [GRO 99] and [TRA 02]). The idea is to create a virtual topology that represents the way that MPI processes communicate. As the domain is decomposed into a regular 3D cube, Cartesian topology is used. A 3D coordinate (n_{p_x},n_{p_y},n_{p_x}) is then assigned to each MPI task. To organize the communication and to simplify the implementation, three communicators representing three directions are created. The derived datatypes are also constructed to create communication "box", *i.e.* a group of data. A 2D example is presented here to

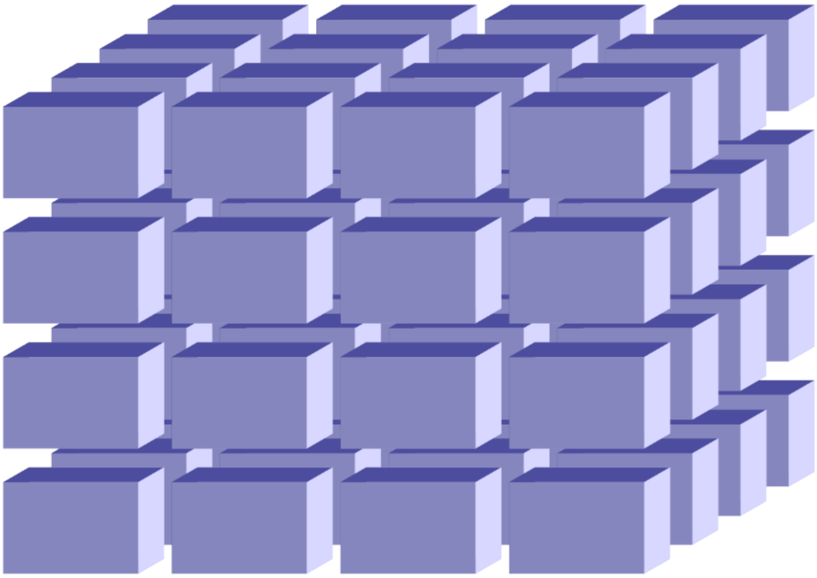

Figure 2.12: 3D decomposition. IDRIS presentation

have an idea about the communication. Figure 2.14 shows the communication process for a 2D problem with 4 MPI tasks. Figure 2.15(a) presents the situation after one relaxation. As we can observe, the value on all the ghosts points shall be updated before the second relaxation. The first step is to communicate in the vertical direction. As illustrated in Figure 2.14(a), in each MPI task one line of values is sent to the neighbor MPI in the vertical direction by using the communicator in this direction. After the first communication, the value on each point is presented in Figure 2.15(b). The second communication is in the horizontal direction (see Figure 2.14(b)), one sends one line of values in each MPI task to its horizontal neighbor. The final updated ”ghost” points are shown in Figure 2.15(c). For 3D problems, one needs one communication per direction, *i.e.* three communications in total.

During the MG scheme, communications are carried out after each relaxation to update the solution. It is carried out after each restriction of residual to update the residual on ”ghost” points. It is also used after each prolongation step.

For the input part, since the tomography image is not too large *e.g.* about 8 GB for an image with 2049^3 voxels, one requires each MPI task to read the entire image and to take the part that it needs. For the output part, the float type data is used in the binary VTK format files. One requires each MPI task to output only the ”real” element part. A pVTK file is created by the master process for the post-processing.

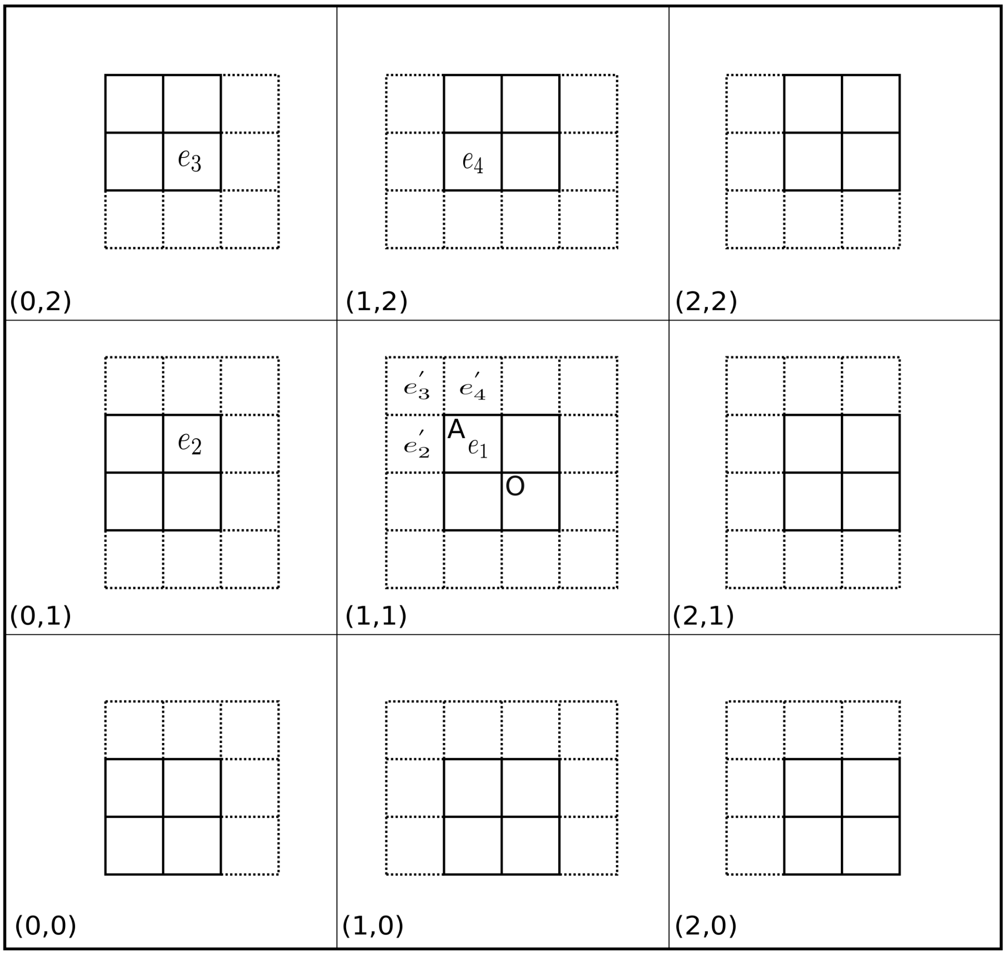

Figure 2.13: A 2D domain decomposition for a 6×6 grid problem and its MPI topology. Solid lines denote ”real” elements, Dashed lines represent ”ghost” elements

2.4.3 HPC performance

The performance of the proposed HPC strategy is analyzed by solving a problem containing 1024^3 elements.

For the performance of the hybrid programming, two parameters have to be investigated: the number of MPI and the number of threads per MPI task. As mentioned previously, each processor has 12 cores for the available machine, and each node has 2 processors. In order to have a good efficiency, the number of threads per MPI is limited by 12 to avoid the use of OpenMP between two sockets, since OpenMP suffers from poor data access patterns when using two sockets. The maximum number of cores that can be used is 1 000 fixed by the owner. As presented in Figure 2.16, one simulation with 1 core

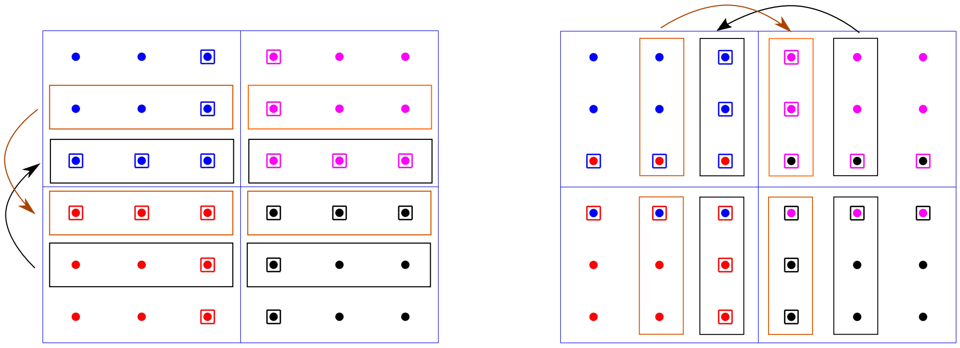

(a) First communication (b) Second communication

Figure 2.14: Communication processing for a 2D problem (Rectangle with a inner point donates ghost point)

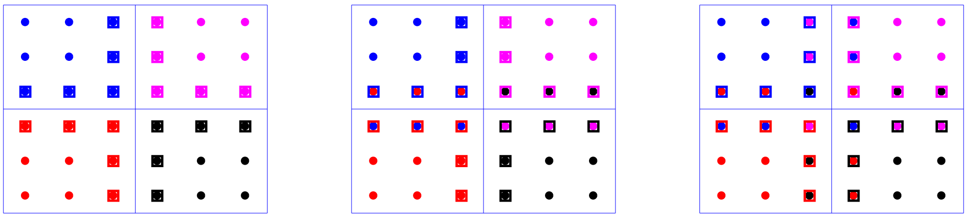

(a) Before communication (b) After 1^{st} communication (c) After 2^{nd} communication

Figure 2.15: Communication result for a 2D problem (Rectangle with a inner point donates ghost point)

and 1 MPI is carried out to have a reference to compute the speedup. The number of MPI is set to 1,2,4,8,16,32 and 64. 12 threads are used in each MPI task. This curve illustrates that for a 1024^3 problem, even with 768 cores, a good speedup is obtained. Within this number of cores, the speedup increases linearly as the number of cores increasing. Furthermore, the speedup is closed optimal at 80%.

Besides the number of cores that has a big influence on the parallel performance, the configuration of the number of MPI and the number of OpenMP can also have an influence. *i.e.* for 384 cores, one has the following configurations: 32 MPI with 12 threads, 48 MPI with 8 threads, 64 MPI with 6 threads, 96 MPI with 4 threads, 128 MPI with 2 threads.

Simulations for three different configurations, *i.e.* 32 MPI with 12 threads, 48 MPI with 8 threads and 64 MPI with 6 threads, are carried out for a problem with 1024^3 elements. As presented in table 2.2, with 48 MPI and 8 threads per MPI, one has a poor performance. Since in one node, there are 3 MPI which means there is at least one

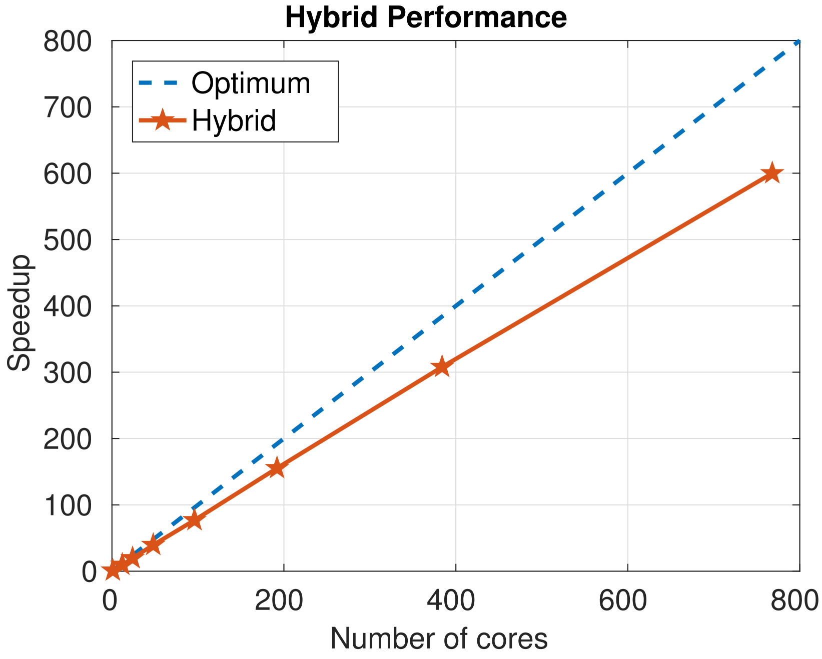

Figure 2.16: Parallel performance of the proposed hybrid strategy

Configurations	Time / s
32 MPI, 12 threads	480
48 MPI, 8 threads	726
64 MPI, 6 threads	463

Tableau 2.2: Comparison between different configurations

MPI using cores from two sockets. With 64 MPI and 6 threads per MPI, one obtains a better performance than that with 32 MPI and 12 threads, but the difference is only $\frac{480-463}{463} \approx 4\%$. It confirms that nevertheless the current program does not allow one to use as many MPI tasks as we want, a sufficient performance is obtained. For a problem with 2024^3 elements, using 12 cores for each of the 64 MPI, *i.e.* 768 cores in total, one can already accomplish the simulation in about 3 hours.

2.5 Conclusion

This chapter introduced the basics of the thermal conduction problem. The notation of the finite element method and the MultiGrid method were reviewed. A new efficient strategy of using a MF-FEM type MG with homogenization techniques was proposed. The comparison of the proposed strategy with the single level Jacobi solver and with the standard MG method confirmed its efficiency. The massively parallel programming was also presented with an efficiency of 80%. With all of the proposed steps, one can finally carry out massively parallel thermal conduction simulations on real images of heterogeneous materials at the microscopic scale.

Chapter 3

Thermal conduction applications using tomographic images

Contents

The main content of this chapter is adapted from our published paper [LIU 19].

3.1 Introduction

The major part of this chapter is about the computational homogenization method and its applications. Several applications of the proposed strategy are demonstrated. The computational homogenization with the proposed MG strategy is firstly introduced in section 3.2. Section 3.3 reveals the validation of the proposed method and its applications on industrial materials.

3.2 The homogenization method and the effective material property

The material behavior is determined by its microscopic structure. However, for industrial applications, the main interest is to know its macroscopic behavior. Researchers found a straightforward way to analyze the macroscopic properties of materials. The homogenization method is invented on the background. Nowadays, there are the analytical homogenization method and the numerical homogenization method. The well-known analytical homogenization methods, *e.g.* Hashin-Shtrikman bounds, Mori-Tanaka methods, self-consistent method, etc., are often used for structured or regular materials. For complex heterogeneous materials, the numerical homogenization method does a better job than the analytical homogenization method. The following part presents the strategy of the application of the proposed method on the numerical homogenization method.

As presented in the work of [ÖZD 08], the idea is to consider the entire domain Ω to be one element, which is also referred to be a Representative Volume Element (RVE). The principle of RVE homogenization is briefly presented below.

The well known Fourier's law is described as:

$$-\boldsymbol{A}\cdot\nabla\theta = Q \tag{3.1}$$

where, $\boldsymbol{A}$ is the effective thermal conductivity at the macroscopic scale, θ is the temperature at the macroscopic scale. $\nabla\theta$ is the temperature gradient and Q is the total heat flux at the macroscopic scale, which can be computed from the local heat flux with the following equation:

$$Q = \frac{1}{V}\int_V q\,dv = -\frac{1}{V}\int_V \alpha\nabla T\,dv \tag{3.2}$$

With the specific boundary conditions, one can obtain $\boldsymbol{A}$. In this work, one suggests to apply the following boundary conditions:

$$\begin{cases} \nabla\theta_x & = 1\,\mathrm{K{\cdot}m^{-1}} \\ \nabla\theta_y & = 0 \\ \nabla\theta_z & = 0 \\ T & = \nabla\theta_x x \text{ on } \partial\Omega \end{cases} \begin{cases} \nabla\theta_x & = 0 \\ \nabla\theta_y & = 1\,\mathrm{K{\cdot}m^{-1}} \\ \nabla\theta_z & = 0 \\ T & = \nabla\theta_y y \text{ on } \partial\Omega \end{cases} \begin{cases} \nabla\theta_x & = 0 \\ \nabla\theta_y & = 0 \\ \nabla\theta_z & = 1\,\mathrm{K{\cdot}m^{-1}} \\ T & = \nabla\theta_z z \text{ on } \partial\Omega \end{cases} \tag{3.3}$$

respectively. $\nabla\theta_x$, $\nabla\theta_y$ and $\nabla\theta_z$ are the temperature gradients in the X, Y and Z direction, respectively. With each boundary condition, one column of $\boldsymbol{A}$ can be obtained. The three columns of $\boldsymbol{A}$ can finally be obtained by these three simulations.

3.3 Validation and applications

3.3.1 Validation

A multi-layer problem is used to validate the proposed solver. The domain Ω: $1.0 \times 1.0 \times 1.0$ cm^3, consists of four uniform layers. The thermal conductivity of each layer is: $\alpha_1 = 1$ W$\cdot$m$^{-1}\cdot$ K^{-1}, $\alpha_2 = 4$ W$\cdot$m$^{-1}\cdot$ K^{-1}, $\alpha_3 = 8$ W$\cdot$m$^{-1}\cdot$ K^{-1} and $\alpha_4 = 4$ W$\cdot$m$^{-1}\cdot$ K^{-1}. The distribution of these four materials is presented in Figure 3.1. Boundary conditions are applied as mentioned in equation (2.3). $T_1 = 0$ K and $T_2 = 1$ K are applied.

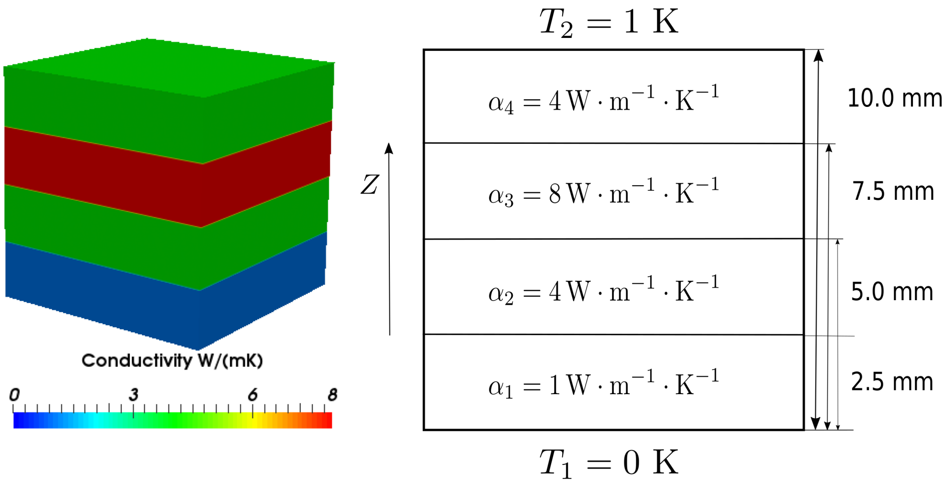

Figure 3.1: Boundary conditions on the multi-layer structure and its conductivity

The analytical solution of this problem is described as:

$$T(z) = \begin{cases} \frac{32}{13} z & \text{for } 0 \leq z < 0.25\,\text{cm} \\ \frac{8}{13} + \frac{8}{13}(z - 0.25) & \text{for } 0.25\,\text{cm} \leq z < 0.5\,\text{cm} \\ \frac{10}{13} + \frac{4}{13}(z - 0.50) & \text{for } 0.5\,\text{cm} \leq z < 0.75\,\text{cm} \\ \frac{11}{13} + \frac{8}{13}(z - 0.75) & \text{for } 0.75\,\text{cm} \leq z \leq 1.0\,\text{cm} \end{cases} \tag{3.4}$$

where z is the coordinate of the Z axis.

To validate the numerical solution, the error between the analytical and the numerical solution is computed. However, the FEM has a discretization error, the number of elements used to obtain the numerical solution affects the error between the analytical and the numerical solution. As a result, on one side, the error between the analytical and the numerical solution is studied; on the other side, the FEM discretization error is studied.

For the numerical solution, one discretizes Ω into $128 \times 128 \times 128$ (*i.e.* more than two million) cubic elements, and applies the same boundary conditions as for the analytical solution and carries out the simulation. The coarsest level has 4×4×4 elements, for each finer level, the grids size is devised by two *i.e.* 6 levels for a 128^3 problem. Figure 3.2 shows the temperature variations of the analytical and the numerical solution, respectively, along the Z direction. The temperature obtained by the numerical simulation is almost the same as the one obtained by the analytical solution. The L_2 error norm between the analytical solution and the numerical solution is 0.0027.

To analyze the influence of the element size, one discretizes Ω with $16 \times 16 \times 16$, $32 \times 32 \times 32$ and $64 \times 64 \times 64$ elements and computes the L_2 error norm compared to the analytical solution, respectively. Figure 3.3 shows the l_2 error norm as a function of element size. The L_2 norm error decreases almost linearly in log-log scale with the element size. The accuracy increases by a factor of 2 when the element size decreases, which confirms to the accuracy obtained for the large variation cases with MultiGrid methods.

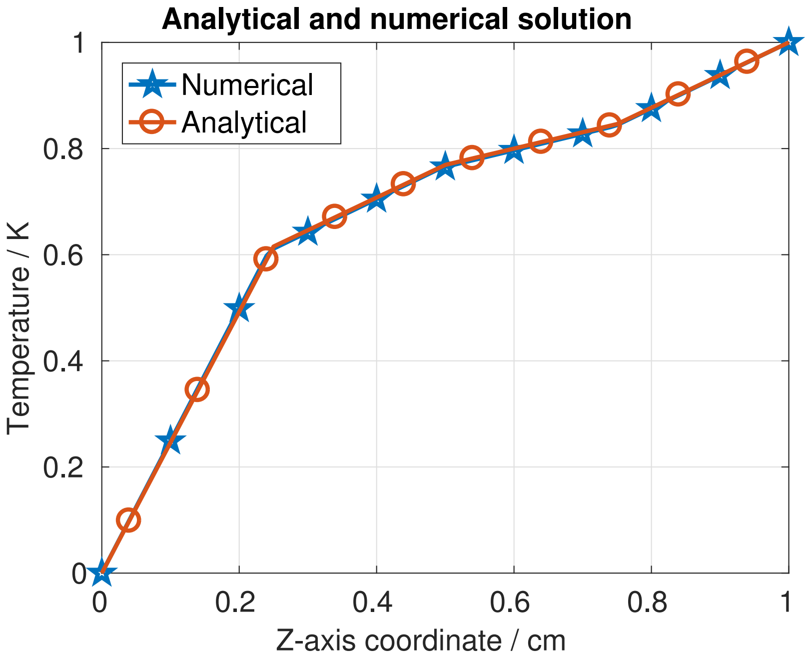

Figure 3.2: Temperature variation in Z direction of the analytical (Red) and the numerical (Blue) solution

The analytical and numerical solution show that the strategy of using the MG method coupled with homogenization technique can deal with problems with varying coefficients.

3.3.2 Spherical inclusion

The stability of the proposed method is analyzed in this subsection, when it handles a spherical inclusion problem with large material property variations.

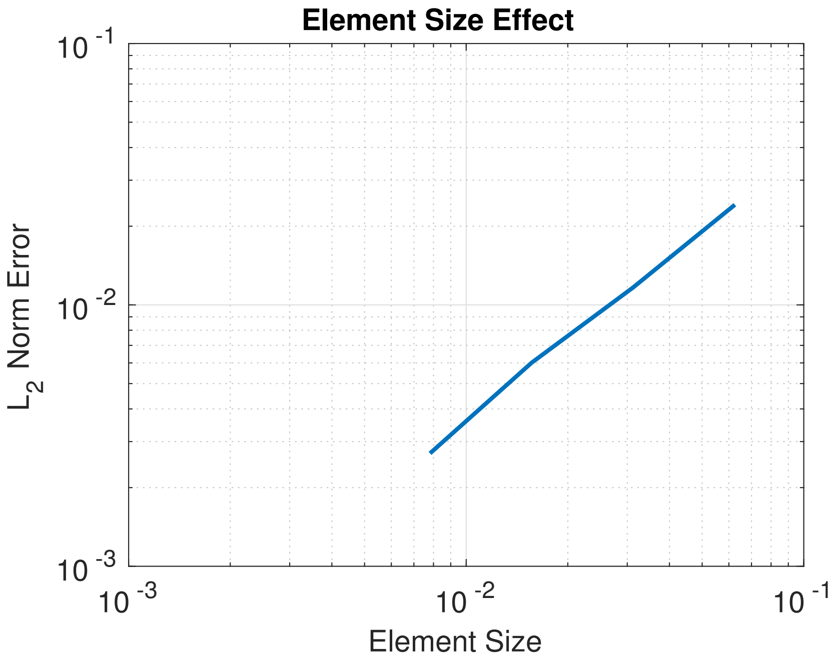

Figure 3.3: L_2 norm error analysis

The domain Ω is a cube, which has two materials, as presented in figure 3.4(a). The radius of the inclusion is $R = \frac{L}{4}$, where, L is the size of cube. The thermal conductivity of the material in the sphere is 1 000 $\mathrm{W{\cdot}m^{-1}{\cdot}K^{-1}}$, whereas it is set to 1 $\mathrm{W{\cdot}m^{-1}{\cdot}K^{-1}}$ in the other part. The contrast between these two materials is 1 000. One discretizes the cube with $128 \times 128 \times 128$ cubic elements. The boundary conditions are presented in the following equation.

$$\begin{cases} T = 0\ \mathrm{K} & \text{on } \Gamma_1 \\ T = 1\ \mathrm{K} & \text{on } \Gamma_2 \\ \alpha \nabla T \cdot \vec{n} = \mathbf{0} & \text{on the other surfaces} \end{cases}$$

The coarsest starts always by a $4{\times}4{\times}4$ grid. ν_0, ν_1, ν_2, n_{cy} are set to be 100, 4, 8 and 10, respectively.

Figure 3.4(b) shows the temperature gradient in Ω. The large variation of the conductivity on the interface explains the large variation of the temperature gradient around the interface.

This application confirms the good stability of this strategy in case of large variations of material properties.

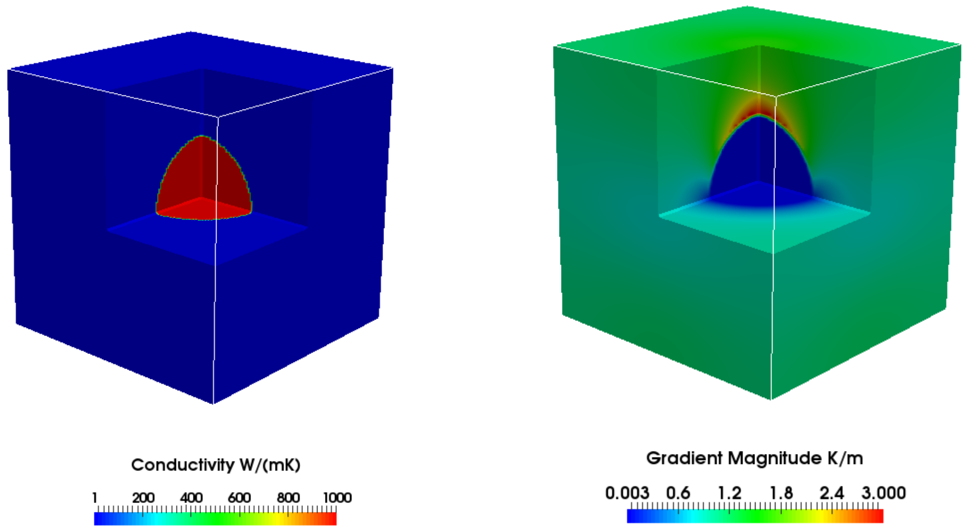

(a) Conductivity

(b) Temperature gradient

Figure 3.4: Conductivity in Ω and its temperature gradient field

3.3.3 Nodular graphite cast iron image

Nodular graphite cast iron is a well-known and widely used material in the industrial domain. The prediction of the conductivity of cast iron is a significant difficulty for researchers. Several papers investigate the conductivity, *e.g.* [HEL 91] regarded cast iron as a composite material and created a model to predict its conductivity. Nevertheless, since the distribution of carbon nodules in cast iron affects its conductivity, the property of cast iron is different for different manufacturers. One proposes to use X-ray tomographic techniques to obtain the carbon nodules distribution in an image format. The numerical simulation is then employed on this image to analyze the influence of carbon nodules and to obtain the effective conductivity of cast iron.

The original tomographic image of cast iron is an image with $512 \times 340 \times 340$ voxels [RAN 10]. The voxel size is 5.06μm. The region of interest (ROI) in this work is a part of this image. This part has $257 \times 257 \times 257$ (more than 16 million) voxels. Each voxel is supposed to be one elementary node of the FEM discretization. A conductivity is assigned to each node. Figure 3.5(a) illustrated the ROI with gray level, where the carbon nodule is obvious. To go from the gray level in the tomographic image to material properties, the thresholding method is applied as presented in Figure 3.5(b). With this strategy, the volume fraction of carbon nodules corresponds to the volume fraction provided in [RAN 10]. Figure 3.6(a) illustrates the conductivity of the two components in cast iron, where, the black nodules in this image are the carbon nodules. The carbon conductivity is 129.0 W$\cdot$m$^{-1}\cdot$ K^{-1}, for the other part, one takes the conductivity of iron which, is 80.4 W$\cdot$m$^{-1}\cdot$ K^{-1}.

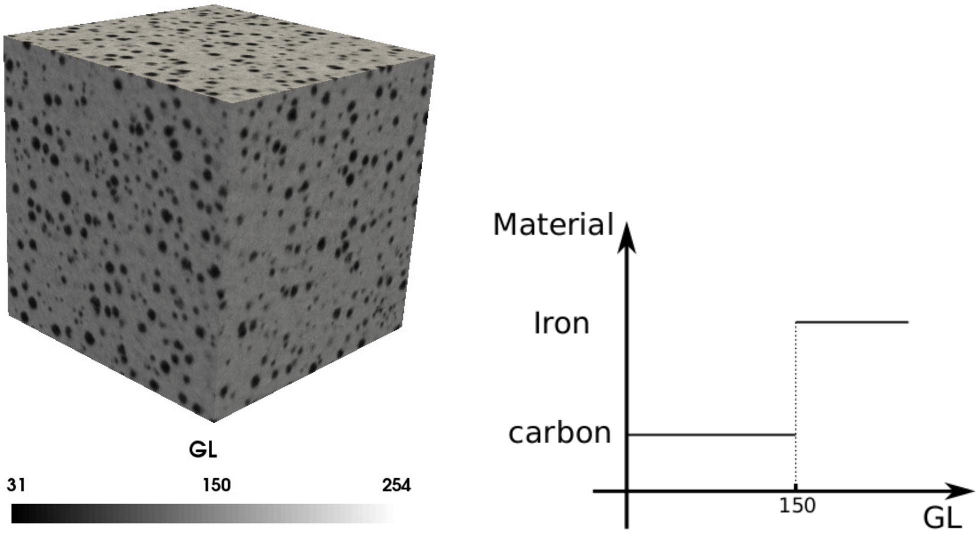

(a) Gray level

(b) Thresholding function

Figure 3.5: The gray level on each voxel, where *GL* is the original value of each voxel obtained by X–Ray tomography, which is an integer between 0 and 255.

To obtain the effective conductivity of the cast iron, the homogenization method is used. The boundary condition is applied as equation (3.3). For the FMG Cycle, 7 levels are used, ν_0, ν_1, ν_2, n_{cy} are set to be 10, 2, 1 and 5, respectively. Figure 3.6(b) shows the distribution of the temperature gradient in the case iron with the boundary conditions in equation 3.5. This figure presents that inclusions in cat iron can be considered as many small spherical inclusions in cast iron. The location of the inclusions where there are small temperature gradient, coincides with the location of carbon nodules whose conductivity is larger. On the two poles of inclusion in the gradient direction, a large temperature gradient is located. This confirms to the spherical inclusion.

$$\begin{cases} \nabla\theta_x & = 0 \\ \nabla\theta_y & = 0 \\ \nabla\theta_z & = 1\,\mathrm{K{\cdot}m^{-1}} \\ T & = \nabla\theta_z z \text{ on } \partial\Omega \end{cases} \tag{3.5}$$

The effective conductivity obtained is:

$$\boldsymbol{A} = \left\{ \begin{array}{ccc} 82.4311 & 0.0020 & 0.0040 \\ 0.0020 & 82.4223 & -0.0026 \\ 0.0040 & -0.0026 & 82.4277 \end{array} \right\} \mathrm{W \cdot m^{-1} \cdot K^{-1}}$$

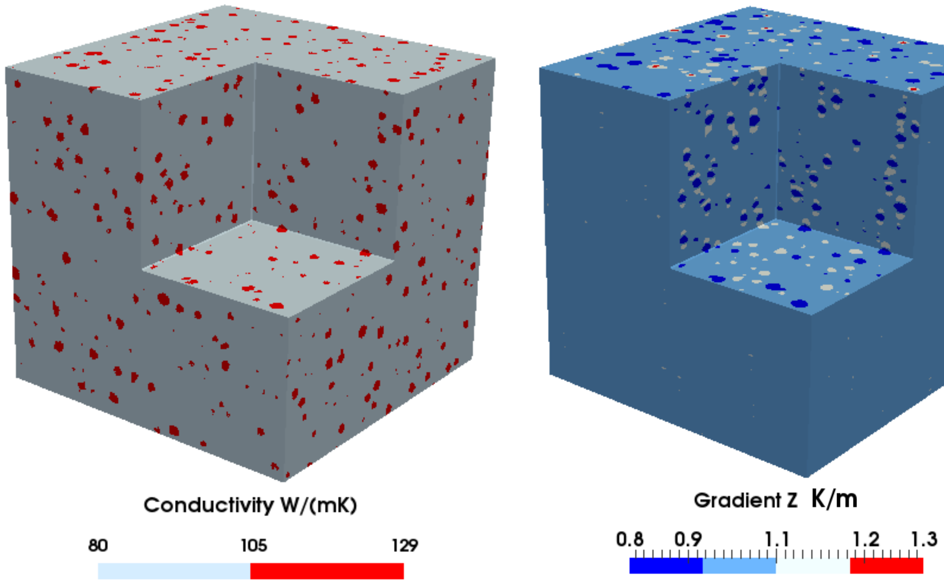

(a) Conductivity

(b) Temperature gradient

Figure 3.6: Conductivity of each component of cast iron and its temperature gradient field

Up to two significant digits, $\boldsymbol{A}$ can be described as:

$$\boldsymbol{A} = \left\{ \begin{array}{ccc} 82.43 & 0.00 & 0.00 \\ 0.00 & 82.42 & 0.00 \\ 0.00 & 0.00 & 82.43 \end{array} \right\} \mathrm{W} \cdot \mathrm{m}^{-1} \cdot \mathrm{K}^{-1}$$

which means that cast iron of this manufacturer is almost isotropic regardless of the random carbon distribution. Since the material is isotropic, one proposes to compute its effective property by classic Voigt-Reuss and Hashin-Shtrikman analytical homogenization method. Table 3.1 confirms the agreement between the analytical and the numerical homogenization for materials with such complex microstructure.

3.3.4 Laminated composite material image

Cast iron is almost isotropic, one may measure its conductivity experimentally. However, layered composite materials, which are also widely used in the industrial domain due to its good performance, can be significantly anisotropic. To carry out an experimental measurement, several external factors have to be observed, which is not simple and sometimes, not possible. Employing numerical simulations directly on tomographic images can be good alternative to know the composite properties.

The image used in this work is the image of a laminate composite material consisting of unidirectional E-glass fibers and a M9 epoxy matrix. It is a Glass Fiber Reinforced

Tableau 3.1: Effective thermal conductivity obtained by analytical homogenization methods

Bounds	$\mathbf{A}$ / W·m^{-1}·K^{-1})
VR$_-$	81.86
VR$_+$	82.70
HS$_-$	82.33
HS$_+$	82.42

Polymer (GFRP) manufactured by the Hexcel Company. Its mechanical properties have been studied by [LEC 15]. The details of this image can be found in the work of [LEC 15]. In this work, the heat transfer in this GFRP is studied to obtain its effective conductivity.

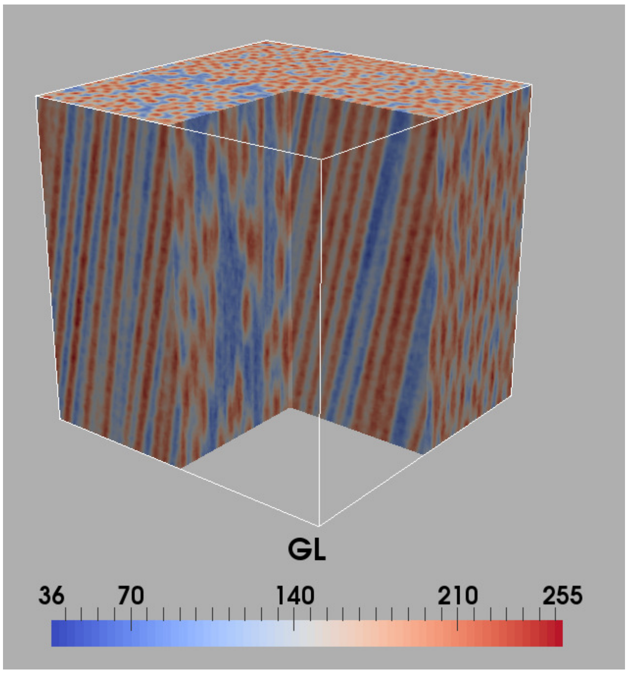

Figure 3.7: The ROI of the GFRP

The original image of this GFRP is an image consisting of 700 × 1300 × 1700 voxels, As mentioned in the work of [LEC 15], this material is designed with four layers, the fibers orientation is $+15°$,$-15°$,$-15°$ and $+15°$, respectively, for each layer. The idea is to take a cubic domain from the part which has the same fiber orientation. One takes $129 \times 129 \times 129$ voxels from the part with a fiber orientation of $-15°$, as the ROI (see Figure 3.7). As presented in 3.7, the interface between the E-glass fiber and M9 epoxy matrix is not extraordinarily sharp. It is difficult to distinguish between these two phases

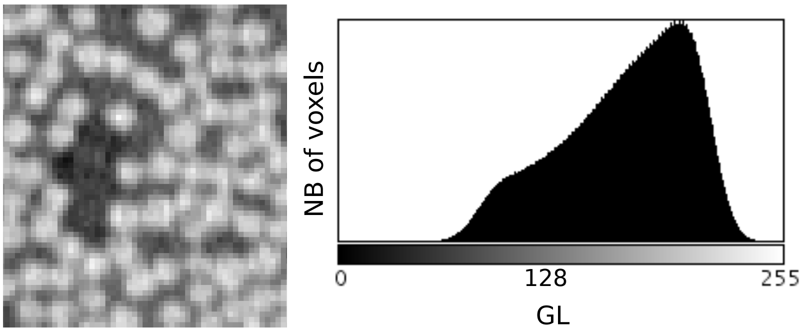

(a) Composite image (b) Histogram

Figure 3.8: Laminated composite image and its histogram

(matrix and fiber) as presented in Figure 3.8(a). From the histogram of this laminated composite in Figure 3.8(b), the interface is not obvious neither. Instead of applying two discontinuous phases, one proposes to apply a continuous conductivity between 0.150 $W{\cdot}m^{-1}{\cdot}\ K^{-1}$ (epoxy) and 1.30 $W{\cdot}m^{-1}{\cdot}\ K^{-1}$ (E-glass fiber). One chooses to smooth the image gray level before it is used to compute the local material property at each voxel. It can be described as:

$$\alpha = 0.575\left(\left(1 - e^{-\frac{|GL-160.5|}{20}}\right) sign\,(GL-160.5)+1\right)+0.15 \tag{3.6}$$

where GL is the original value of each voxel obtained by X–Ray tomography, which is an integer between 0 and 255. Figure 3.9 presents the material property variation in function of gray level. Figure 3.10 illustrates a good agreement can be found between the gravy level and the material property variations. Except for the problem of the allocation of the conductivity, another problem is that the diameter of fiber is too small to have enough voxels in it. Sub-sampling *i.e.* linear interpolation, is therefore applied to this ROI to have more voxels in each fiber. The FEM discretization error therefore needs to be analyzed, to obtain the number of voxels needed for each section. A simulation with $\nabla\theta_z = 1$ $W{\cdot}m^{-1}{\cdot}$ K^{-1}, $\nabla\theta_x = \nabla\theta_y = 0$ and $T = \nabla\theta_z z$ on $\partial\Omega$ is performed. One time sub-sampling (case I) and two times sub-sampling (case II) are applied to the ROI, respectively. Figure 3.11 illustrates the conductivity of each node in this ROI after one time sub-sampling. For the FMG Cycles, ν_0, ν_1, ν_2, n_{cy} are set to be 10, 2, 1 and 5, respectively.

The third column of the effective property tensor $\boldsymbol{A}_c$ is computed for each case.
For case I (7 levels *i.e.* 257^3 nodes):

$$\boldsymbol{A}_c^3 = \{-0.001559 \quad 0.025400 \quad 0.744922\}$$

For case II (8 levels *i.e.* 513^3 nodes):

$$\boldsymbol{A}_c^3 = \{-0.001607 \quad 0.026223 \quad 0.745158\}$$

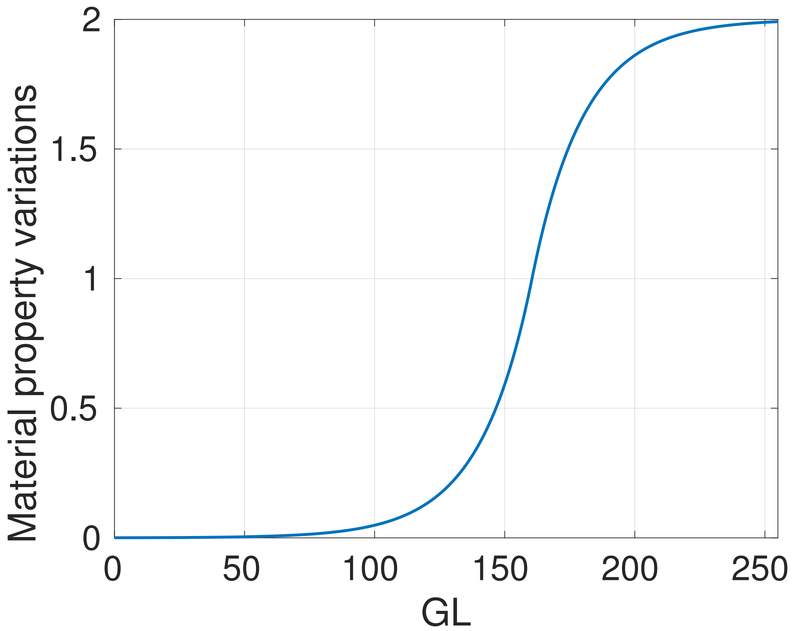

Figure 3.9: Function to generate material property from gray level. 0 represents the resin, 2 represents fibers.

It means that about up to three significant digits, the effective conductivity tensor is the same, or rather, one can take three significant digits for the $\boldsymbol{A}_c$ obtained by one time sub-sampling, which is sufficient for industrial applications. The temperature gradient is also computed, as presented in Figure 3.12.

Similar to the previous cast iron application, two other simulations with boundary conditions of equation (3.3) are performed. The effective conductivity of the ROI of the GFRP is:

$$\boldsymbol{A_c} = \left\{ \begin{array}{ccc} 0.625386 & 0.002162 & -0.001559 \\ 0.002162 & 0.628834 & 0.025400 \\ -0.001559 & 0.025400 & 0.744922 \end{array} \right\} W/(mK)$$

With up to three significant digits, it reads:

$$\boldsymbol{A_c} = \left\{ \begin{array}{ccc} 0.625 & 0.002 & -0.002 \\ 0.002 & 0.629 & 0.025 \\ -0.002 & 0.025 & 0.745 \end{array} \right\} W/(mK)$$

which confirms that GFRP is an orthotropic material.

The effective property tensor obtained above, is for the fibers with an orientation of -15°, for that of the $+15^\circ$ orientation, one can derive it directly.

The applications introduced above reveal that, the effective conductivity can be obtained by numerical simulations directly from an X-Ray tomographic image, without any

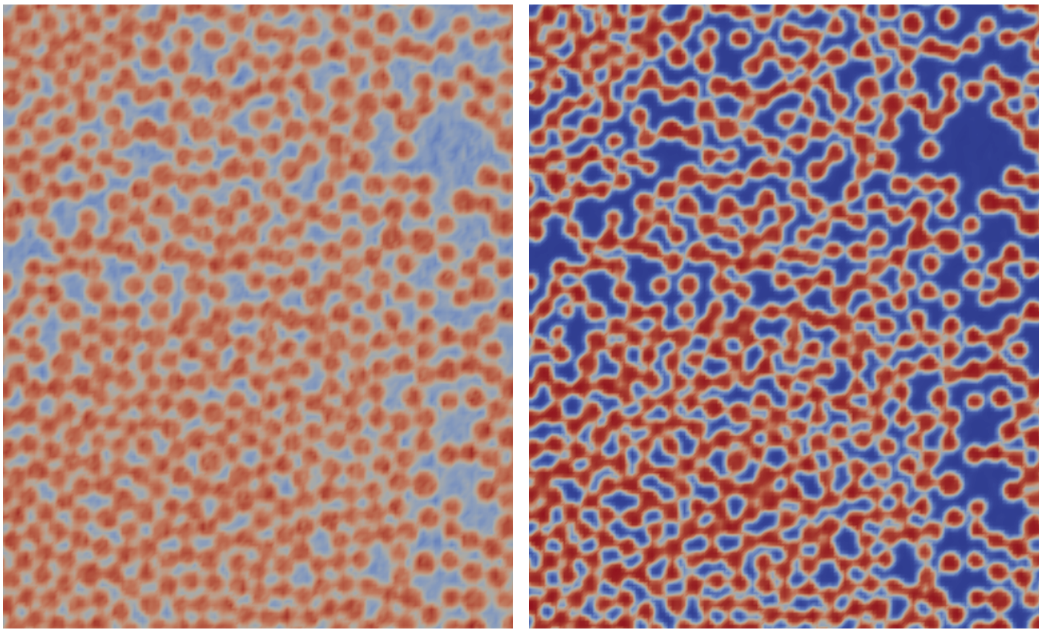

(a) Gray level (b) Material property variations

Figure 3.10: Laminated composite image and its property

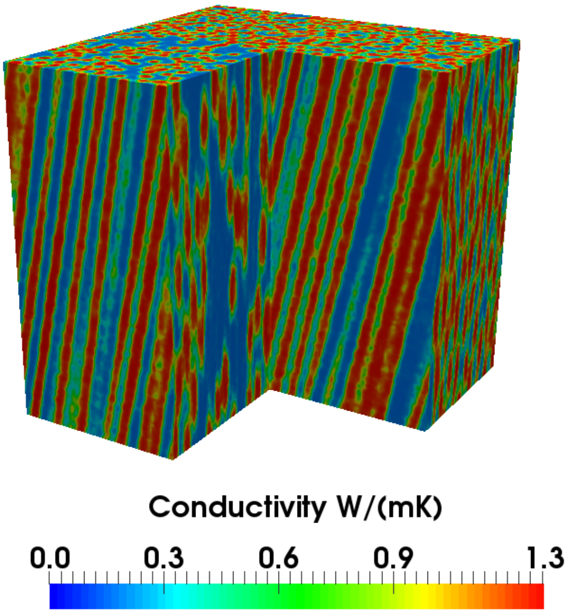

Figure 3.11: The conductivity of the fibers and the matrix

human intervention. The current tomographic images have 2048 × 2048 × 2048 voxels or more than 8 billion elements. The final application for this work it to carry out the

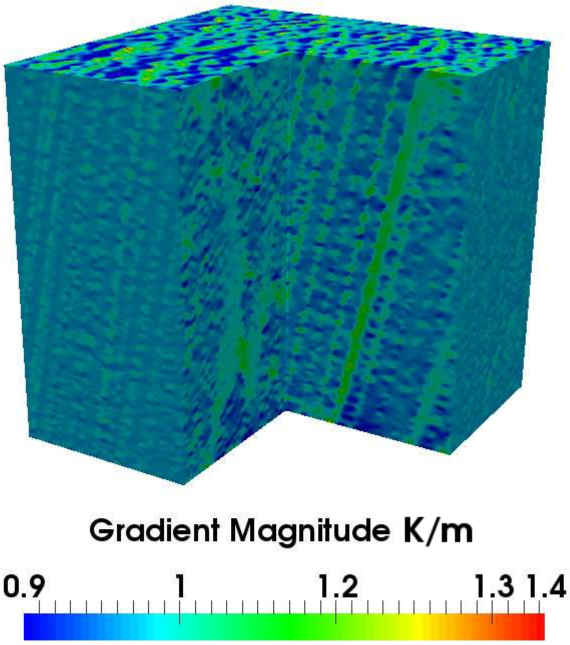

Figure 3.12: The temperature gradient in this composite material

numerical simulation with such a large image.

The image used in this case is the GFRP image of the previous application. One takes a part from the original image, the ROI consists of $513 \times 513 \times 513$ voxels. As presented in Figure 3.13, it consists of four layers with different E–glass fiber orientations. One employs a two times sub-sampling to obtain an image consisting of $2048 \times 2048 \times 2048$ elements. The smoothing process on the gray level is also applied and the material property has been assigned to each node as presented in Figure 3.13. The boundary conditions are applied as the following.

$$\begin{cases} T = 0K & \text{on } \Gamma_1 \\ T = 1K & \text{on } \Gamma_2 \\ \alpha \nabla T \cdot \vec{n} = 0 & \text{on the other surfaces} \end{cases}$$

For the FMG cycles in this simulation, 10 levels of grids are used, ν_0, ν_1, ν_2, n_{cy} are set to be 10, 2, 1 and 5, respectively. 768 cores (64 MPI, 12 OpenMP/MPI) are used simultaneously. The calculation time is about 3.16 hours.

Figure 3.14 illustrates the residual evolution with the number of V-Cycles on level 10. Regardless of the size of the problem, the convergence speed remains very good. To achieve a residual of 10^{-6}, only 5 V-Cycles on the finest level are required. It means that

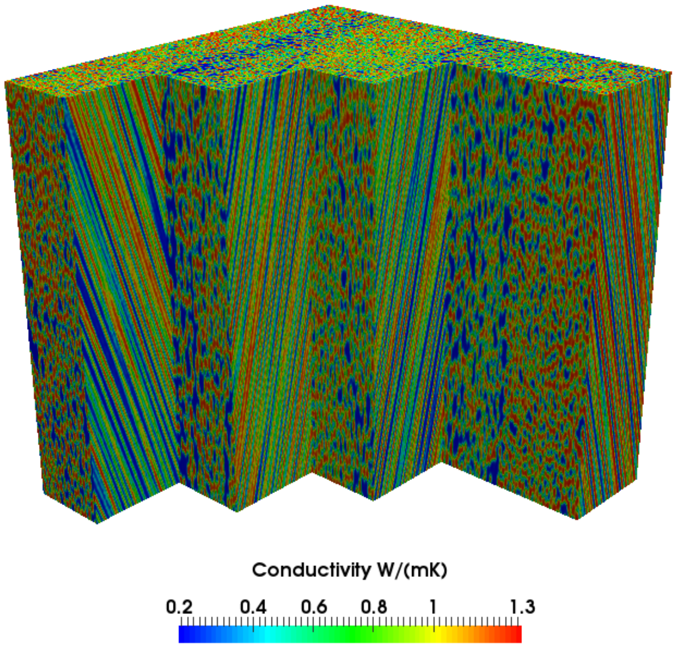

Figure 3.13: E–glass fiber orientation in each layer and conductivity at each elementary node

the number of relaxations on the finest level is only 15. It confirms the efficiency of the strategy used in this work.

The temperature gradient is presented in Figure 3.15. Figure 3.15 and 3.16 illustrate the correspondence between conductivity and temperature gradient. A smaller temperature gradient can be found in fibers where their thermal conductivity are larger.

3.4 Conclusion

The examples given in this chapter show the stability and the efficiency of the proposed strategy. They proved that numerical simulations at the microscopic scale permit one to deeply understand the material behavior. The CT simulation directly using the laminated structure implies the possibility to carry out numerical simulations with billions of DoF. The application of the spherical inclusion, of the cast iron image and of the composite image confirmed the stability of the proposed MF-FEM based MG method. The numerical homogenization coupled with the proposed strategy demonstrated the direct, efficient and automatic way to obtain the effective property of materials by using its tomography images.

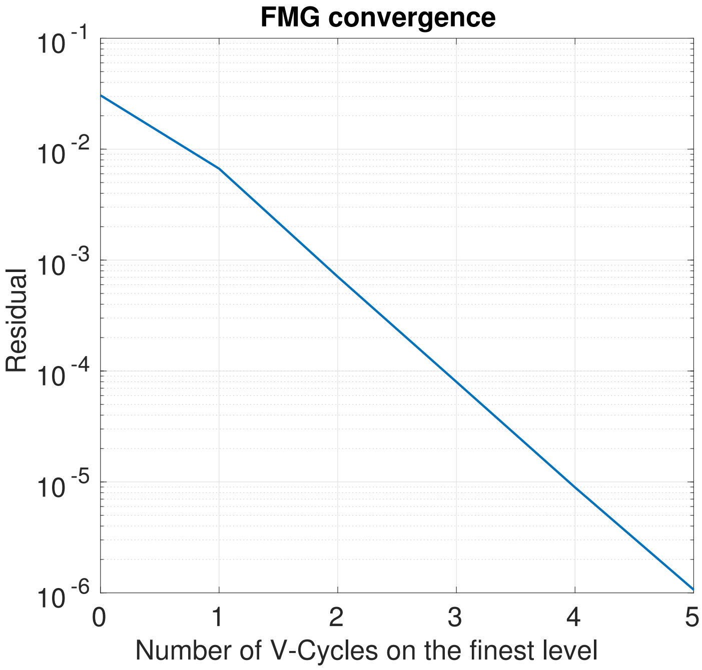

Figure 3.14: FMG convergence on the 2048^3-element problem

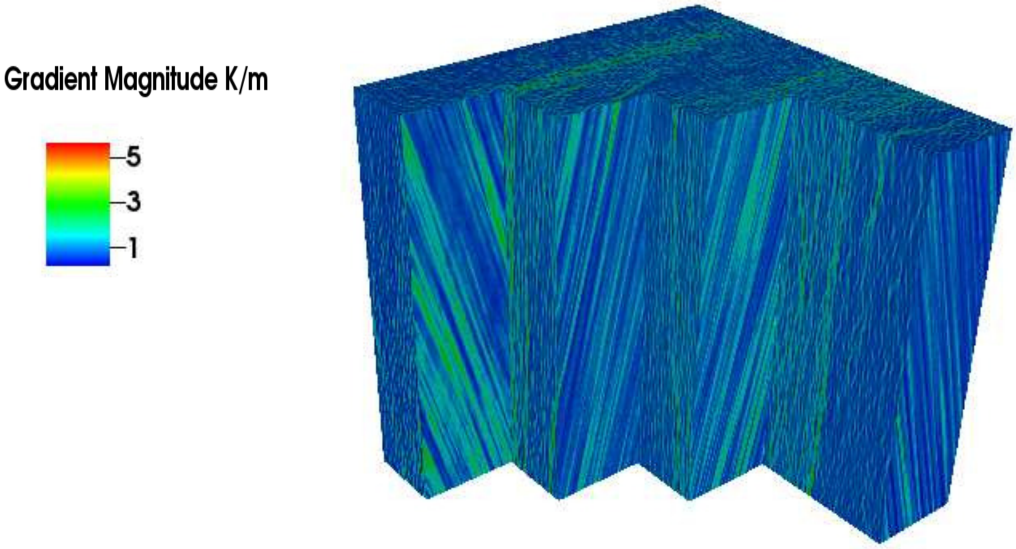

Figure 3.15: Temperature gradient of this four-layer composite material

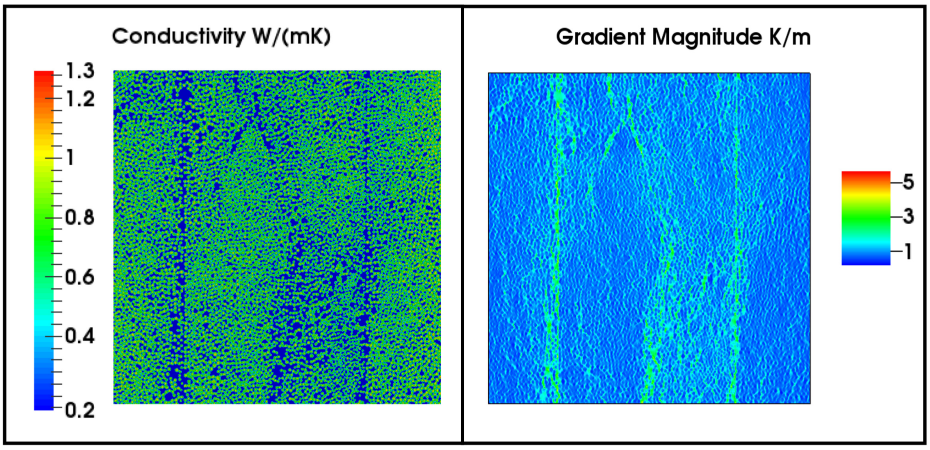

Figure 3.16: Conductivity (left) and temperature gradient (right) in the section of fibers and their surrounding matrix

Chapter 4

Mechanical problems

Contents

4.1 Introduction

In this chapter, the proposed massively parallel matrix free finite element based MultiGrid method is applied to the mechanical problems. Section 4.2 reviews the equations of mechanics and its numerical solutions by the MF-FEN iterative solver. The linear elastic case is also presented in the second part of this section. Section 4.3 introduces the process to apply the MG method on the mechanical problems with large material properties variations. Section 4.4 demonstrates the validation of the proposed method by comparing with the analytical homogenization method for a spherical inclusion case. The applications of the CT image of a laminated structure are presented after the validation in this section. The last part of this section studies the crack opening by using a CT image of the cast iron.

4.2 Problem statement and theory

To solve a mechanical problem, the equations of equilibrium are the basics. The fundamentals of solid mechanics equations and their numerical solutions are presented in this section.

4.2.1 Governing equations

Assuming a deformed domain Ω as presented in Figure 4.1, $\partial\Omega$ is its boundary and $\vec{n}$ is its exterior normal. $\boldsymbol{\sigma}$ denotes the second order stress tensor. $\vec{f}$ is the body force in Ω, which is due to gravity, magnetism, etc.. $\vec{a}$ is the acceleration, ρ is an abbreviation for density. The equilibrium equations can be described as:

$$\nabla \cdot \boldsymbol{\sigma} + \rho \vec{f} = \rho \vec{a} \tag{4.1}$$

For the sake of simplicity, the inertia effects are neglected in this paper. The equations of equilibrium can be simplified to:

$$\nabla \cdot \boldsymbol{\sigma} = \vec{0} \tag{4.2}$$

Another often used form can be written as follows:

$$\begin{cases} \frac{\partial \sigma_{xx}}{\partial x} + \frac{\partial \sigma_{xy}}{\partial y} + \frac{\partial \sigma_{xz}}{\partial z} & = 0 \\ \frac{\partial \sigma_{yx}}{\partial x} + \frac{\partial \sigma_{yy}}{\partial y} + \frac{\partial \sigma_{yz}}{\partial z} & = 0 \\ \frac{\partial \sigma_{zx}}{\partial x} + \frac{\partial \sigma_{zy}}{\partial y} + \frac{\partial \sigma_{zz}}{\partial z} & = 0 \end{cases}$$

Besides the equilibrium equations, the boundary conditions on $\partial\Omega$ are essential to solve a mechanical problem. Two kinds of boundary conditions are Dirichlet and Neumann boundary conditions. The Dirichlet boundary condition applied on $\partial\Omega_D$ is often presented as prescribed displacements, *e.g.* $\vec{u} = \vec{u_0}$ on Γ_1. The Neumann boundary condition applied on $\partial\Omega_N$ refers to the external force $\vec{f_{ex}}$, which can be described as:

$$\vec{f_{ex}} = \boldsymbol{\sigma} \cdot \vec{n}$$

e.g. applying $\vec{f_0}$ on Γ_2.

To solve equation (4.2), as stated in the fist chapter of this work, one has many choices *e.g.* the FDM, the FEM, the FFT, etc.. The aim of this work is to build an automatic solver using information directly from CT images. As presented in the above chapter the matrix free finite element method (MF-FEM) is suitable for the CT simulations. Instead of taking the heavy meshing step, each voxel in the CT image is supposed to be an elementary node. 8-node cuboid elements are therefore used to discretize Ω. With this strategy, the mesh generation step becomes automatic.

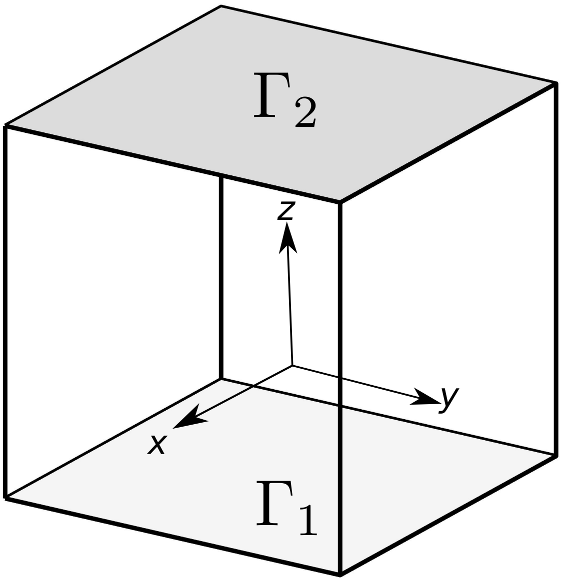

Figure 4.1: An elastic body Ω and its boundary

Multiplying equation (4.2) by a test function $\vec{u}^*$ and integrating on Ω, the weak form of equation (4.2) reads:

$$\int_\Omega \nabla \cdot \boldsymbol{\sigma} \vec{u}^* \, d\Omega = 0 \tag{4.3}$$

Applying the divergence theorem and integrating by parts, it reads:

$$\int_\Omega \boldsymbol{\sigma} \nabla \vec{u}^* \, d\Omega = \int_{\partial\Omega} \boldsymbol{\sigma} \cdot \vec{n} \vec{u}^* \, dS \tag{4.4}$$

which can be described as the equilibrium of internal forces $\vec{f_{in}}$ and external forces $\vec{f_{ex}}$:

$$\vec{f_{in}} = \vec{f_{ex}} \tag{4.5}$$

with

$$\begin{cases} \vec{f_{in}} & = \int_\Omega \boldsymbol{\sigma} \nabla \vec{u}^* \, d\Omega \\ \vec{f_{ex}} & = \int_{\partial\Omega} \boldsymbol{\sigma} \cdot \vec{n} \vec{u}^* \, dS \end{cases} \tag{4.6}$$

Applying finite element discretization, the displacements $\vec{u}$ can be described by:

$$\vec{u}^c \approx \sum_{i=1}^{N} \psi_i^c \hat{u}_i^c \tag{4.7}$$

where i denotes the node number, N is the number of nodes, index c represents the three directions with $c = \{1,2,3\}$. $\vec{\hat{u}}$ is the displacement at the elementary node i. $\hat{u}_i^c$ is thus the component c of the displacement at the node i. ψ is the shape function of a 8-node cubic element. The test function $\vec{u}^*$ reads:

$$\vec{u}^* = \psi_j^c$$

where j is the node number.

The internal force for node j and component c reads:

$$f_{in}^c = \sum_m \sum_e \sum_{g=1}^{8} w_g \sigma_{cm}(\vec{u}) \nabla_m \psi_j^c \tag{4.8}$$

with $m = \{1,2,3\}$. g is the Gauss integration point number, w_g is its weight. 8 Gauss integration points are used in each element. e is the element number. $\boldsymbol{\sigma}(\vec{\boldsymbol{u}})$ is the function implying the relationship between $\boldsymbol{\sigma}$ and $\vec{u}$. This function can be obtained by the constitutive law (The constitutive law of a linear elastic material is presented in the next part).

To solve equation (4.4), the typical FEM process is to compute the stiffness matrix and to use a direct or iterative solver. However, a typical FEM process is almost impossible for a large scale CT image simulation because of memory space limitations, *e.g.* for a problem with more than 18 billion DoF. In this chapter, the MF-FEM iterative solver is developed for CT simulations on mechanical problems.

The principle is to compute the unknowns node by node without using the entire stiffness matrix. It can be described by equation (4.9).

$$\vec{u}^{ite+1} = \vec{u}^{ite} + \omega \boldsymbol{S} (\vec{f}_{ex} - \vec{f}_{in}) \tag{4.9}$$

where $\vec{u}^{ite+1}$ and $\vec{u}^{ite}$ are displacements of one node in the current iteration and the previous iteration. ω is the relaxation coefficient, for $0 < \omega < 1$, it refers to damped Jacobi, *i.e.* under-relaxation, which is used in this part. $\boldsymbol{S}$ is the compliance of the diagonal value of the stiffness matrix at this node. It reads:

$$\boldsymbol{S} = \begin{bmatrix} \frac{1}{K_u} & 0 & 0 \\ 0 & \frac{1}{K_v} & 0 \\ 0 & 0 & \frac{1}{K_w} \end{bmatrix} \tag{4.10}$$

where K_u, K_v and K_w are the diagonal values of the stiffness matrix at each DoF.

4.2.2 The linear elasticity

It this work, the above strategy is applied to a linear elastic problem.

For a linear elastic problem, the constitutive equation reads:

$$\boldsymbol{\sigma} = \boldsymbol{C} \boldsymbol{\varepsilon} \tag{4.11}$$

where ε is the second order strain tensor, $\boldsymbol{C}$ is a symmetric forth order tensor. For isotropic materials, only two elastic constants are independent. The often used constants are Young's modulus E and Poisson's ratio υ. $\boldsymbol{C}$ for isotropic materials can be described as:

$$\boldsymbol{C} = \frac{E}{(1+\nu)(1-2\nu)} \begin{pmatrix} 1-\nu & \nu & \nu & 0 & 0 & 0 \\ \nu & 1-\nu & \nu & 0 & 0 & 0 \\ \nu & \nu & 1-\nu & 0 & 0 & 0 \\ 0 & 0 & 0 & \frac{1-2\nu}{2} & 0 & 0 \\ 0 & 0 & 0 & 0 & \frac{1-2\nu}{2} & 0 \\ 0 & 0 & 0 & 0 & 0 & \frac{1-2\nu}{2} \end{pmatrix} \tag{4.12}$$

In this work, materials are considered to be locally isotropic, *i.e.* on each elementary node. The constitutive law can implied by the bulk modulus and the shear modulus:

$$\boldsymbol{\sigma} = Ktr(\varepsilon)\boldsymbol{I} + 2G\left(\varepsilon - \frac{1}{3}tr(\varepsilon)\right) \tag{4.13}$$

K and G refer to the bulk modulus and the shear modulus, respectively. $\boldsymbol{I}$ is the unit tensor. Using with the Young's modulus E and the Poisson ratio υ, K and G read:

$$K = \frac{E}{3(1-2\upsilon)}, \qquad G = \frac{E}{2(1+\upsilon)}$$

The strain ε can be described by the displacement $\vec{u}$:

$$\varepsilon = \frac{1}{2}\left(\nabla\vec{u} + \nabla^T\vec{u}\right) \tag{4.14}$$

Since $\vec{u}$ is symmetrical, one has:

$$tr(\varepsilon) = tr\left(\frac{1}{2}\left(\nabla\vec{u} + \nabla^T\vec{u}\right)\right) = tr(\nabla\vec{u})$$

Combining equation (4.13) and (4.14), equation (4.13) reads:

$$\boldsymbol{\sigma} = \left(K - \frac{2G}{3}\right)tr(\vec{u})\boldsymbol{I} + G(\nabla\vec{u} + \nabla^T\vec{u}) \tag{4.15}$$

Applying the finite element discretization with equation (4.7), the stress reads:

$$\sigma_{cm}(\vec{u}) = \sum_i \left[\left(K - \frac{2G}{3}\right)\left(\sum_k \nabla_k \psi_i^k \hat{u}_i^k\right)\delta_{cm} + G\left(\nabla_m \psi_i^c \hat{u}_i^c + \nabla_c \psi_i^m \hat{u}_i^m\right)\right] \tag{4.16}$$

where $k = \{1, 2.3\}$. δ_{cm} is the Kronecker delta. It reads:

$$\delta_{cm} = \begin{cases} 1 & c = m \\ 0 & c \neq m \end{cases}$$

Combining equation (4.8) and (4.16), one obtains the component c of the internal force on node j:

$$\begin{aligned} f_{in}^{c} = &\sum_{e}\sum_{g=1}^{8}\sum_{i} w_g \left\{ \left(K^g - \frac{2G^g}{3}\right)\left(\sum_{k}\nabla_k \psi_i^k \hat{u}_i^k\right)\nabla_c \psi_j^c \right. \\ &\left. + \sum_{m}\left[G^g\left(\nabla_m \psi_i^c \hat{u}_i^c + \nabla_c \psi_i^m \hat{u}_i^m\right)\nabla_m \psi_j^c\right]\right\} \end{aligned} \tag{4.17}$$

K^g and G^g are the material property at a Gauss point. As mentioned before, the material property is assigned to each node from voxel information. An interpolation is used to obtain the material property at each Gauss point. It reads:

$$K^g = \sum_{i=1}^{8}\psi_i K_i \quad G^g = \sum_{i=1}^{8}\psi_i G_i.$$

K_u in the first term of $\boldsymbol{S}$ in equation (4.10) reads:

$$K_u = \sum_{e}\sum_{g} w_g \left[\left(K^g - \frac{2G^g}{3}\right)\nabla_c \psi_j^c \nabla_c \psi_j^c + \sum_{m} G^g \nabla_m \psi_j^c \nabla_m \psi_j^c + G^g \nabla_c \psi_j^c \nabla_c \psi_j^c\right]$$

where $c = 1$ represents the first term. Equation (4.9) can thus be solved node by node.

4.3 The MultiGrid method for mechanical problems

As presented in the work of the thermal conduction problems, using only the MF-FEM Jacobi solver, the convergence rate can be very slow after several iterations. The same strategy is applied to the mechanical problem to improve convergence. The MG method is therefore applied to the iterative solver to improve convergence.

As mentioned in the thermal conduction application, the principle of MG is that relaxations on the fine grid can eliminate high frequency errors, and the low frequency errors can be eliminated by relaxing on the coarse grid. The first step of MG is therefore to construct several levels. In this work, the grid size on level l is two times larger than that on level $l+1$, *e.g*, for a 128^3-grid problem with 3 level, the number of points on each level is: 128^3 on level 3, 64^3 on level 2 and 32^3 on level 1.

Once the different grids are constructed, as presented in the above chapter, three important operators are needed to employ a MG scheme: the coarse grid operator, the restriction operator $\boldsymbol{R}$ and the prolongation operator $\boldsymbol{P}$. As presented in for the thermal conduction, the standard MG scheme can not deal efficiently with problems with large variations of the material properties. Special intergrid operators are generated in the same way for the mechanical problems.

The process to obtain the $\vec{F_{in}}$ and the $\boldsymbol{S}$ indicates that for a representative coarse grid operator, one needs the material property and the shape function on the coarse grid. The shape function of an element on each coarse grid is simple to obtain with the finite element theorem. For the material property on the coarse grid, the standard method is to compute the arithmetic average, *i.e* Voigt approximation, of the material property on the coarse grid. However, for heterogeneous materials with large property variations, a simple average can not represent the material on the fine grid. In this chapter, we propose to apply the homogenization method proposed for the thermal problems, which applied the homogenization method on MG algorithms to obtain the coarse grid operator.

The principle is to compute first the Voigt and Reuss approximations of K and G on all the coarse grid recursively as follow:

$$\begin{cases} \text{Voigt: } K^{HV} = \frac{\sum_1^{N_h} K^h}{N_h}, & G^{HV} = \frac{\sum_1^{N_h} G^h}{N_h} \\ \text{Reuss: } K^{HR} = \frac{N_h}{\sum_1^{N_h} \frac{1}{K^h}}, & G^{HR} = \frac{N_h}{\sum_1^{N_h} \frac{1}{G^h}} \end{cases}$$

where K^{HV}, G^{HV}, K^{HR} and G^{HR} are Voigt and Reuss approximations of the bulk modulus and shear modulus on the coarse grid, N_h is the number of nodes on level l, which has the same volume as one element on level $l-1$.

According to the work on homogenization techniques, the effective material property lies between the Voigt and Reuss approximations, which is called Voigt-Reuss (VR) bounds. VR bounds are not the most accurate bounds, but one can compute them recursively from the finest level. The effective material property on the coarse grid can be obtained by the following equation:

$$\begin{cases} K^H & = \frac{\left(\frac{K^{HV}+K^{HR}}{2} + \sqrt{K^{HV}K^{HR}}\right)}{2} \\ G^H & = \frac{\left(\frac{G^{HV}+G^{HR}}{2} + \sqrt{G^{HV}G^{HR}}\right)}{2} \end{cases} \tag{4.18}$$

which means the effective K^H and G^H on the coarse grid is the mean of the arithmetic and geometric average of the VR bounds on this level. According to the comparison of different homogenization methods in [LIU 19], the proposed homogenization scheme is robust and efficient.

With the correct material property and correct shape function on the coarse grid, one can now define the coarse grid operator. For the restriction operator $\boldsymbol{R}$ and the prolongation operator $\boldsymbol{P}$, the process of prolongation of corrections can be described with one element on the coarse grid $l-1$ and its eight elements on the fine grid l as presented in Figure 4.2. The objective is to bring the correction, *i.e* displacement corrections $\vec{e}$, from level $l-1$ to level l. The displacement correction of level $l-1$ at black points is known. Instead of computing a simple average, one proposes to account for the material property at each node. The bulk modulus K is used.

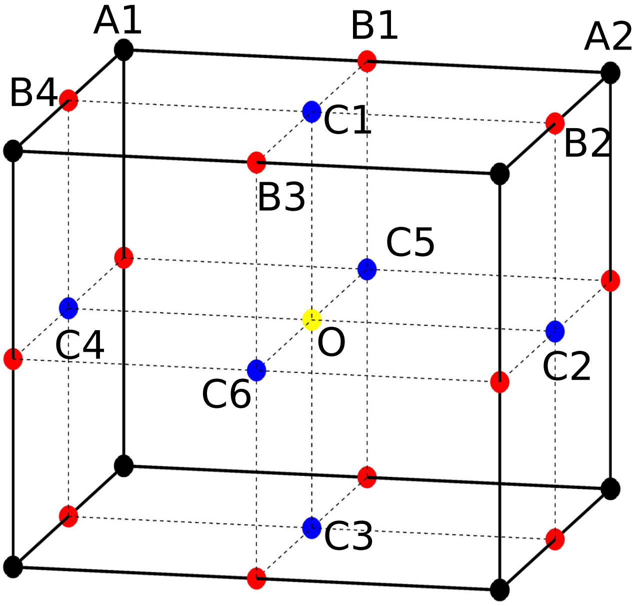

Figure 4.2: Prolongation scheme

For the black points on level l, one performs an injection from level $l-1$ to l, *e.g.* point $A1$:

$$\vec{e^{l}_{A1}} = \vec{e^{l-1}_{A1}}.$$

For the red points, one computes them from the $\vec{e}$ at black point of level l, *e.g.* point $B1$:

$$\vec{e^{l}_{B1}} = \frac{K_{A1}\vec{e^{l}_{A1}} + K_{A2}\vec{e^{l}_{A2}}}{K_{A1} + K_{A2}}.$$

For the blue points, one computes them from the $\vec{e}$ at red points on level l, *e.g.* point $C1$:

$$\vec{e^{l}_{C1}} = \frac{K_{B1}\vec{e^{l}_{B1}} + K_{B2}\vec{e^{l}_{B2}} + K_{B3}\vec{e^{l}_{B3}} + K_{B4}\vec{e^{l}_{B4}}}{K_{B1} + K_{B2} + K_{B3} + K_{B4}}.$$

For the yellow points, one computes them from the $\vec{e}$ at blue points on level l, *e.g.* point O:

$$\vec{e^{l}_{O}} = \frac{K_{C1}\vec{e^{l}_{C1}} + K_{C2}\vec{e^{l}_{C2}} + K_{C3}\vec{e^{l}_{C3}} + K_{C4}\vec{e^{l}_{C4}} + K_{C5}\vec{e^{l}_{C5}} + K_{C6}\vec{e^{l}_{C6}}}{K_{C1} + K_{C2} + K_{C3} + K_{C4} + K_{C5} + K_{C6}}.$$

For the restriction process, one can use $\boldsymbol{R} = \boldsymbol{P}^T$ to obtain the restriction operator.

In this part, FMG cycle is performed to have a good initial solution on the finest grid. The process of the FMG cycle is the same as for the thermal conduction problem.

With the above strategy, the construction of a MF-FEM iterative solver with homogenized MG algorithms for the mechanical problems is finished. One can start performing numerical simulations. However, for a large image, *e.g.* with more than 18 billion DOF, the computational time is too long using a standard computer. Hybrid MPI+OpenMP programming is therefore applied to achieve good parallel computational performance as the strategy propose for the thermal applications.

4.4 Validation and applications

In this section, the proposed strategy is validated using a spherical inclusion case. The effective elastic modulus of a spherical inclusion is computed both by the analytical homogenization method and the computational homogenization method with the proposed strategy. A comparison of the effective modulus obtained by different methods is then performed. Two industrial material applications are presented following the validation subsection.

4.4.1 Validation

To validate the proposed strategy, the typical spherical inclusion case is used. The cubic domain Ω is filled with a spherical inhomogeneity and a homogeneous matrix as presented in figure 4.3. The sphere radius is a quarter of the cube size L. The elastic modulus of the sphere is $\boldsymbol{C}_s$, and $\boldsymbol{C}_m$ denotes the elastic modulus of matrix. The ratio between these two materials is $r_e = \frac{E_m}{E_s}$, where E_m and E_s are the Young modulus of matrix and inclusion *e.g.* Figure 4.3 presents the case of $E_m = 500$ GPa and $E_s = 1$ GPa. The Poisson ratio equals to 0.3 for both materials. The objective is to compute the effective modulus $\boldsymbol{C}$ of the domain Ω for different r_e. For the sake of simplicity, E_s equals to 1 GPa.

One of the best-know methods is the Mori-Tanaka (MT) homogenization method, see [MOR 73] and [BEN 87] for details. The effective modulus obtained by MT is:

$$\boldsymbol{C}_{MT} = \boldsymbol{C}_m + V_s(\boldsymbol{C}_s - \boldsymbol{C}_m)\boldsymbol{A}$$

where

$$\boldsymbol{A} = \boldsymbol{T}[(V_m - V_s)\boldsymbol{I} + V_s\boldsymbol{T}]^{-1}$$

with

$$\boldsymbol{T} = [\boldsymbol{I} + \boldsymbol{S}_s\boldsymbol{C}_m^{-1}(\boldsymbol{C}_s - \boldsymbol{C}_m)]^{-1}$$

where $\boldsymbol{I}$ is the unit tensor, $\boldsymbol{S}_s$ is the Eshelby tensor (see [GU 16] for details and Appendix 4.5 for its formulation), V_s denotes the volume fraction of the sphere part, $\boldsymbol{C}_{MT}$ is the effective elastic modulus obtained by MT homogenization.

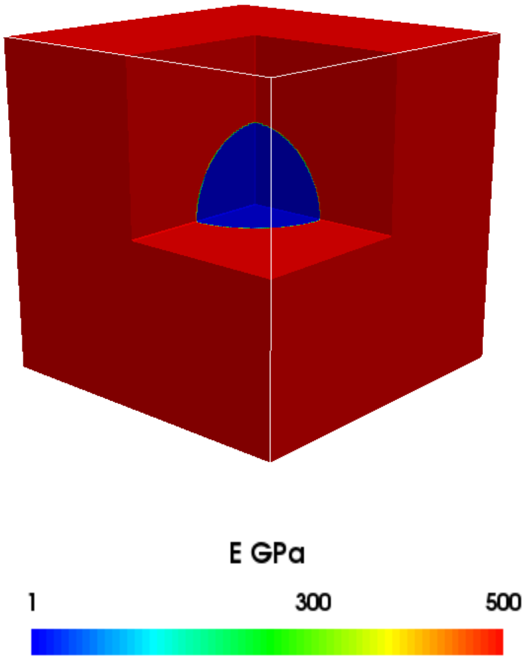

Figure 4.3: Young modulus of inclusion and matrix

For the computational homogenization with the proposed MG strategy, the homogeneous displacement boundary condition is applied to obtain the effective modulus $\boldsymbol{C}_{MG}$. Domain Ω is discretized by 256×256×256 elements. The under-relaxation coefficient equals to 0.5 for the jacobi solver. The coarsest grid has 4×4×4 elements, thus there are 7 levels. The FMG cycles use $n_{cy} = 6$, $\nu_0 = 50$, $\nu_1 = 4$ and $\nu_2 = 2$. The comparison between $\boldsymbol{C}_{MT}$ and $\boldsymbol{C}_{MG}$ is qualified using the following equation:

$$e_{MT-MG} = \frac{1}{n_t}\sqrt{\sum_{i=1}^{n_t}\left(\frac{C_i^{MT} - C_i^{MG}}{C_i^{MT}}\right)^2}$$

where C_i^{MT} is each term of $\boldsymbol{C}_{MT}$. C_i^{MG} is each term of $\boldsymbol{C}_{MG}$. n_t is the number of components in elastic modulus, which equals to 36.

The elastic modulus for $r_e = 10$ obtained by the MT and the MG is presented as the following:

$$C_{MT} = \begin{pmatrix} 11.933 & 4.997 & 4.997 & 0 & 0 & 0 \\ 4.997 & 11.933 & 4.997 & 0 & 0 & 0 \\ 4.997 & 4.997 & 11.933 & 0 & 0 & 0 \\ 0 & 0 & 0 & 3.563 & 0 & 0 \\ 0 & 0 & 0 & 0 & 3.563 & 0 \\ 0 & 0 & 0 & 0 & 0 & 3.563 \end{pmatrix} \text{GPa}$$

$$C_{MG} = \begin{pmatrix} 11.986 & 4.991 & 4.991 & 0 & 0 & 0 \\ 4.991 & 11.986 & 4.991 & 0 & 0 & 0 \\ 4.991 & 4.991 & 11.986 & 0 & 0 & 0 \\ 0 & 0 & 0 & 3.488 & 0 & 0 \\ 0 & 0 & 0 & 0 & 3.488 & 0 \\ 0 & 0 & 0 & 0 & 0 & 3.488 \end{pmatrix} \text{GPa}$$

From these two elastic modulus, we find that the effective material is isotropic, which confirms to this case. Table 4.1 presents the first item of the effective modulus obtained by the MT and the MG method for different r_e. e_{MT-MG} is also presented in Table 4.1. From this table, a good agreement can be found between the MT and the MG. There is a small difference (less than 0.5%) between these two methods. The proposed method is therefore validated.

Tableau 4.1: C_{1111} obtained by MT and MG

r_e	C^{MT}_{1111}/GPa	C^{MG}_{1111}/GPa	e_{MT-MG}
1	1.346	1.346	0
10	11.934	11.986	0.31%
50	58.220	58.557	0.40%
100	116.037	116.730	0.42%
200	231.6670	233.068	0.43%
500	578.549	582.073	0.43%

The strain field of this spherical case with $r_e = 500$ is illustrated in Figure 4.4. It is the field of strain XX obtained by the prescribed displacement as indicated in equation 4.19.

$$\vec{u} = \{x, 0, 0\} \quad \text{on all the surfaces} \tag{4.19}$$

where x is the coordinate of the X direction. Some strain raisers are found at the interface of matrix and inhomogeneity. The strain inside the sphere is smaller than in the matrix which is typical for soft inclusions.

The efficiency of the proposed strategy is also analyzed for this mechanical problem. The principle is to perform the numerical simulation for $r_e = 10$ with both the FMG scheme and the single level Jacobi iterative solver. Figure 4.4.1 implies that with 2000 relaxations, the single level Jacobi iterative solver still can not achieve the initial residual of the FMG scheme. The FMG achieves a residual of 10^{-5} with 36 relaxations. The FEM convergence slows down after only few relaxations. However, the FMG scheme remains its good convergence. The red line in Figure 4.5(b) demonstrates the residual at the finest level after each V–Cycle of the FMG scheme.

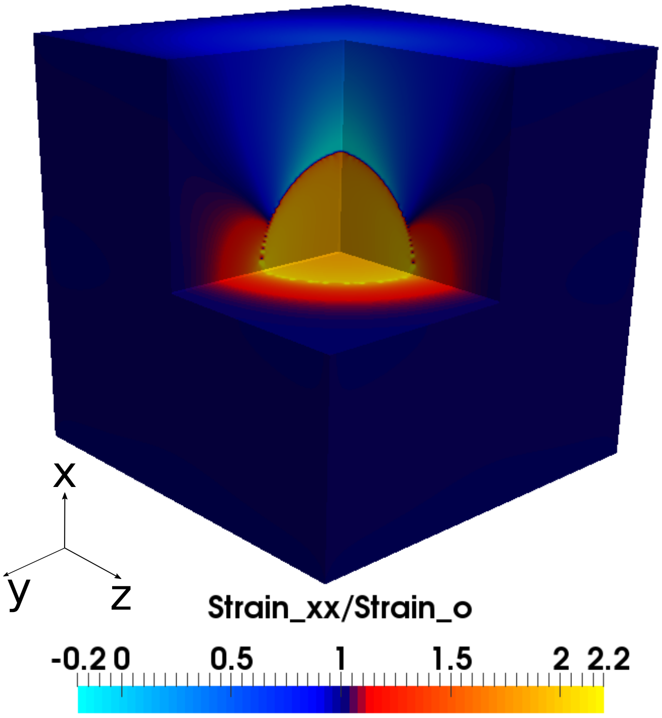

Figure 4.4: Strain field of spherical inclusion case. The white box is the initial shape of Ω

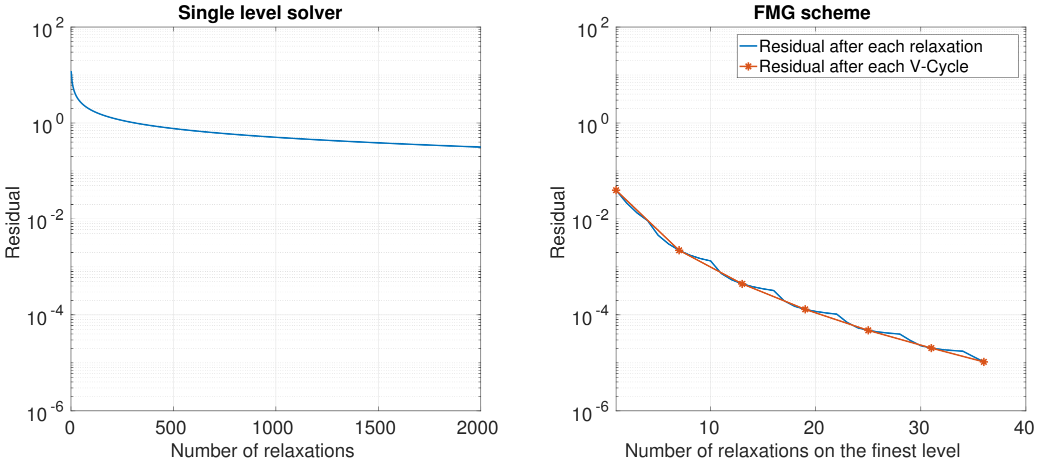

(a) Single level

(b) FMG scheme

Figure 4.5: Convergence of the Jacobi solver (a) and FMG scheme (b) on a 256^3 nodes problem

4.4.2 Laminated material simulations

In this subsection, a simulation on a problem with more than 18 billion DoF is presented. The numerical result is then compared to the experimental result obtained by the digital image correlation (DIC).

The CT image of a laminated material is used in this case. This CT image has 700×1300×1700 voxels with 4.5 µm/pixel. This laminated structure consists of four layers with a fiber orientation of 15°, -15°, -15° and 15°, respectively. The fiber is the E-glass fiber with a Young's modulus of 80.0 GPa. The matrix is s M9 epoxy with a Young's modulus of 3.2 GPa. The Poisson ratio of these two materials equals to 0.22. Figure 4.6 illustrates a section view of an interface of layers, one can observe two different fiber orientations crossing, and the fiber distributions are not uniform. All these defects, which can only be seen by CT, have an impact on the material mechanical behavior under certain loading. More information about this image and this material can be found in [LEC 15].

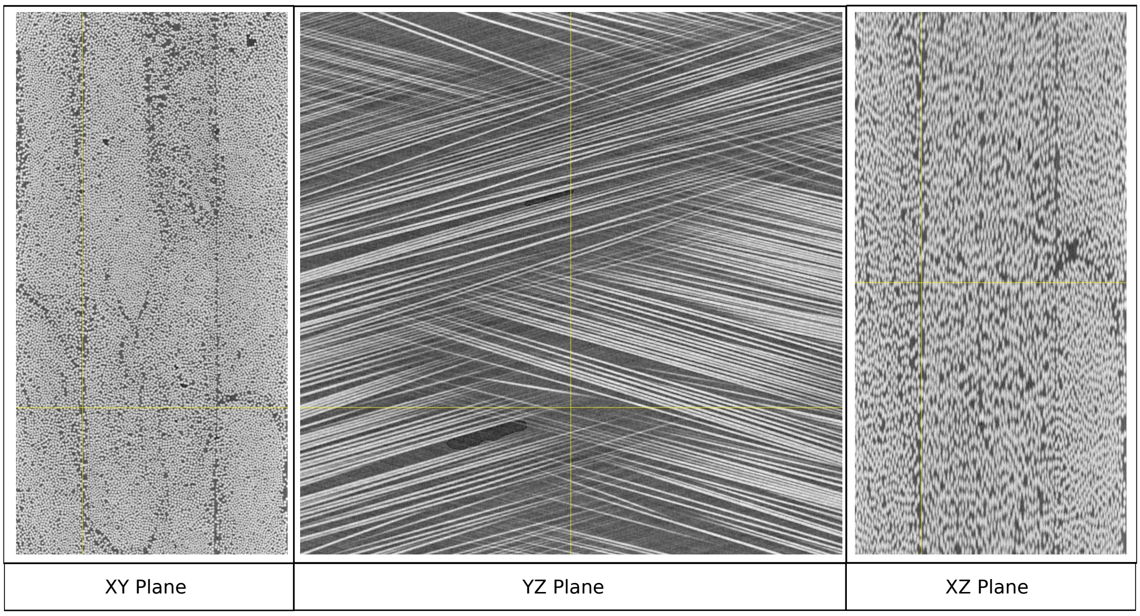

Figure 4.6: Sections of material

The main subject of this subsection is to analyze free edge effects in the laminated structure by numerical simulation. A qualitative comparison between the numerical results and the experimental results is also presented. The free edge effect was firstly presented by [PIP 94], who found the strain concentrations around free edges and the ply interface. [LEC 09] illustrates the free edge effect by the DIC experimental method of an unidirectional carbon fiber reinforced plastic laminated structure. For more information about the free edge effect, see [PIP 94]. In this paper, instead of carrying out DIC experiments, the CT image of the laminated material is used directly to employ numerical simulations and understand the free edge effect.

To carry out numerical simulations, one proposes to take a part of this image which refers to the region of interest (ROI). The ROI is constituted of 577×1153×1153 voxels as presented in Figure 4.7. To have more voxels in the fiber section, one performs a subsampling, *i.e.* linear interpolation, on this ROI. Figure 4.8 shows that we have about ten pixels per fiber diameter. The final input image, *i.e.* domain Ω, has 1153×2305×2305 voxels which means we have more than 6 billion elements, *i.e.* 18 billion DoF. The coordinates of the center of Ω are (0,0,0) with a size of L×2L×2L.

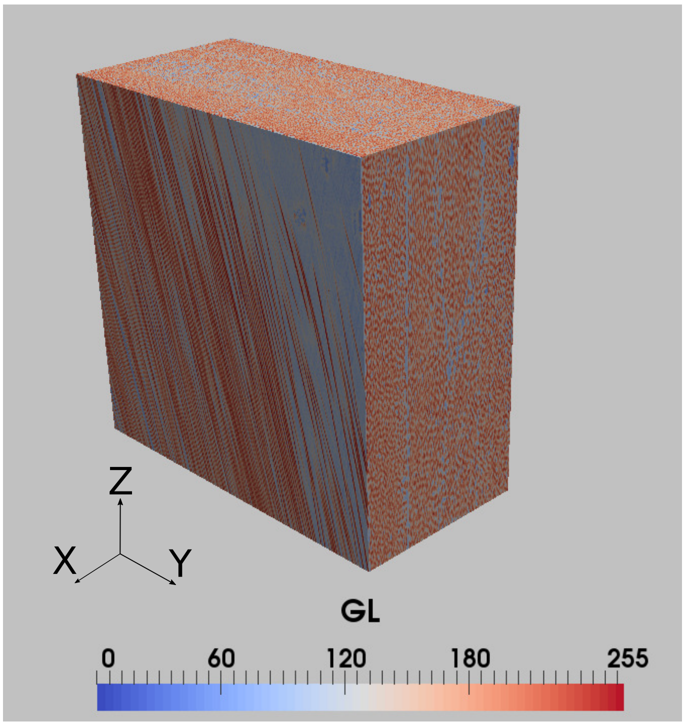

Figure 4.7: The gray level (GL) of the ROI opened in Paraview with colors

The boundary conditions are given by the following equations:

$$\begin{cases} \vec{u} = \{0, 0, -0.01L\}, & \text{on } z = -L \\ \vec{u} = \{0, 0, 0.01L\}, & \text{on } z = L \end{cases} \tag{4.20}$$

where u_z is the displacement in Z direction.

There are 1153×2305×2305 elementary nodes on the finest level and 9×18×18 elements on the coarsest level with a total of 8 levels. The under-relaxation coefficient equals to 0.5 for the Jacobi solver. The parameters of the FMG cycles are: $n_{cy} = 9$, $\nu_0 = 500$, $\nu_1 = 4$ and $\nu_2 = 2$.

Figure 4.9 illustrates the Young modulus and the shear strain XZ on surface $y = -L$. This figure demonstrates that the shear strain field mimics the Young modulus distribution. Shear strain concentrations are found on the two interfaces. This is the so called free

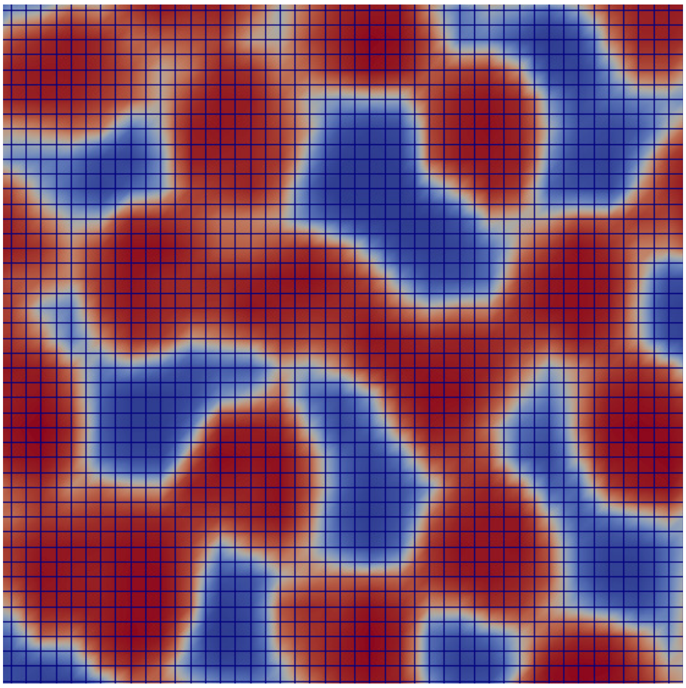

Figure 4.8: Pixels in fiber section; red is fiber, blue is matrix

edge effect in laminated materials. In the area with few fibers with too much matrix, they also aches strain concentrations which can lead to preventive damage in industrial applications. The same phenomena are found by the DIC experimental method in [LEC 09]. The material used in [LEC 09] is a carbon fiber reinforced plastic laminated structure which is similar to the material used in this work. A good correlation between the numerical and the experimental results is found.

Figure 4.10 reveals the displacement in the Z direction on the two opposite surfaces $y = -L$ and $y = L$. Equally, the free edge effect can be found on the interfaces, which leads to large displacement variations on the interfaces. This displacement variation can also be found in [LEC 09], the displacement curves illustrated in Figure 4.11, have the same tendency both for the numerical results and the DIC results. Another phenomenon that we can observe is that the displacement variations on $y = -L$ is almost anti-symmetric to $y = L$. This is because the fiber orientations on these two opposite surfaces are anti-symmetric. The Z displacements along the X axis in the center of these two surfaces are illustrated in Figure 4.11 where a clear anti-symmetry can be found.

4.4.3 Cast iron applications

Cast iron is a widely used industrial material. Its artifacts date to the fifth century BC according to an analysis of the microstructures of the artifact according to [WAG 93]. However, its mechanical behavior is not known as long as its history. Nowadays, re-

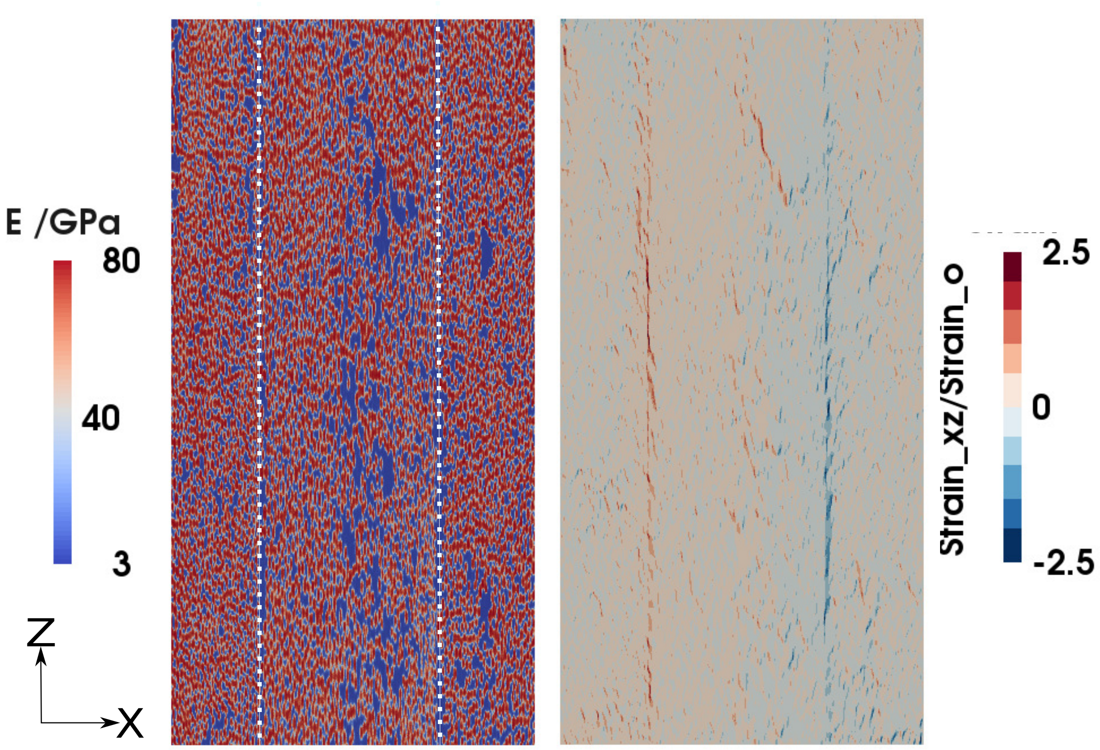

Figure 4.9: Young modulus and strain on the surface $y = -L$; the white dashed lines are the interfaces of layers. $Strain_o$ is the macroscopic strain, which is 1%.

searchers are still not able to understand its complete mechanical behavior due to its complex structure at the microscopical scale, *e.g.* carbon nodule distributions. Because of its wide use, many researchers investigated its mechanical and thermal properties. [ELL 88] and [ANG 60] are early books which analyzed cast iron in detail. [RAN 10] analyzed the fatigue crack problem by using the CT image of cast iron both numerically and experimentally. In this work, we perform the proposed strategy on a nodular graphite cast iron CT image.

The image used in this paper is the image obtained by [RAN 10] using X–Ray tomography. This image consists of 340×340×512 voxels with a 5.06 µm/pixel size. For more information about this CT image, please refer to [RAN 10]. A ROI with 257×257×257 voxels is taken from this CT image. As illustrated in Figure 4.12, many carbon nodules with a random distribution, can be found at the microscopic scale of the CT image.

The objective is to perform the linear elastic simulation on the ROI, with a prescribed rectangular crack to see how carbon nodules affect the crack opening. Assuming Ω is the ROI. The center of the Ω is the origin of axis. The size of Ω is L. 256^3 8-node cubic elements are used to discretize Ω. The rectangular crack is presented in Figure 4.13. The width of the crack is the size of the cube L. Its length is $\frac{L}{3}$. The crack is constructed by setting material property as 0 one three layers of nodes in Z direction. The prescribed

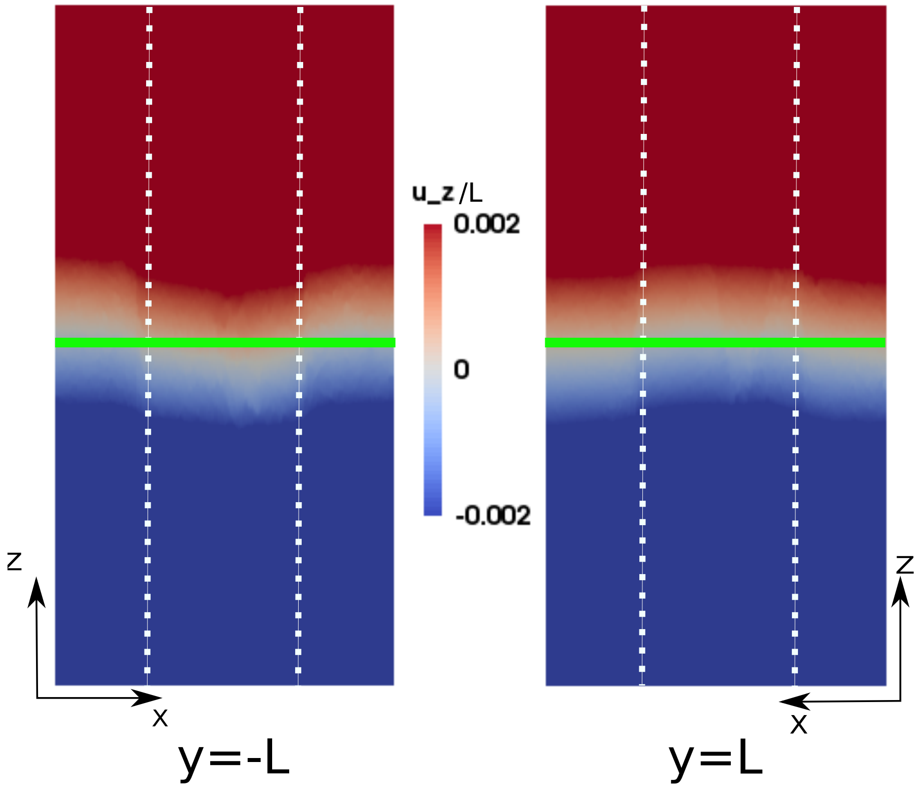

Figure 4.10: Displacement u_z on the surface $y = -L$ and on the surface $y = L$; the while dashed lines are two interfaces of layers, the green line is the $z = 0$ line which is the center of the surface

boundary conditions are given by the following equations.

$$\begin{cases} u_z = 0, & \text{on } Z = -\frac{L}{2} \\ u_z = 0.01L, & \text{on } Z = \frac{L}{2} \\ \vec{u} = \vec{0}, & \text{at node } (0,0,-\frac{L}{2}) \end{cases}$$

The material properties are given in Table 4.2. Table 4.2 implies that the crack is defined by setting the material property to 0 at the crack nodes. The crack domain is considered as nodes with a material property 0, which means the computational domain is the entire cubic Ω. To perform this numerical simulation, a specific treatment is required to deal with the infinite material property jump. This treatment involves in the following steps.

- Step A: The MF-FEM iterative solver for the relaxation step.
- Step B: The injection of solutions from the fine grid to the coarse grid.
- Step C: The restriction of residuals from the fine grid to the coarse grid.
- Step D: The prolongation of the corrections from the coarse grid to the fine grid.

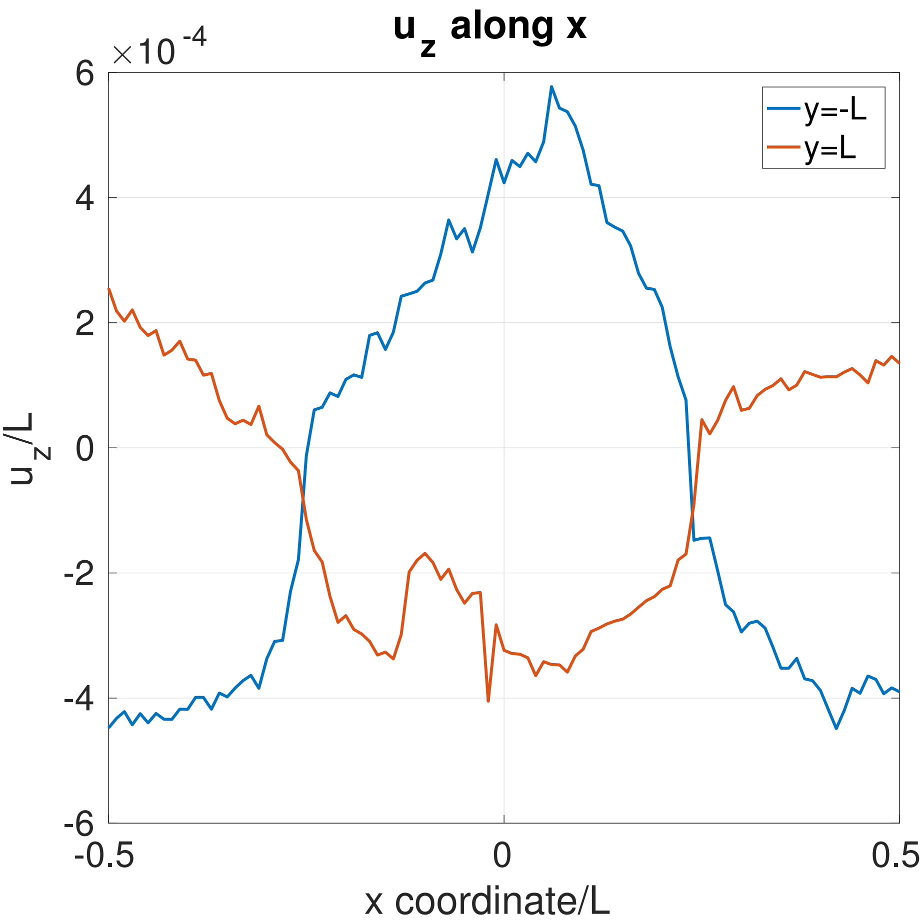

Figure 4.11: Displacement u_z along the line $z = 0$ on surface $y = -L$ and $y = L$ (see Figure 4.10 for position of line)

Tableau 4.2: Material properties in cast iron

Component	Young's modulus/GPa	Poisson ratio
Iron	210	0.3
Carbon granules	21	0.2
Crack	0	0

For "Step A": during the relaxation processing, the displacements on nodes without material are not updated.

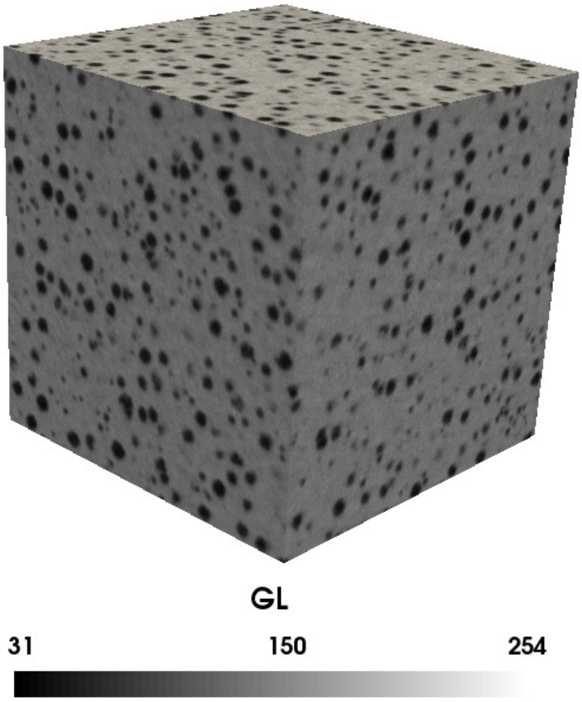

Figure 4.12: THE GL of the ROI of the CT image of cast iron

For ”Step B”: as mentioned above, the Reuss approximation is

$$K^{HR} = \frac{N_h}{\sum_1^{N_h} \frac{1}{K^h}},\ G^{HR} = \frac{N_h}{\sum_1^{N_h} \frac{1}{G^h}}$$

To avoid 0 in the denominator, one defines: if there is $K^h = 0$ and $G^h = 0$, then $K^{HR} = 0$ and $G^{HR} = 0$.

For ”Step C” and ”D”: the restriction and the prolongation process are done only when the material property on this node and on all of its nearest neighbor nodes is not 0 at the fine grid. If 0 appears in the denominator when computing the restriction matrix, one replaces it with 10^{-6}.

For the grids, one has $256\times256\times256$ elements on the finest level and $4\times4\times4$ elements on the coarsest level with 7 levels. The under-relaxation coefficient is taken to 0.5 for the Jacobi solver. The parameters of the FMG cycles are: $n_{cy} = 4$, $\nu_0 = 100$, $\nu_1 = 8$ and $\nu_2 = 4$. Since the displacement and the crack thickness are too small for the visualization, *i.e.* 1%, in the following figures the displacement is multiplied by a factor of 20.

Figure 4.14 illustrates the Young’s modulus and the strain field in the cast iron. It presents the strain concentrations on the crack front. The largest strain can be found in

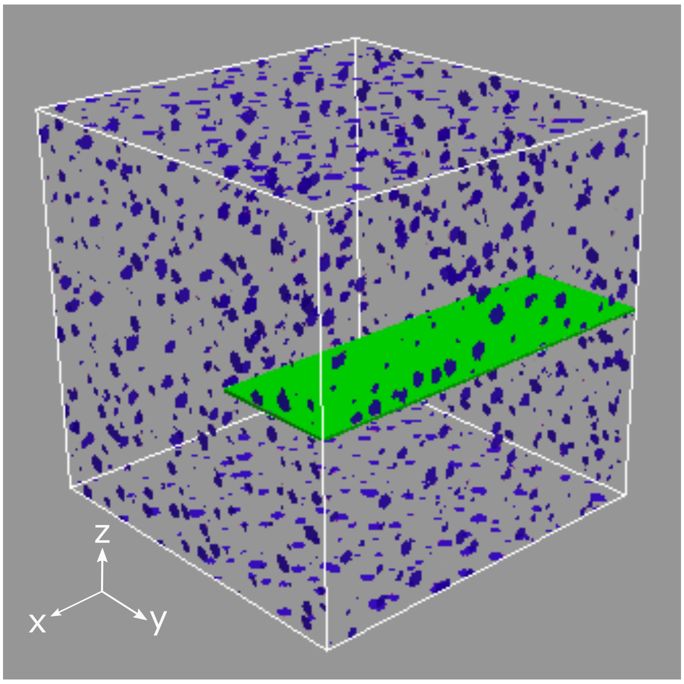

Figure 4.13: The prescribed rectangular crack in cast iron CT image

carbon nodules on the crack front. The largest strain is 10 times larger than the prescribed strain at the macroscopic scale, *i.e.* 1%. Other strain concentrations are located on carbon nodules, because carbon nodules are 10 times softer than iron.

Another simulation is carried out to compare the crack opening in a homogeneous material and in a heterogeneous material. The principle is to replace all the carbon nodules in the CT image by iron, which means the simulation is carried with a prescribed crack in the iron. The same boundary conditions are applied on the simulation of the crack opening in iron. Figure 4.15 shows the strain field in the homogeneous iron and heterogeneous cast iron. The strain field in the iron presents typical butterfly strain concentrations in the homogeneous materials after the crack opening. Compared to the strain concentrations in the iron, the strain concentrations in the cast iron are not only in the vicinity of the crack front but also in the carbon nodules over the entire volume. The material heterogeneity spreads strain concentrations in a large volume. Figure 4.16 illustrates the strain concentrations on the crack front in the iron and in the cast iron, respectively. The largest strain is located on carbon nodules on the crack front in the cast iron, but in iron, a uniform strain concentration can be found on the entire crack front. This should lead to non rectilinear crack front (if crack propagation is performed) and strong interactions between the crack and the material microstructure.

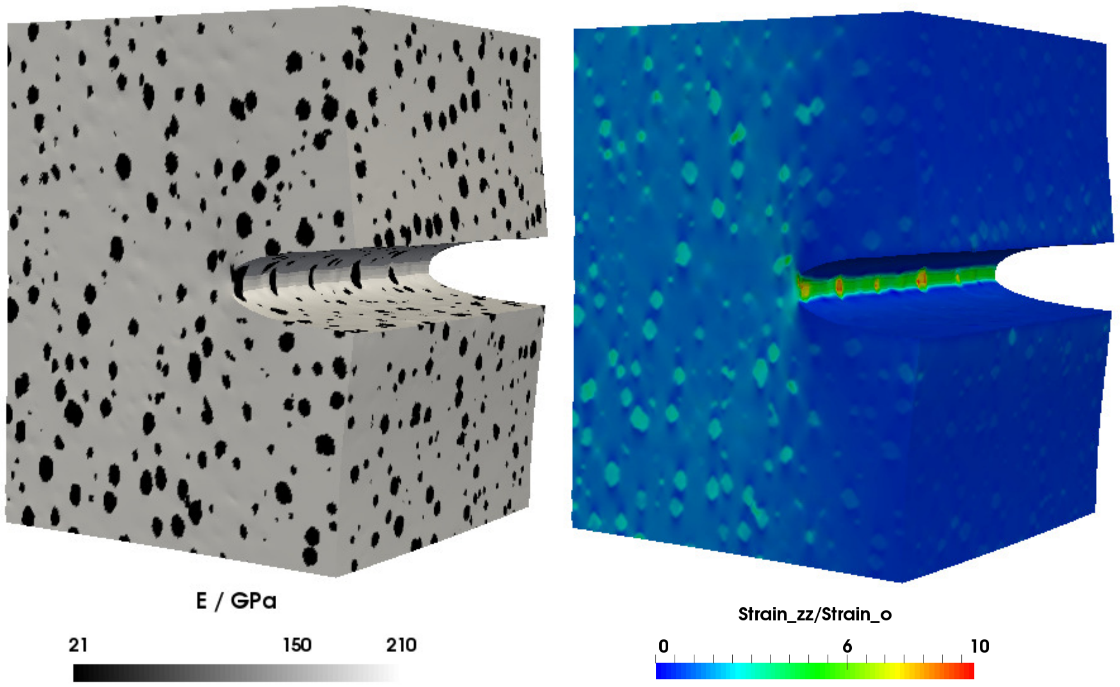

Figure 4.14: The Young's modulus and the strain$_{zz}$ in cast iron

4.5 Conclusion

In this chapter, the proposed strategy is developed for the mechanical problems. The free edge effect is analyzed by using the the CT image of an E–glass fiber reinforced plastic laminated structure. The numerical simulation with more than 18 DoF implies the possibility to carry out CT simulations with larger area, The good correlation between the numerical simulation and the DIC experiment demonstrated the importance to carry out simulations directly from CT images but not using the theoretical microstructures. The analyze of crack opening confirms that one can perform CT simulations to analyze the mechanical behavior of heterogeneous materials.

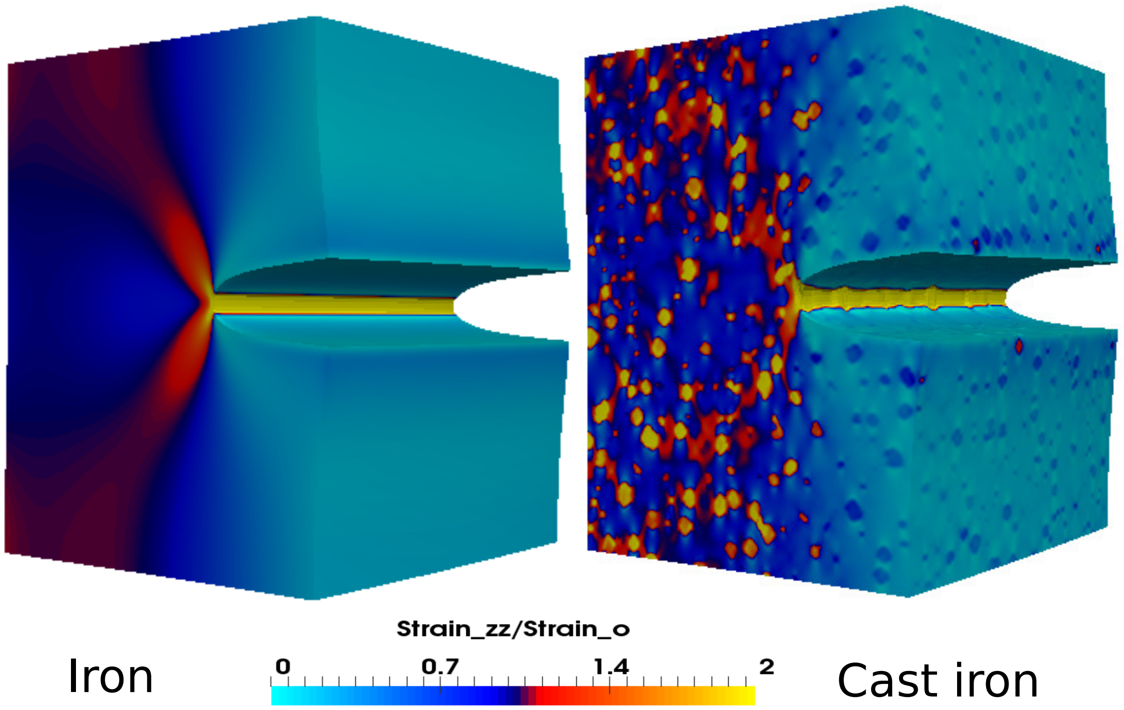

Figure 4.15: Strain$_{zz}$ in iron and in cast iron

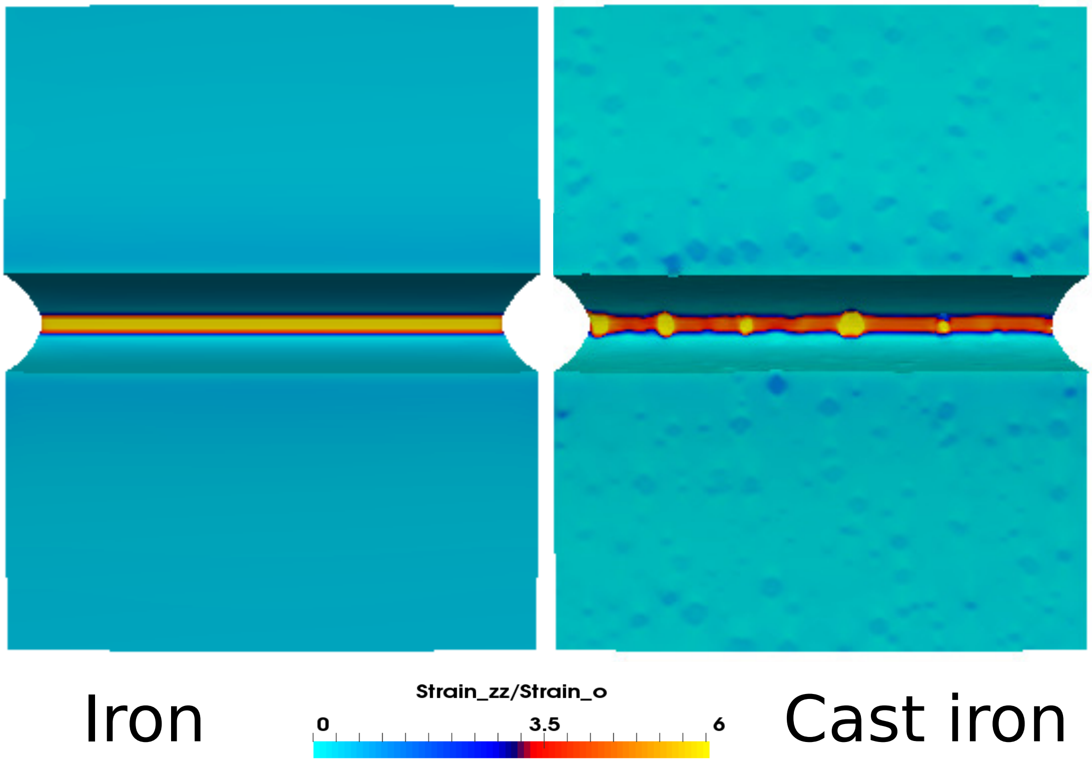

Figure 4.16: Strain concentrations on the crack font in the cast iron and in the iron

General conclusions and perspectives

General conclusion

As stated at the beginning of this thesis, the objective of this work is to develop an automatic and efficient solver for the CT image simulations. To achieve this final objective, we started by analyzing the suitable numerical methods. After reviewing all the commonly used methods, the matrix free finite element method is finally chosen in this work. The MF-FEM has a large advantage for the voxel conversion problems. It diminishes memory requirement. To deal with the slow convergence of the MF-FEM, the MultiGrid method is applied to speedup convergence. The comparison between the MG method and the single level Jacobi iterative solver shows the efficiency of the MG method. Several specific strategies are proposed to overcome the drawbacks of the MG method, when large material properties variations are involved. The comparison between different MG methods demonstrates the stability and the efficiency of the proposed strategy. The new homogenization technique proposed in this work is very efficient and suitable to compute the coarse grid operator of the MG method. To obtain a complete strategy, a parallel computing is applied to the MF-FEM based MultiGrid method. An efficiency of 80% is achieved for simulation with about 1000 cores simultaneously. The entire program, including the input and output, is developed using C/C++ with the hybrid MPI+OpenMP. The solver can automatically read information from CT images and carry out the numerical simulations itself and finally output the result in vtk and pvtk files. The entire process requires little human intervention.

Compared to [ARB 08], we apply the standard MG method to the matrix free element method, which is simpler. Meanwhile, for the voxel conversion problem, we use only cubic elements, the aggregation-based MultiGrid method can not show its advantage for this structural grid. [ARB 08] performed the CT simulation on a human bone, *i.e.*, homogeneous material, within one billion of DoF. In this work, using more than 16 billion DoF, we achieved a parallel efficiency of about 80%. Moreover, the effect of material heterogeneity is studied in this work.

The proposed method is developed on the thermal conduction problem. It is extended for mechanical problems. The mechanical applications imply that employing the CT simulations can help researchers to understand the material behavior at the microscopic scale. It permits ones to predict the effects of the defects in materials and to improve performance. The study about the free edge effects demonstrates the advantage and the power of using the CT images at the microscopic scale. The good correlation between the CT simulations and the DIC experiment verifies the necessity of carrying out simulations with real microstructures. The simulation with more than 16 billion DoF for a real tomography image demonstrates the efficiency and the stability of the proposed strategy. It implies the possibility to carry out CT simulations in larger domain. The crack opening application confirms the stability of the proposed strategy. It can deal with problems with infinite material property jumps between cracks and materials. The interaction between the crack and the microstructure is also observed by CT simulations.

Perspectives

In this work, a qualitative comparison is performed between CT simulations and DIC experiments. For the next step, a quantitative comparison is more interesting. One of challenges to perform this quantitative comparison, is that the DIC measurement is performed with a precision of about ten voxels. However, the CT simulation has a precision until one voxel. A strategy shall be proposed to perform this comparison.

With the quantitative comparison between the CT simulation and the DIC experiment, one can try to identify the real material properties of each constituent in heterogeneous materials. The principle is to prescribe the DIC measurement as boundary conditions in the simulation and to optimize the different between the simulation and experiment to find the good material properties of each constituent. With this good material properties of each constituent, one can well predict material behavior by CT simulations.

The problem of crack opening is analyzed in this work. However, it does not study the real crack propagation. The crack propagation by the phase field method can be carried out using the proposed strategy. For the crack propagation in the brittle materials, there are two parts: linear elasticity and crack propagation. In the equations of the phase field method (4.5), we can see two essential parts. One is similar to the elastic problem, the other is similar to the thermal conduction problem. A next step is to combine these two parts.

$$\begin{cases} 2(1-d)\mathcal{H} - \frac{g_c}{l}(d - l^2\Delta d) = 0 & \text{in } \Omega \\ d(\boldsymbol{x}) = 1 & \text{on } \Gamma \\ \nabla d(\boldsymbol{x}) \cdot \boldsymbol{n} = 0 & \text{on } \partial\Omega \end{cases}$$

With the CT simulation on the crack propagation problems at the microscopic scale, the interaction between microstructures and crack propagation can be analyzed. One can obtain the propagation law for the same material at the macroscopic scale. It permits one to carry out crack propagation in large structures with a good precision and to better understand and predict material behavior.

Appendix A

Formulations of several analytical homogenization methods

The following analytical homogenization formulations are destined for the tow-phase inclusion of the linear thermal conduction problems. The following formulation is presented under these conditions:

- It is a two-phase particulate microstructure.
- The material is isotropic

Supposing the conductivity of the matrix is α_m, and α_s for the inhomogeneity with $\alpha_s > \alpha_m$. The volume fraction is V_m for matrix and V_s for the inhomogeneity. The effective thermal conductivity is α_e. The dimension of the problem is d, $d = 2$ for 2D, $d = 3$ for 3D.

Voigt-Reuss bounds

The Voigt-Reuss lower bound is:

$$\alpha_e^{VR-} = \frac{V_m + V_s}{\frac{V_m}{\alpha_m} + \frac{V_s}{\alpha_s}}$$

The Voigt-Reuss upper bound is:

$$\alpha_e^{VR+} = \frac{V_m \alpha_m + V_s \alpha_s}{V_m + V_s}$$

Hashin-Shtrikman bounds

The Hashin-Shtrikman lower bound is:

$$\alpha_e^{HS-} = \alpha_e^{VR+} - \frac{V_m V_s (\alpha_s - \alpha_m)^2}{\tilde{\alpha} + (d-1)\alpha_m}$$

with

$$\tilde{\alpha} = V_m \alpha_s + V_s \alpha_m$$

The Hashin-Shtrikman upper bound is:

$$\alpha_e^{HS-} = \alpha_e^{VR+} - \frac{V_m V_s (\alpha_s - \alpha_m)^2}{\tilde{\alpha} + (d-1)\alpha_s}$$

Self-Consistent method

The process of the Self-Consistent method is to find the α_e^{SC} with the following equation:

$$V_m \frac{\alpha_m - \alpha_e^{SC}}{\alpha_m + (d-1)\alpha_e^{SC}} + V_s \frac{\alpha_s - \alpha_e^{SC}}{\alpha_s + (d-1)\alpha_e^{SC}} = 0$$

Eshelby's tensor for a spherical inclusion

The following Eshelby's tensor is for the spherical inclusion of a linear elastic problem in isotropic materials.

$$\boldsymbol{S} = \frac{1}{15(1-\nu)} \begin{pmatrix} 7-5\nu & 5\nu-1 & 5\nu-1 & 0 & 0 & 0 \\ 5\nu-1 & 7-5\nu & 5\nu-1 & 0 & 0 & 0 \\ 5\nu-1 & 5\nu-1 & 7-5\nu & 0 & 0 & 0 \\ 0 & 0 & 0 & 4-5\nu & 0 & 0 \\ 0 & 0 & 0 & 0 & 4-5\nu & 0 \\ 0 & 0 & 0 & 0 & 0 & 4-5\nu \end{pmatrix}$$

where ν is the Poisson ratio of inclusion.

Bibliography

[ADA 99] ADAMS M. F.
Multigrid equation solvers for large scale nonlinear finite element simulations. rapport, 1999, CALIFORNIA UNIV BERKELEY DEPT OF ELECTRICAL ENGINEERING AND COMPUTER SCIENCES.

[ADE 91] ADELI H.
Parallel processing in computational mechanics, vol. 2. Crc Press, 1991.

[ALC 81] ALCOUFFE R., BRANDT A., DENDY JR J., PAINTER J.
The multi-grid method for the diffusion equation with strongly discontinuous coefficients. *SIAM Journal on Scientific and Statistical Computing*, vol. 2, n° 4, 1981, p. 430–454, SIAM.

[ANG 60] ANGUS H. T.
Physical and engineering properties of cast iron: a data book for engineers and designers. British Cast Iron Research Association, 1960.

[ANN 07] ANNAPRAGADA S. R., SUN D., GARIMELLA S. V.
Prediction of effective thermo-mechanical properties of particulate composites. *Computational Materials Science*, vol. 40, n° 2, 2007, p. 255–266, Elsevier.

[ARB 08] ARBENZ P., VAN LENTHE G. H., MENNEL U., MÜLLER R., SALA M.
A scalable multi-level preconditioner for matrix-free μ-finite element analysis of human bone structures. *International Journal for Numerical Methods in Engineering*, vol. 73, n° 7, 2008, p. 927–947, Wiley Online Library.

[AUB 11] AUBRY R., HOUZEAUX G., VAZQUEZ M., CELA J.
Some useful strategies for unstructured edge-based solvers on shared memory machines. *International journal for numerical methods in engineering*, vol. 85, n° 5, 2011, p. 537–561, Wiley Online Library.

[AUG 06] AUGARDE C., RAMAGE A., STAUDACHER J.
An element-based displacement preconditioner for linear elasticity problems. *Computers & structures*, vol. 84, n° 31-32, 2006, p. 2306–2315, Elsevier.

[BAK 12] BAKHVALOV N. S., PANASENKO G.
Homogenisation: averaging processes in periodic media: mathematical problems in

the mechanics of composite materials, vol. 36. Springer Science & Business Media, 2012.

[BEN 87] BENVENISTE Y.
A new approach to the application of Mori-Tanaka's theory in composite materials. *Mechanics of materials*, vol. 6, n° 2, 1987, p. 147–157, Elsevier.

[BER 06] BERGEN B., GRADL T., HULSEMANN F., RUDE U.
A massively parallel multigrid method for finite elements. *Computing in science & engineering*, vol. 8, n° 6, 2006, p. 56–62, IEEE.

[BES 07] BESSHO M., OHNISHI I., MATSUYAMA J., MATSUMOTO T., IMAI K., NAKAMURA K.
Prediction of strength and strain of the proximal femur by a CT-based finite element method. *Journal of biomechanics*, vol. 40, n° 8, 2007, p. 1745–1753, Elsevier.

[BIB 13] BIBOULET N., GRAVOUIL A., DUREISSEIX D., LUBRECHT A., COMBESCURE A.
An efficient linear elastic FEM solver using automatic local grid refinement and accuracy control. *Finite Elements in Analysis and Design*, vol. 68, 2013, p. 28–38, Elsevier.

[BIL 07] BILGER N., AUSLENDER F., BORNERT M., MOULINEC H., ZAOUI A.
Bounds and estimates for the effective yield surface of porous media with a uniform or a nonuniform distribution of voids. *European Journal of Mechanics-A/Solids*, vol. 26, n° 5, 2007, p. 810–836, Elsevier.

[BOF 12a] BOFFY H.
Techniques multigrilles et raffinement pour un modèle 3D efficace de milieux hétérogènes sous sollicitations de contact. PhD thesis, INSA Lyon, 9 2012.

[BOF 12b] BOFFY H., BAIETTO M.-C., SAINSOT P., LUBRECHT A. A.
An efficient 3d model of heterogeneous materials for elastic contact applications using multigrid methods. *Journal of tribology*, vol. 134, n° 2, 2012, p. 021401, American Society of Mechanical Engineers.

[BOF 14] BOFFY H., VENNER C. H.
Multigrid solution of the 3D stress field in strongly heterogeneous materials. *Tribology international*, vol. 74, 2014, p. 121–129, Elsevier.

[BOF 15] BOFFY H., VENNER C. H.
Multigrid numerical simulation of contact mechanics of elastic materials with 3D heterogeneous subsurface topology. *Tribology international*, vol. 92, 2015, p. 233–245, Elsevier.

[BRA 77] BRANDT A.
Multi-level adaptive techniques (MLAT) for partial differential equations: ideas and software. *Mathematical software*, p. 277–318 Elsevier, 1977.

[BRA 81] BRANDT A.
Multigrid solvers on parallel computers. *Elliptic Problem Solvers*, p. 39–83 Elsevier, 1981.

[BRA 85] BRAND G.
Multigrid methods in finite element analysis of plane elastic structures. , 1985.

[BRA 88] BRAESS D.
A multigrid method for the membrane problem. *Computational mechanics*, vol. 3, n^o 5, 1988, p. 321–329, Springer.

[BRA 11] BRANDT A., LIVNE O. E.
Multigrid techniques: 1984 guide with applications to fluid dynamics, vol. 67. SIAM, 2011.

[BUD 65] BUDIANSKY B.
On the elastic moduli of some heterogeneous materials. *Journal of the Mechanics and Physics of Solids*, vol. 13, n^o 4, 1965, p. 223–227, Elsevier.

[CAR 86] CAREY G. F., JIANG B.-N.
Element-by-element linear and nonlinear solution schemes. *Communications in Applied Numerical Methods*, vol. 2, n^o 2, 1986, p. 145–153, Wiley Online Library.

[CHE 02] CHENOT J.-L., FOURMENT L., MOCELLIN K.
Numerical treatment of contact and friction in FE simulation of forming processes. *Journal of Materials Processing Technology*, vol. 125, 2002, p. 45–52, Elsevier.

[CIO 99] CIORANESCU D., DONATO P.
An introduction to homogenization. Oxford University Press, 1999.

[DIG 19] DIGONNET H., COUPEZ T., LAURE P., SILVA L.
Massively parallel anisotropic mesh adaptation. *The International Journal of High Performance Computing Applications*, vol. 33, n^o 1, 2019, p. 3–24, SAGE Publications Sage UK: London, England.

[DOW 90] DOW J. O., JONES M. S., HARWOOD S. A.
A new approach to boundary modelling for finite difference applications in solid mechanics. *International Journal for Numerical Methods in Engineering*, vol. 30, n^o 1, 1990, p. 99–113, Wiley Online Library.

[DUR 96] DURST F., SCHÄFER M.
A parallel block-structured multigrid method for the prediction of incompressible

flows. *International Journal for Numerical Methods in Fluids*, vol. 22, n° 6, 1996, p. 549–565, Wiley Online Library.

[ELL 88] ELLIOTT R.
Cast iron technology. Butterworth-Heinemann, 1988.

[ENG 96] ENGQUIST B., LUO E.
New coarse grid operators for highly oscillatory coefficient elliptic problems. *Journal of Computational Physics*, vol. 129, n° 2, 1996, p. 296–306, Elsevier.

[ENG 97] ENGQUIST B., LUO E.
Convergence of a multigrid method for elliptic equations with highly oscillatory coefficients. *SIAM journal on numerical analysis*, vol. 34, n° 6, 1997, p. 2254–2273, SIAM.

[ESH 57] ESHELBY J. D.
The determination of the elastic field of an ellipsoidal inclusion, and related problems. *Proceedings of the Royal Society of London. Series A. Mathematical and Physical Sciences*, vol. 241, n° 1226, 1957, p. 376–396, The Royal Society London.

[ESH 59] ESHELBY J. D.
The elastic field outside an ellipsoidal inclusion. *Proceedings of the Royal Society of London. Series A. Mathematical and Physical Sciences*, vol. 252, n° 1271, 1959, p. 561–569, The Royal Society London.

[EYR 99] EYRE D. J., MILTON G. W.
A fast numerical scheme for computing the response of composites using grid refinement. *The European Physical Journal-Applied Physics*, vol. 6, n° 1, 1999, p. 41–47, EDP Sciences.

[FED 62] FEDORENKO R. P.
A relaxation method for solving elliptic difference equations. *USSR Computational Mathematics and Mathematical Physics*, vol. 1, n° 4, 1962, p. 1092–1096, Elsevier.

[FED 64] FEDORENKO R. P.
The speed of convergence of one iterative process. *USSR Computational Mathematics and Mathematical Physics*, vol. 4, n° 3, 1964, p. 227–235, Elsevier.

[FER 99] FERRANT M., WARFIELD S. K., GUTTMANN C. R., MULKERN R. V., JOLESZ F. A., KIKINIS R.
3D image matching using a finite element based elastic deformation model. *International Conference on Medical Image Computing and Computer-Assisted Intervention* Springer, 1999, p. 202–209.

[FIS 07] FISH J., BELYTSCHKO T.
A first course in finite elements. Wiley, 2007.

[FOU 99] FOURMENT L., CHENOT J.-L., MOCELLIN K.
Numerical formulations and algorithms for solving contact problems in metal forming simulation. *International Journal for Numerical Methods in Engineering*, vol. 46, n$^{\text{o}}$ 9, 1999, p. 1435–1462, Wiley Online Library.

[GAH 12] GAHVARI H., GROPP W., JORDAN K. E., SCHULZ M., YANG U. M.
Modeling the performance of an algebraic multigrid cycle using hybrid mpi/openmp. *2012 41st International Conference on Parallel Processing* IEEE, 2012, p. 128–137.

[GRO 99] GROPP W. D., GROPP W., LUSK E., SKJELLUM A.
Using MPI: portable parallel programming with the message-passing interface, vol. 1. MIT press, 1999.

[GU 16] GU H., RÉTHORÉ J., BAIETTO M.-C., SAINSOT P., LECOMTE-GROSBRAS P., VENNER C. H., LUBRECHT A. A.
An efficient MultiGrid solver for the 3D simulation of composite materials. *Computational materials science*, vol. 112, 2016, p. 230–237, Elsevier.

[HAS 62a] HASHIN Z., SHTRIKMAN S.
On some variational principles in anisotropic and nonhomogeneous elasticity. *Journal of the Mechanics and Physics of Solids*, vol. 10, n$^{\text{o}}$ 4, 1962, p. 335–342, Elsevier.

[HAS 62b] HASHIN Z., SHTRIKMAN S.
A variational approach to the theory of the elastic behaviour of polycrystals. *Journal of the Mechanics and Physics of Solids*, vol. 10, n$^{\text{o}}$ 4, 1962, p. 343–352, Elsevier.

[HAS 64] HASHIN Z., ROSEN B. W.
The elastic moduli of fiber-reinforced materials. *Journal of applied mechanics*, vol. 31, n$^{\text{o}}$ 2, 1964, p. 223–232, American Society of Mechanical Engineers Digital Collection.

[HEE 97] HEERAMAN D. A., HOPMANS J. W., CLAUSNITZER V.
Three dimensional imaging of plant roots in situ with X-ray computed tomography. *Plant and soil*, vol. 189, n$^{\text{o}}$ 2, 1997, p. 167–179, Springer.

[HEL 91] HELSING J., GRIMVALL G.
Thermal conductivity of cast iron: models and analysis of experiments. *Journal of applied physics*, vol. 70, n$^{\text{o}}$ 3, 1991, p. 1198–1206, AIP.

[HER 54] HERSHEY A.
The elasticity of an isotropic aggregate of anisotropic cubic crystals. *Journal of Applied mechanics-transactions of the ASME*, vol. 21, n$^{\text{o}}$ 3, 1954, p. 236–240, ASME-AMER SOC MECHANICAL ENG 345 E 47TH ST, NEW YORK, NY 10017.

[HIL 65] HILL R.
A self-consistent mechanics of composite materials. *Journal of the Mechanics and Physics of Solids*, vol. 13, n$^{\text{o}}$ 4, 1965, p. 213–222, Elsevier.

[HIR 95] HIRANO T., USAMI K., TANAKA Y., MASUDA C.
In situ x-ray CT under tensile loading using synchrotron radiation. *Journal of materials research*, vol. 10, n$^{\rm o}$ 2, 1995, p. 381–386, Cambridge University Press.

[HOE 98] HOEKEMA R., VENNER K., STRUIJK J. J., HOLSHEIMER J.
Multigrid solution of the potential field in modeling electrical nerve stimulation. *Computers and Biomedical Research*, vol. 31, n$^{\rm o}$ 5, 1998, p. 348–362, Academic Press.

[HUG 83] HUGHES T. J., LEVIT I., WINGET J.
An element-by-element solution algorithm for problems of structural and solid mechanics. *Computer Methods in Applied Mechanics and Engineering*, vol. 36, n$^{\rm o}$ 2, 1983, p. 241–254, Elsevier.

[HUG 87] HUGHES T. J., FERENCZ R. M., HALLQUIST J. O.
Large-scale vectorized implicit calculations in solid mechanics on a Cray X-MP/48 utilizing EBE preconditioned conjugate gradients. *Computer Methods in Applied Mechanics and Engineering*, vol. 61, n$^{\rm o}$ 2, 1987, p. 215–248, Elsevier.

[IDI 09] IDIART M. I., WILLOT F., PELLEGRINI Y.-P., CASTANEDA P. P.
Infinite-contrast periodic composites with strongly nonlinear behavior: Effective-medium theory versus full-field simulations. *International Journal of Solids and Structures*, vol. 46, n$^{\rm o}$ 18-19, 2009, p. 3365–3382, Elsevier.

[KAN 03] KANIT T., FOREST S., GALLIET I., MOUNOURY V., JEULIN D.
Determination of the size of the representative volume element for random composites: statistical and numerical approach. *International Journal of solids and structures*, vol. 40, n$^{\rm o}$ 13-14, 2003, p. 3647–3679, Elsevier.

[KAR 03] KARNIADAKIS G. E., KARNIADAKIS G., KIRBY II R. M.
Parallel scientific computing in C++ and MPI: a seamless approach to parallel algorithms and their implementation, vol. 2. Cambridge University Press, 2003.

[KAR 07] KARI S., BERGER H., RODRIGUEZ-RAMOS R., GABBERT U.
Computational evaluation of effective material properties of composites reinforced by randomly distributed spherical particles. *Composite structures*, vol. 77, n$^{\rm o}$ 2, 2007, p. 223–231, Elsevier.

[KRO 18] KRONBICHLER M., WALL W. A.
A performance comparison of continuous and discontinuous Galerkin methods with fast multigrid solvers. *SIAM Journal on Scientific Computing*, vol. 40, n$^{\rm o}$ 5, 2018, p. A3423–A3448, SIAM.

[KUM 02] KUMAR V.
Introduction to parallel computing. Addison-Wesley Longman Publishing Co., Inc., 2002.

[LAR 13] LARSON M. G., BENGZON F.
The finite element method: theory, implementation, and applications, vol. 10. Springer Science & Business Media, 2013.

[LEC 09] LECOMTE-GROSBRAS P., PALUCH B., BRIEU M., DE SAXCÉ G., SABATIER L.
Interlaminar shear strain measurement on angle-ply laminate free edge using digital image correlation. *Composites Part A: Applied Science and Manufacturing*, vol. 40, n^{o} 12, 2009, p. 1911–1920, Elsevier.

[LEC 15] LECOMTE-GROSBRAS P., RÉTHORÉ J., LIMODIN N., WITZ J.-F., BRIEU M.
Three-dimensional investigation of free-edge effects in laminate composites using x-ray tomography and digital volume correlation. *Experimental Mechanics*, vol. 55, n^{o} 1, 2015, p. 301–311, Springer.

[LEG 11] LEGRAIN G., CARTRAUD P., PERREARD I., MOËS N.
An X-FEM and level set computational approach for image-based modelling: application to homogenization. *International Journal for Numerical Methods in Engineering*, vol. 86, n^{o} 7, 2011, p. 915–934, Wiley Online Library.

[LEG 12] LEGRAIN G., CHEVAUGEON N., DRÉAU K.
High order X-FEM and levelsets for complex microstructures: uncoupling geometry and approximation. *Computer Methods in Applied Mechanics and Engineering*, vol. 241, 2012, p. 172–189, Elsevier.

[LEN 98] LENGSFELD M., SCHMITT J., ALTER P., KAMINSKY J., LEPPEK R.
Comparison of geometry-based and CT voxel-based finite element modelling and experimental validation. *Medical engineering & physics*, vol. 20, n^{o} 7, 1998, p. 515–522, Elsevier.

[LIA 13] LIAN W.-D., LEGRAIN G., CARTRAUD P.
Image-based computational homogenization and localization: comparison between X-FEM/levelset and voxel-based approaches. *Computational Mechanics*, vol. 51, n^{o} 3, 2013, p. 279–293, Springer.

[LIU 19] LIU X., RÉTHORÉ J., BAIETTO M.-C., SAINSOT P., LUBRECHT A. A.
An efficient strategy for large scale 3D simulation of heterogeneous materials to predict effective thermal conductivity. *Computational materials science*, vol. 166, 2019, p. 265–275, Elsevier.

[MCB 91] MCBRYAN O. A., FREDERICKSON P. O., LINDENAND J., SCHÜLLER A., SOLCHENBACH K., STÜBEN K., THOLE C.-A., TROTTENBERG U.
Multigrid methods on parallel computers - a survey of recent developments. *IMPACT of Computing in Science and Engineering*, vol. 3, n^{o} 1, 1991, p. 1–75, Elsevier.

[MES 08] MESRI Y., ZERGUINE W., DIGONNET H., SILVA L., COUPEZ T.
Dynamic parallel adaption for three dimensional unstructured meshes: Application to interface tracking. *Proceedings of the 17th International Meshing Roundtable*, p. 195–212 Springer, 2008.

[MIC 10] MICHAILIDIS N., STERGIOUDI F., OMAR H., TSIPAS D.
An image-based reconstruction of the 3D geometry of an Al open-cell foam and FEM modeling of the material response. *Mechanics of Materials*, vol. 42, n^{o} 2, 2010, p. 142–147, Elsevier.

[MOR 73] MORI T., TANAKA K.
Average stress in matrix and average elastic energy of materials with misfitting inclusions. *Acta metallurgica*, vol. 21, n^{o} 5, 1973, p. 571–574, Elsevier.

[MOU 98] MOULINEC H., SUQUET P.
A numerical method for computing the overall response of nonlinear composites with complex microstructure. *Computer methods in applied mechanics and engineering*, vol. 157, n^{o} 1-2, 1998, p. 69–94, Elsevier.

[NAK 12] NAKAJIMA K.
New strategy for coarse grid solvers in parallel multigrid methods using OpenMP/MPI hybrid programming models. *Proceedings of the 2012 International Workshop on Programming Models and Applications for Multicores and Manycores* ACM, 2012, p. 93–102.

[NEM 82] NEMAT-NASSER S., IWAKUMA T., HEJAZI M.
On composites with periodic structure. *Mechanics of materials*, vol. 1, n^{o} 3, 1982, p. 239–267, Elsevier.

[NGU 17] NGUYEN T.-T., RETHORE J., YVONNET J., BAIETTO M.-C.
Multi-phase-field modeling of anisotropic crack propagation for polycrystalline materials. *Computational Mechanics*, vol. 60, n^{o} 2, 2017, p. 289–314, Springer.

[OLE 84] OLEINIK O.
On homogenization problems. *Trends and applications of pure mathematics to mechanics*, p. 248–272 Springer, 1984.

[ÖZD 08] ÖZDEMIR I., BREKELMANS W., GEERS M.
Computational homogenization for heat conduction in heterogeneous solids. *International journal for numerical methods in engineering*, vol. 73, n^{o} 2, 2008, p. 185–204, Wiley Online Library.

[PAP 78] PAPANICOLAU G., BENSOUSSAN A., LIONS J.-L.
Asymptotic analysis for periodic structures, vol. 5. Elsevier, 1978.

[PAR 90a] PARSONS I., HALL J.
The multigrid method in solid mechanics: part I-algorithm description and behaviour. *International Journal for Numerical Methods in Engineering*, vol. 29, n° 4, 1990, p. 719–737, Wiley Online Library.

[PAR 90b] PARSONS I., HALL J.
The multigrid method in solid mechanics: part II-practical applications. *International Journal for Numerical Methods in Engineering*, vol. 29, n° 4, 1990, p. 739–753, Wiley Online Library.

[PAS 11] PASSIEUX J.-C., GRAVOUIL A., RÉTHORÉ J., BAIETTO M.-C.
Direct estimation of generalized stress intensity factors using a three-scale concurrent multigrid X-FEM. *International Journal for Numerical Methods in Engineering*, vol. 85, n° 13, 2011, p. 1648–1666, Wiley Online Library.

[PIP 94] PIPES R. B., PAGANO N.
Interlaminar stresses in composite laminates under uniform axial extension. *Mechanics of composite materials*, p. 234–245 Springer, 1994.

[PRO 16] PROUDHON H., LI J., WANG F., ROOS A., CHIARUTTINI V., FOREST S.
3D simulation of short fatigue crack propagation by finite element crystal plasticity and remeshing. *International Journal of Fatigue*, vol. 82, 2016, p. 238–246, Elsevier.

[RAB 09] RABENSEIFNER R., HAGER G., JOST G.
Hybrid MPI/OpenMP parallel programming on clusters of multi-core SMP nodes. *2009 17th Euromicro international conference on parallel, distributed and network-based processing* IEEE, 2009, p. 427–436.

[RAD 05] RADON J.
1.1 über die bestimmung von funktionen durch ihre integralwerte längs gewisser mannigfaltigkeiten. *Classic papers in modern diagnostic radiology*, vol. 5, 2005, p. 21, Springer Berlin–Heidelberg–New York.

[RAN 10] RANNOU J., LIMODIN N., RÉTHORÉ J., GRAVOUIL A., LUDWIG W., BAÏETTO-DUBOURG M.-C., BUFFIERE J.-Y., COMBESCURE A., HILD F., ROUX S.
Three dimensional experimental and numerical multiscale analysis of a fatigue crack. *Computer methods in applied mechanics and engineering*, vol. 199, n° 21-22, 2010, p. 1307–1325, Elsevier.

[RIE 96] VAN RIETBERGEN B., WEINANS H., HUISKES R., POLMAN B.
Computational strategies for iterative solutions of large FEM applications employing voxel data. *International Journal for Numerical Methods in Engineering*, vol. 39, n° 16, 1996, p. 2743–2767, Wiley Online Library.

[RUB 13] RUBLON P., HUNEAU B., SAINTIER N., BEURROT S., LEYGUE A., VERRON E., MOCUTA C., THIAUDIÈRE D., BERGHEZAN D.
In situ synchrotron wide-angle X-ray diffraction investigation of fatigue cracks in natural rubber. *Journal of synchrotron radiation*, vol. 20, n° 1, 2013, p. 105–109, International Union of Crystallography.

[RUG 87] RUGE J. W., STÜBEN K.
Algebraic multigrid. *Multigrid methods*, p. 73–130 SIAM, 1987.

[SÁN 80] SÁNCHEZ-PALENCIA E.
Non-homogeneous media and vibration theory. *Lecture notes in physics*, vol. 127, 1980, Springer-Verlag.

[SCH 96] SCHENA M., SHALON D., HELLER R., CHAI A., BROWN P. O., DAVIS R. W.
Parallel human genome analysis: microarray-based expression monitoring of 1000 genes. *Proceedings of the National Academy of Sciences*, vol. 93, n° 20, 1996, p. 10614–10619, National Acad Sciences.

[SMI 85] SMITH G. D., SMITH G. D., SMITH G. D. S.
Numerical solution of partial differential equations: finite difference methods. Oxford university press, 1985.

[SOR 17] SORBA G., BINETRUY C., LEYGUE A., COMAS-CARDONA S.
Squeeze flow in heterogeneous unidirectional discontinuous viscous prepreg laminates: Experimental measurement and 3D modeling. *Composites Part A: Applied Science and Manufacturing*, vol. 103, 2017, p. 196–207, Elsevier.

[SUQ 90] SUQUET P.
Une méthode simplifiée pour le calcul des propriétés élastiques de matériaux hétérogènes à structure périodique. *Comptes rendus de l'Académie des sciences. Série 2, Mécanique, Physique, Chimie, Sciences de l'univers, Sciences de la Terre*, vol. 311, n° 7, 1990, p. 769–774, Gauthier-Villars.

[SVI 15] SVIERCOSKI R. F., POPOV P., MARGENOV S.
An analytical coarse grid operator applied to a multiscale multigrid method. *Journal of Computational and Applied Mathematics*, vol. 287, 2015, p. 207–219, Elsevier.

[TAR 09] TARTAR L.
The general theory of homogenization: a personalized introduction, vol. 7. Springer Science & Business Media, 2009.

[TEZ 93] TEZDUYAR T., ALIABADI S., BEHR M., JOHNSON A., MITTAL S.
Parallel finite-element computation of 3D flows. *Computer*, vol. 26, n° 10, 1993, p. 27–36, IEEE.

[TRA 02] TRAFF J. L.
Implementing the MPI process topology mechanism. *SC'02: Proceedings of the 2002 ACM/IEEE Conference on Supercomputing* IEEE, 2002, p. 28–28.

[TRO 00] TROTTENBERG U., OOSTERLEE C. W., SCHULLER A.
Multigrid. Elsevier, 2000.

[VEN 00] VENNER C. H., LUBRECHT A. A.
Multi-level methods in lubrication, vol. 37. Elsevier, 2000.

[VIN 08] VINOGRADOV V., MILTON G.
An accelerated FFT algorithm for thermoelastic and non-linear composites. *International Journal for Numerical Methods in Engineering*, vol. 76, n^o 11, 2008, p. 1678–1695, Wiley Online Library.

[WAG 93] WAGNER D. B.
Iron and steel in ancient China, vol. 9. Brill, 1993.

[YAN 02] YANG U. M. et al.
BoomerAMG: a parallel algebraic multigrid solver and preconditioner. *Applied Numerical Mathematics*, vol. 41, n^o 1, 2002, p. 155–177, Elsevier.

[ZHA 19] ZHANG B., BOFFY H., VENNER C. H.
Multigrid solution of 2D and 3D stress fields in contact mechanics of anisotropic inhomogeneous materials. *Tribology international*, , 2019, Elsevier.

[ZIE 00] ZIENKIEWICZ O. C., TAYLOR R. L., TAYLOR R. L., TAYLOR R.
The finite element method: solid mechanics, vol. 2. Butterworth-heinemann, 2000.

List of Figures

List of Tables

Titre : Une méthode multigrille massivement parallèle à base d'éléments finis sans matrice pour la simulation des matériaux hétérogènes à partir d'images de tomographie

Mots clés : CT simulations, Multigrille, Calcul parallèle, Hétérogène, Homogénéisation

Résumé : Les simulations numériques à partir d'images de tomographie sont de plus en plus courantes depuis les vingt dernières années. Les simulations à l'échelle microscopique à partir d'images réelles de matériaux permettent aux chercheurs de connaître ses comportements thermiques et mécaniques, et d'améliorer leurs performances. Les difficultés de faire la simulation à partir d'images viennent de leur complexité et leur taille. La génération de maillages pour la microstructure complexe nécessite une intervention humaine pour l'utilisation de la méthode des éléments finis. Ces simulations à partir d'images de tomographie haute résolution demandent beaucoup de temps et de mémoire.

L'objectif de ce travail est de surmonter ces difficultés pour effectuer automatiquement des simulations numériques à partir d'images réelles des matériaux hétérogènes. Une méthode éléments finis sans matrice (MF-FEM) est utilisée pour diminuer les besoins en mémoire. Les méthodes de multigrille sont intégrées pour améliorer la convergence de la MF-FEM. Une technique efficace à la base d'homogénéisation est proposée pour traiter la mauvaise convergence de multigrille pour les problèmes avec grandes variations des propriétés des matériaux. Le calcul en parallèle hybride est aussi appliqué. Des simulations avec des milliards degrés de libertés sont effectuées sur des problèmes thermiques et mécaniques.

Title: A massively parallel matrix free finite element based MultiGrid method for simulations of heterogeneous materials using tomography images

Keywords: CT simulations, MultiGrid, Parallel computing, Heterogeneous, Homogenization

Abstract: Numerical simulations using X-ray based Computed Tomography (CT) images became more and more common in the last two decades. CT images give researchers ample information about material microstructures. Performing numerical simulation at the microscopical scale permits researchers to understand the thermal and mechanical behavior of materials, and to improve material performance. The difficulties of performing simulations come from the complexity and the dimension of images. The meshing generation for the complex microstructure requires human intervention when using the finite element method. Simulations using large scale CT images are memory and time consuming.

The objective is to overcome these difficulties and to perform automatically numerical simulations directly from CT images. The matrix free finite element method (MF-FEM) is applied to diminish the memory requirements. A MultiGrid (MG) method is used to improve the convergence of the MF-FEM. An efficient homogenization method to compute the coarse grid operator of MG methods is proposed to insure the convergence of MG methods for problems with large material property variations. Massively parallel computing is applied to deal with time consumption problem. Numerical simulations directly from CT images with billions of degrees of freedom are finally performed on the thermal and mechanical problems.